uOttawa
University of Ottawa
Faculty of Engineering
Department of Chemical and Biological Engineering

Transport Phenomena in Oscillatory Flow Mini Coils for Solid-forming Reactions

A dissertation submitted by

Mohammad Mahdi Fadaee

to the University of Ottawa

in partial fulfillment of the requirements for the degree of

Doctor of Philosophy in Chemical Engineering

Abstract

Traditional pharmaceutical and fine chemical production processes possess a high degree of flexibility because batch or semi-batch stirred tank reactors are primarily utilized, which aren't often allocated to any specific reaction or product; instead, they are flexible to produce different chemicals via various reactions at a wide range of operating conditions. This flexibility is associated with some problems, such as low heat transfer performance, poor mixing quality, and fouling. Reducing the problems associated with traditional pharmaceutical processes is included in the concept of "Process Intensification," which refers to methods and modifications implemented in a process to enhance its efficiency and economy, such as reducing equipment volume, handling chemical reactions at optimized conditions, decreasing energy consumption, and waste materials.

The focus of this research was on the intensification and characterization of a coil reactor capable of handling solid-forming reactions and potentially applicable to pharmaceutical industries. This type of reactor has been partially intensified as its flow is continuous, and its volume reduced relative to batch-wise operation. In this work, oscillatory flow at different operating conditions (frequency, amplitude, and net flow rate) was applied to the fluid flowing in the reactor, aiming to better intensify its performance.

First, the behavior of fluid flow inside the reactor in terms of residence time distribution (RTD) and associated axial dispersion was experimentally investigated and mathematically characterized by a statistical model. The results showed that there is a point at which the axial dispersion under oscillatory conditions is minimum. The axial dispersion was also correlated with the operating conditions and coil dimensions by a Dean number with the flow amplitude as the characteristic length.

Second, the viscous power dissipation and phase shift between the coil pressure drop and velocity at different oscillatory conditions was numerically studied by a CFD model in order to better understand the relationship between the instantaneous flow field, power dissipation and the RTD variance.

Third, the enhancement of the wall-to-fluid heat transfer was evaluated under non-

oscillatory and oscillatory conditions. For the non-oscillatory experiments, three new correlations were developed for the thermal entrance length of coils, Nusselt number of developing laminar flow, and combined (developing and developed) flow, and the Nusselt number of turbulent flow. The result showed that the heat transfer coefficient of coils in laminar flow is not significantly dependent on the coil curvature. Then the Nusselt number of the oscillatory flow was characterized using the non-oscillatory results and correlated with the operating conditions and coil dimensions. The results showed that although oscillation can enhance the coil heat transfer coefficient, the amount of enhancement is limited by the net flow rate.

Finally, the reactor performance during a sample solid-forming reaction was characterized, and the effect of oscillatory conditions on the particle size distribution was studied. The net flow rate and oscillation frequency can effectively change the particle size, while the effect of amplitude needs more investigation for different reactions. In addition, online measurement of the pressure drop for a concentrated reaction showed that oscillation can extend the operation time by decreasing the amount of fouling and consequently the risk of blocking.

According to the achievements in this research, applying oscillation can provide ranges of operating conditions in which the plug flow performance, convective heat transfer coefficient, particle growth, and PSD broadness are optimized. However, these ranges are mostly independent, and for quantities related to solid forming reactions, they are case-specific. Therefore, to design a reactor for a specific solid-forming reaction, a trade-off must be established between different design parameters such that more important quantities are in acceptable ranges.

Sommaire

Les procédés traditionnels de production pharmaceutique et de chimie fine offrent une grande flexibilité grâce à l'utilisation prédominante de réacteurs à cuve agitée, discontinus ou semi-discontinus. Ces réacteurs ne sont généralement pas consacrés à une réaction ou un produit spécifique; ils permettent de produire différents produits chimiques par diverses réactions dans des conditions opératoires très variées. Cette flexibilité est associée à certains problèmes, tels qu'un taux transfert de chaleur relativement faible, une mauvaise qualité de mélange et l'encrassement. La réduction des problèmes liés aux procédés pharmaceutiques traditionnels relève du concept d'«intensification des procédés», qui désigne les méthodes et modifications mises en œuvre pour améliorer l'efficacité et la rentabilité d'un procédé, telles que la réduction du volume des équipements, la gestion des réactions chimiques dans des conditions optimisées, la diminution de la consommation énergétique et des déchets générés

Cette recherche portait sur l'intensification et la caractérisation d'un réacteur à serpentin capable de gérer des réactions de formation de solides et potentiellement applicable à l'industrie pharmaceutique. Ce type de réacteur a été partiellement intensifié grâce à son écoulement continu et à son volume réduit par rapport à un réacteur à cuve agitée. Dans ce travail, un écoulement oscillatoire sous différentes conditions de fonctionnement (fréquence, amplitude et débit net) a été appliqué au fluide s'écoulant dans le réacteur afin d'en améliorer les performances.

Tout d'abord, le comportement de l'écoulement du fluide à l'intérieur du réacteur en termes de distribution des temps de séjour (RTD) et de dispersion axiale résultant a été étudié expérimentalement et caractérisé mathématiquement par un modèle statistique. Les résultats ont montré qu'il existe un point où la dispersion axiale en conditions oscillatoires est minimale. La dispersion axiale a également été corrélée aux conditions d'opération et aux dimensions du serpentine par un nombre de Dean dont l'amplitude de l'écoulement étant la longueur caractéristique.

Deuxièmement, la dissipation de puissance visqueuse et le déphasage entre la chute de pression de du serpentin et la vitesse dans différentes conditions oscillatoires ont été étudiés numériquement par un modèle CFD afin de mieux comprendre la relation entre le champ

d'écoulement instantané, la dissipation de puissance et la variance de la RTD.

Troisièmement, l'amélioration du transfert de chaleur paroi-fluide a été évaluée en conditions oscillatoires et non oscillatoires. Pour les expériences non oscillatoires, trois nouvelles corrélations ont été établies pour la longueur d'entrée thermique des serpentins, le nombre de Nusselt de l'écoulement laminaire en développement, l'écoulement combiné (en développement et développé) et le nombre de Nusselt de l'écoulement turbulent. Les résultats ont montré que le coefficient de transfert thermique des serpentins en écoulement laminaire ne dépend pas significativement de la courbure de ces derniers. Le nombre de Nusselt de l'écoulement oscillatoire a ensuite été caractérisé à l'aide des résultats non oscillatoires et corrélé aux conditions d'opérations et aux dimensions des serpentins. Les résultats ont montré que, bien que l'oscillation puisse améliorer le coefficient de transfert thermique des serpentins, cette amélioration est limitée par le débit net.

Enfin, les performances du réacteur lors d'une réaction de formation de solides ont été caractérisées et l'effet des conditions oscillatoires sur la distribution des particules solides a été étudié. Le débit net et la fréquence d'oscillation peuvent effectivement modifier la taille des particules, tandis que l'effet de l'amplitude nécessite des recherches plus approfondies pour différentes réactions. De plus, la mesure en ligne de la perte de pression pour une réaction concentrée a montré que l'oscillation peut prolonger la durée de fonctionnement en réduisant l'encrassement et, par conséquent, le risque de blocage.

D'après les résultats de cette recherche, l'application d'oscillations permet d'obtenir des plages de conditions opératoires optimisant les performances d'écoulement piston, le coefficient de transfert thermique par convection, la croissance des particules et la largeur de la distribution granulométrique. Cependant, ces plages sont généralement indépendantes et, pour les grandeurs liées aux réactions de formation de solides, elles dépendent du cas étudié. Par conséquent, pour concevoir un réacteur adapté à une réaction de formation de solides spécifique, il est nécessaire d'établir un compromis entre différents paramètres de conception afin que les grandeurs les plus importantes se situent dans des plages acceptables.

Statement of Contributions

I hereby declare that I am the sole author of this dissertation. I have conducted experiments for Chapters 3, 4 and 5, analyzed data and prepared the resulting manuscripts for publication. I also wrote VBA codes to model residence time distribution and heat transfer data. My supervisors, Professors Arturo Macchi, Jan Haelssig, and Dominique Roberge, supervised the experimental plans for power dissipation, heat transfer, and solid forming studies, and provided guidance and editorial comments throughout this research. The experimental data used in Chapter 2 was produced by Dr. Brendon Doyle at Lonza under Prof. Dominique Roberge's supervision. I also cowrote Chapter 3 with Prof. Haelssig as he performed CFD simulations for this research.

Acknowledgements

I would first and foremost like to express my deep gratitude to my supervisors Prof. Arturo Macchi for providing me with the opportunity to perform this research. His continued support and mentorship throughout have been invaluable to my scientific development, and I owe much of my academic success to his supports.

I deeply feel beholden to my co-supervisor, Prof. Jan Haelssig, for his distinguished technical and scientific advice throughout the research, and for the results of CFD simulations.

I would like to thank Prof. Dominique Roberge for his guidance and resources.

I would like to acknowledge the financial supports of the Natural Sciences and Engineering Research Council of Canada, Eurofins Alphora, and University of Ottawa.

Finally, I would like to thank the technical staff of the Department of Chemical and Biological Engineering, Franco Zilardo, Patrick Pageau, and Gerard Nina, for their assistance with the design, construction, and instrumentation of a multi-purpose reactor. During this research, I learned many technical things from them, and the progress in this research would not be possible without their assistance.

To

thousands of martyrs of Iran's freedom protests who were massacred in January 2026,
by the illegitimate genocidal regime of the mullahs,
who occupied Iran in 1979.

Table of Contents

List of Figures

List of Tables

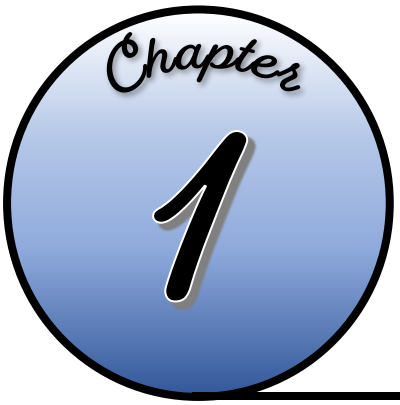

Introduction

1.1. Introducing Research Topic

Traditional pharmaceutical and fine chemical production processes possess a high degree of flexibility due to their short duration and proper response to continuously changing market demands. The scale of these processes is significantly smaller than the one of bulk chemicals industries and is usually on the order of a few kilograms to 100 tonnes per year. [1] Therefore, these chemicals are often produced in modular and/or multipurpose plants that utilize primarily batch or semi-batch stirred tank reactors. These reactors are often not optimized to any specific reaction or product, instead, they are designed to accommodate a wide range of reactions and operating conditions. This flexibility makes it feasible to produce different chemicals through a schedule of campaigns that can last as little as a few days or as long as a few months, allowing for production of a large number of different products annually in a single train. [2,3] On the other hand, this flexibility is associated with some costs. Most processes in this industry are developed at lab-scale and then scaled up by increasing the vessel size while maintaining a similar geometry. The increase from a lab-scale flask to a production-scale reactor decreases the reactor surface area to volume ratio, negatively impacting the heat transfer performance of the system. Furthermore, a smaller heat transfer surface area increases the rate of fouling on the internal surfaces of the reactor, causing an excessive decline in the heat transfer performance during the reaction, especially high-fouling ones. The mixing quality also decreases when a lab-scale batch reactor is scaled up to an industrial scale, leading to a decrease in the mass transfer performance of the reactor. In some reaction media, a poor mixing quality leads to instability and finally the precipitation of produced solid particles, increasing the rate of fouling. As a result, batch vessels are usually operated at more dilute and less extreme conditions to minimize negative effects of increased fouling tendency and reduced mixing quality, leading to reduced performance as their scale increases. Overall, batch/semi-batch production-scale pharmaceutical processes operate at sub-optimal efficiency with reduced space-time yields. [4–7]

Reducing the problems associated with traditional pharmaceutical processes is included in the concept of “Process Intensification” which refers to a wide range of methods and modifications implemented in an establishing or existing process in order to enhance its efficiency and economy. [8] These types of modifications comprise the reduction in equipment volume, [9] handling chemical reactions at optimized conditions, decreasing

energy consumption and waste materials, consequently leading to a lower-cost, more sustainable process. [10] The decrease in equipment volume consisting of lumping several unit operations, compacting, or installing them in a smaller space can decrease the material holdup as well as improve heat and mass transfer within them. [11,12] The concept of process intensification is complementary to the Industry 4.0 standard for a high degree of automation and information processing in chemicals production. [13] In this idea, processing equipment is able to communicate with each other and their operators digitally, leading to a high level of information transparency and availability as well as the ability of machines and artificial intelligence to help with decision making and performing of difficult tasks.

In this research, the focus will be on the characterization and optimization of a reactor capable of handling solid-forming reactions which has been previously intensified by several methods and is potentially applicable to pharmaceutical industries. This reactor is a coil reactor in which an oscillatory flow is applied. According to the concept of process intensification, the following are the most important intensification cases which have been implemented for this type of reactor:

- Continuous flow within the reactor
- Decreased volume and holdup due to higher volumetric efficiency
- Enhanced heat transfer
- Improved mixing
- Reduced fouling/clogging

In this work, an oscillatory flow will be applied to the fluid flowing in the reactor aiming to better intensify its performance. For this purpose, the performance of the reactor at different net flow rates and different oscillatory conditions (amplitude and frequency of oscillation) will be studied for different reactor dimensions (tube diameter and coil diameter) and the optimum operating conditions for a given transport parameter will be determined. First, the behavior of fluid flow inside the reactor in terms of axial dispersion will be characterized. Then, the viscous power dissipation and phase shift, as two key parameters in micromixing characterization will be investigated. The enhancement of the wall-to-fluid heat transfer under oscillatory conditions will be also evaluated. In the last part, the reactor performance

during a solid-forming reaction will be characterized and the effect of oscillatory conditions on the product size distribution as well as the extent of fouling and clogging will be studied. For each section, the optimum combination of reactor geometry and operating conditions will be determined with consideration toward better intensification.

1.2. Literature Review

Despite many process intensification attributes addressed in the literature, there are some barriers to intensifying processes such as high cost and complexity. [8] Furthermore, the nature of many existing processes is not compatible with modifications like decreasing equipment volume/holdup, compacting/lumping unit operations, improving heat and mass transfer, etc. Therefore, there is a tendency to implement intensified technologies in cases where a plant is being designed or developed. [8]

One of the industries in which the process intensification concept has been highlighted is the pharmaceutical industry. There are many processes in this industry within which one or more reactions are handled batchwise even though they are essentially short-lived. Hence, there is a tendency to decrease equipment volume and make these processes continuous to benefit from the advantages of the process intensification mentioned before. By doing these modifications, product quality and control, as well as productivity, are expected to be improved and hazardous materials are handled more safely. [14–17]

To decrease the size of plants, plate microreactors have been studied for multiphase fluids containing liquid and gas phases, especially where more plug flow along with rapid micromixing is required. [18] Coil reactors have also been employed for slower reactions where a longer residence time is needed. [19,20] The importance of employing these types of reactors is highlighted when there is a need for producing a single product (or a limited number of products requiring similar operating conditions) to respond to market demands, particularly in terms of the fluctuation in production volume. [19] In this condition, employing a monoplant with a modular structure instead of a multipurpose plant is desired. In addition to reduced volume in this intensified structure, it can be designed for a continuous operating mode to eliminate the lead-time generally associated with batch processes and increase its productivity. However, a high degree of automation is needed along with this

intensification [13] as well as a shift to reaction technologies that are suitable for continuous processing. [18]

Pharmaceutical production processes often involve solid materials as reactant, catalyst, or final product. These processes are traditionally handled batchwise; however, in redesigning or modifying them for the purpose of intensification, some proper consideration should be adopted to deal with the problems resulting from solid materials. When the size of equipment is reduced, the resized unit has a high potential for fouling and clogging. This issue may worsen when the unit is to be utilized at higher temperatures and/or pressures. To minimize problems resulting from the presence of solid materials, the degree of mixing is augmented using some methods although selecting an appropriate structure for the reactor such as a baffleless coil may be also included. There are two general methods of augmenting the degree of mixing: passive and active. [21] The former acts based on the passage of the fluid through a channel whose fluid velocity direction and/or magnitude change repeatedly such as for a plain or inverted coil or a tube having helical, integral, central, or orifice baffles. The source of mixing energy in passive mixing is the kinetic energy of the fluid, while active mixing essentially uses an external source of energy [21] that is separate from the fluid kinetic energy, enhancing transport properties for a wide range of residence time. [21] This is very helpful when switching from a batch process with a long residence time to a continuous one in which the use of only a passive mixing method requires relatively high flow rates. [22]
An active mixing method for continuous intensified reactors is applying oscillation on the flowing fluid independent of the net flow rate by alternately drawing and discharging the fluid at a certain frequency and amplitude. [23,24]. Often, an active mixing method is combined with a passive one such as channel curvature or baffles/plates inside the flow channel. [20,25]

A baffleless oscillatory coiled channel, using curvature to promote passive mixing, is a promising choice for intensifying pharmaceutical reactions involving solid materials because both active and passive methods of mixing are employed while limiting the potential of fouling and finally blocking. In the following sections, the differences between the flow patterns in straight and curved pipes will be reviewed. Then, it will be demonstrated how different flow patterns in a curved pipe can affect mixing conditions, heat transfer, and solid

forming reactions in the absence and presence of oscillation. The concept of mixing at different scales will be also reviewed and an introduction to the characterization of mixing will also be provided.

1.2.1. Flow in Straight and Curved Pipes

When a fluid flow with a uniform velocity profile enters a straight tube or pipe, depending on the Reynolds number ($Re_n = \rho u d_{t,i}/\mu$) the flow regime is determined. The limits of Re_n are well-known so that for Re_n < 2300, the flow regime is considered laminar, for 2300 < Re_n< 4000, the flow regime is transitional and for Re_n > 4000 the flow regime will be turbulent. [26] In addition to the limits of the flow regime, the length of a pipe with specific dimensions over which the flow becomes fully developed (length of hydrodynamic entrance region) can be calculated using the boundary layer thickness relationships which are different for each flow regime. The criterion for a flow to be developed is that the boundary layer thickness must approach the pipe radius (**Figure 1-1**).

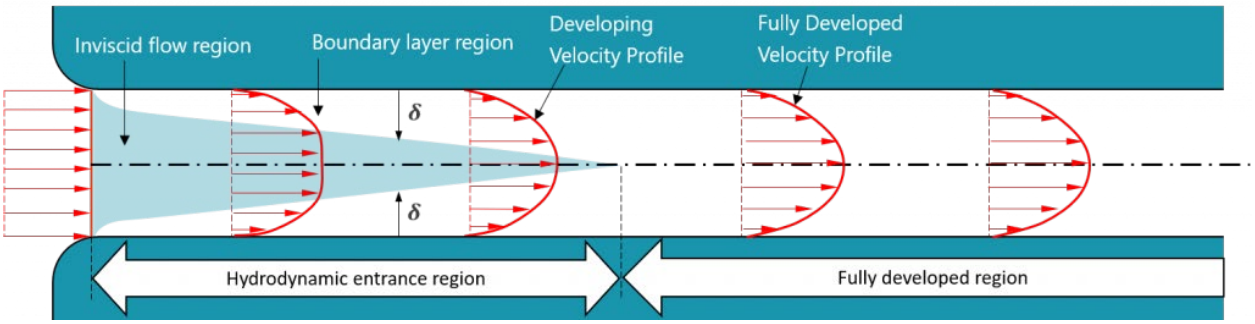

Figure 1-1. Developing velocity profile of a fluid entering a pipe.

In a laminar flow (Re_n <2300) the fluid layers slide past each other so that they do not cross the adjacent layers, and any transport phenomena between two adjacent layers occur via the diffusion mechanism. The layers close to the pipe wall have a slower motion so that the radial profile of the axial velocity has a parabolic shape in the developed region. When 2100 < Re_n < 4000, the fluid layers have a wavy motion so that there is some bulk flow between layers. This is the introduction of forming fluid eddies. When Re_n > 4000, the fluid flow is completely turbulent and eddies which are small pieces of the fluid with chaotic motion predominate the flow and possess the most important role in all transport phenomena in the pipe. The axial velocity profile for turbulent flow is not uniform but a main part except near the pipe wall of

it can be considered approximately uniform because the rate at which momentum is transported radially by the eddies is very high.

If a fluid flow with any regime passes through a curved pipe with sufficient curvature, the curved path causes the direction of the fluid elements to change, leading to radial pressure and velocity gradients after a short distance from the curved pipe entrance. [27] Near the convex (inner) wall, the axial velocity decreases and the pressure increases, while the opposite occurs near the concave (outer) wall for both quantities (**Figure 1-2**). The centrifugal force created by the curved pipe which is proportional to u^2/R_c (u: velocity, R_c: radius of curvature) is combined with the fluid flow and creates a new flow pattern called the secondary flow. When the central part of the flow which has a higher velocity is driven toward the concave wall due to the centrifugal force, the fluid near that wall returns instead to the center of the pipe. If the velocity of the fluid is high enough and/or the radius of curvature of the pipe is low enough, the centrifugal force produces a pair of symmetrical counter-rotating vortices at the center of the pipe known as the Dean vortices which are symmetrical relative to the central horizontal plane of the pipe.

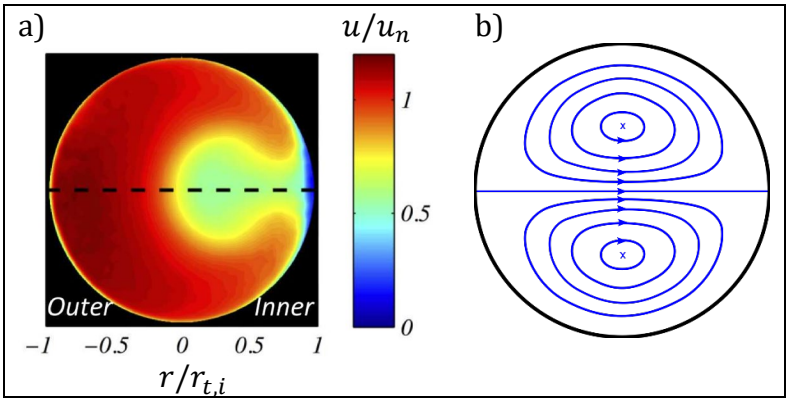

Figure 1-2. a. An example of the velocity gradient at the exit of a 90° bend, [27] b. Schematic representation of the Dean vortices.

The characterization of the Dean vortices consisting of the conditions of creation, the flow regime, and transition between two consecutive regimes is based on an important dimensionless group named the Dean number:

$$De = \frac{\rho u_n d_{t,i}}{\mu}\sqrt{\frac{d_{t,i}}{2R_c}} = Re_n\sqrt{\frac{d_{t,i}}{2R_c}} \qquad (1\text{-}1)$$

This group appears in solving the Navier-Stokes equation for a Newtonian fluid passing through a curved pipe. The physical meaning of this number is similar to the Reynolds number with the difference that the centrifugal force is also included in this number as follows:

$$De = \frac{\sqrt{\frac{1}{2}(inertial\ forces)(centrifugal\ forces)}}{viscous\ forces} = \frac{\sqrt{\frac{1}{2}(\rho d_{t,i}^2 R_c u_n^2/d_{t,i})(\rho d_{t,i}^2 R_c u_n^2/R_c)}}{\mu(u_n/d_{t,i})d_{t,i}R_c} = \frac{\rho u_n d_{t,i}}{\mu}\sqrt{\frac{d_{t,i}}{2R_c}}$$

Many studies have been performed since the 1920s on the secondary flow in curved pipes and its relationships with the Dean number. Despite reporting some limits for the Dean number to specify the flow regime, they are not in good agreement with each other. Nonetheless, some limits can be considered to initially assign a flow regime to a value of the Dean number. If the flow regime before entering a rectangular curved channel is a fully-developed laminar flow, the flow pattern remains unidirectional and laminar at $De < 40$ when passing through the curved channel. This limit can be a higher value up to $De = 60$. [28] Overall, between the Dean numbers of 40 and 60 (sometimes up to 75), the flow becomes gradually unstable indicating that a pair of vortices are being formed. [28,29] At higher Dean numbers, the vortices develop and begin to undulate. When the Dean number ranges from 90 to 100, the vortices approximately cover the entire cross-section of the channel. [28] From the start of forming the secondary flow up to $De = 130$, the Dean vortices undulate (wavy regime). The splitting and merging of the Dean vortices are also observed over the same range of the Dean number. When $130 < De < 200$, the undulating wavy regime is replaced by a twisting regime. Above $De = 160$, twisting becomes more important because this leads to an increase in longitudinal fluctuation. [28] Initial signs of the flow turbulence are observed for $De > 100$, but fully turbulent flow occurs at $De > 400$. [28]

As can be clearly seen, specifying exact values of De is not quite feasible for any transition between different regimes. The most important reason for these uncertainties is that the transition between two consecutive regimes depends on both De and the curvature ratio ($d_{t,i}/(2R_c)$) even though the latter has been included in De. This can be inferred from some correlations proposed to calculate the critical Reynolds number in curved pipes. [30] This is why the transition from the laminar to the turbulent flow does not have a universal solution. [27]

The formation and development of the Dean vortices are also dependent on some other parameters in addition to De and curvature ratio. One of them is the bend angle (coordinate θ in **Figure 1-3-a** and **Figure 1-3-b**). Some studies show that the Dean vortices at bend angles less than 30° are not formed or clearly visible and above that up to a bend angle of 75°, the initial flow regime becomes highly distorted. [27] Another study also shows that at a 30° bend angle, the secondary flow intensity is greatest and decreases slightly afterward. [31] It seems that the bend angle at which the Dean vortices are visible is dependent on both De and curvature ratio similar to the flow regime transition limits of De. However, it can be concluded that at every condition, there is a minimum value of the bend angle less than which the secondary flow is not expected.

The secondary flow formed at a minimum bend angle grows if the curved path continues until the vortices cover the majority of the pipe cross-section. In this condition which the secondary flow is called "developed", only a thin viscous layer near the pipe wall exists named the secondary boundary layer. The thickness of this layer is limited to a short distance from the surface of the pipe wall. As long as the vortices are present at the center of the pipe, this layer cannot grow considerably. Therefore, its thickness is different from the one of straight pipes. The length of a curved pipe that a flow requires to reach a fully developed state is shorted than the one of a straight pipe with a similar diameter at a similar Reynolds number. [32]

To numerically study the behavior of the secondary flow and the secondary boundary layer, two distinct coordinate systems are selected (**Figure 1-3**). For the fluid motion outside the secondary boundary layer, a cylindrical polar coordinate system consisting of R', θ, and Z' is used (**Figure 1-3-a**) For the secondary boundary layer, a toroidal coordinate system consisting of r', α, and θ is instead employed (**Figure 1-3-b**). The velocity vector in the secondary boundary layer has two components. One of them is parallel to a line tangent to axis θ, and the other one is parallel to a line tangent to axis α (**Figure 1-3-c**). Several numerical studies performed on the behavior of the secondary boundary layer in laminar and turbulent flows show that its thickness changes in both θ and α directions such that a separation point is predicted for α = 60°–90° for a laminar flow [32] and for α = 60°–110° for a turbulent one. [33] Moreover, the thickness of the secondary boundary layer gradually

increases as the fluid travels further downstream. [32] As long as the flow path is curved, the secondary flow persists, unless the pipe becomes straight. In this condition, the vortices start to break down at some downstream distance from the bend exit, however, they may persist up to a distance of ten pipe diameters. [27]

Another parameter that affects the formation of the secondary flow is the velocity profile at the inlet of a bend. Four types of velocity profiles have been considered in the literature for a fluid entering a bend: uniform, laminar, turbulent, and turbulent swirling. Depending on the inlet velocity profile, the required length of a bend through which a flow becomes fully developed is different. The other parameters which are affected by the inlet velocity profile are the shape of the vortices, the location of the boundary layer separation, and the velocity profiles of the secondary boundary layer and vortices.

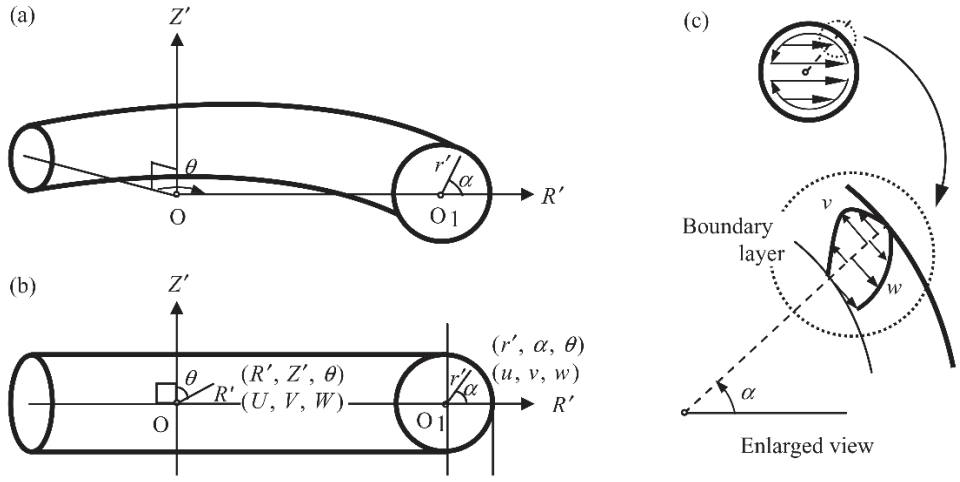

Figure 1-3. The two coordinate systems used to study the secondary flow and secondary boundary layer: a. The cylindrical polar coordinate system consisting of R', θ, and Z' to study the secondary flow, b. The toroidal coordinate system consisting of r', α, and θ to study the secondary boundary layer, c. The velocity profile and its components in the secondary boundary Layer. [33]

For an inlet flow that is turbulent, the complexity of the secondary flow increases so that some other pairs of vortices with very complicated configurations may be formed, although the majority of the pipe cross-section is occupied by a pair of large vortices. [34] For very low values of R_c (sharp bends), instead of the two large vortices, only a single vortex with a very complicated velocity profile may be formed. The rotating direction of a part of this vortex is clockwise in contrast to the other part. [35] Accordingly, a separation plane is observed

between these two parts as indicated in **Figure 1-4**. [36,37] This phenomenon is called swirl switching in which the axial velocity profile of the clockwise rotating part is different from that of the other part, meaning that there is a negative-velocity part in this single vortex.

Turbulent swirling flows generally exist at the outlet streams of rotary equipment such as turbines. When this type of flow enters a bend, the swirling flow is combined with the effect of the bend on the flow and alters the velocity profile in the bend. Limited studies have been performed in this regard which show that at high values of swirling speed, the Dean vortices and other possible pairs of vortices gradually merge and form a single vortex whose axis of rotation is near the pipe centerline (**Figure 1-5**).

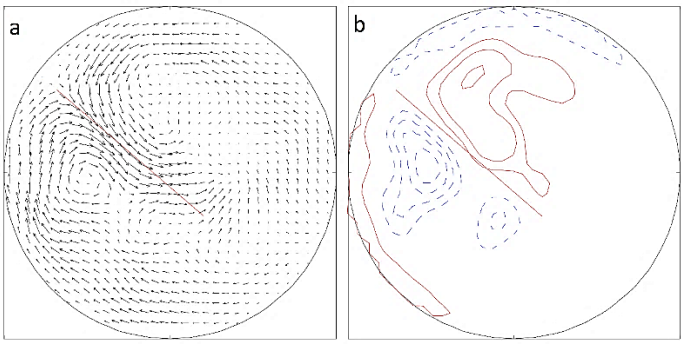

Figure 1-4. The swirl switching of the vortices: a. Velocity vector field, b. Contours of streamwise vorticity (blue dashed lines indicate negative values and red solid lines indicate positive value). [37]

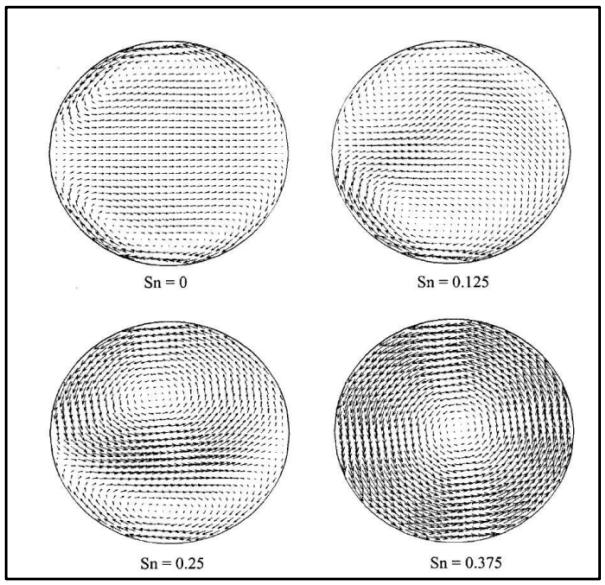

Figure 1-5. Flow structures at increasing swirl intensities ($S_n = \Omega d_{t,i}/(2u_n)$) where Ω is the angular speed of the flow). [38]

When a tubular reactor is constructed in the form of a coil, the formation of the secondary flow is considered as a passive mixing method because the kinetic energy of the fluid is

consumed to create the Dean vortices. Recent studies on coil reactors demonstrate that the formation of the secondary flow can improve the radial mixing, causing better plug flow performance (See Section 1.2.3.1). [39,40] Despite this improvement, any transport phenomena at the center of the Dean vortices occur via diffusion. [41] To improve the mixing quality at the central part of the vortices, modified structures of coils that disrupt the vortices are employed. One way to periodically disrupt the vortices and promote mixing across streamlines is known as an inverter which is a bend in the middle of a straight coil which alters the way a coil continues its turns such that there is a large angle between the axis of the coil upstream the inverter and the one downstream it. **Figure 1-6** shows a 90° flow inverter in the middle of a coil. Each inverter changes the direction of the centrifugal forces, causing the Dean vortices to rotate as well as their central parts as indicated in **Figure 1-6**. Periodically rotating the location of the Dean vortices by creating several inverters in the path of a coil (now called coiled flow inverter or CFI) improves radial mixing as well as plug flow performance and diminishes the impact of the stagnant points at the centers of the Dean vortices. A new generation of CFIs with a large number of inverters [42] named compact coiled flow inverter (CCFI) has a plug flow performance comparable to active mixing methods; however, a minimum number of turns between two consecutive inverters is required to allow the secondary flow to be fully developed after inversion. [43] This minimum limits the number of inverters for a certain length of a coil.

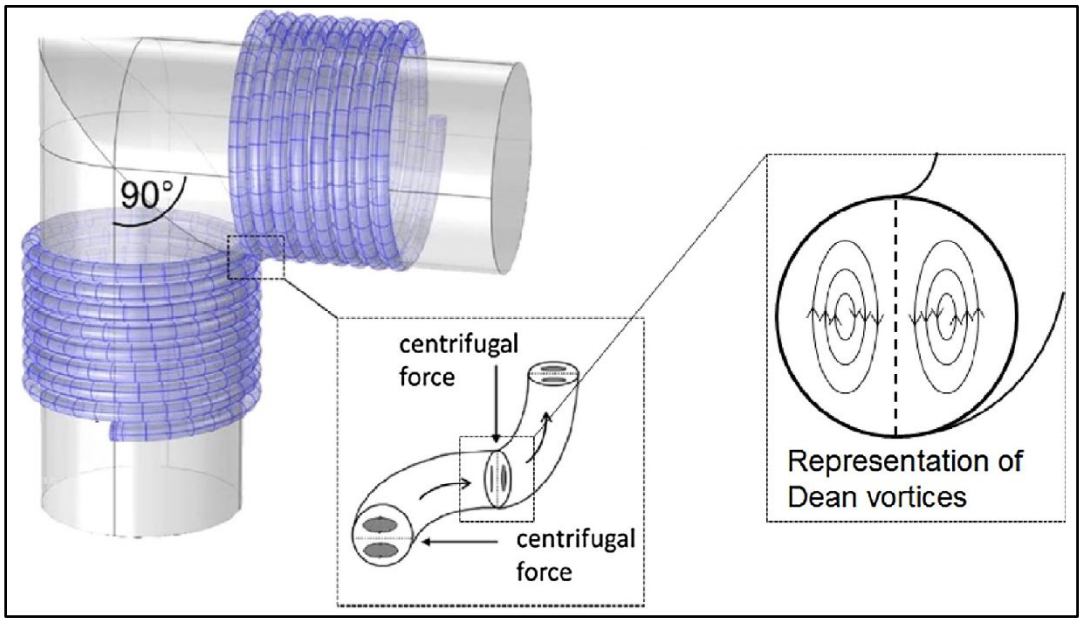

Figure 1-6. Coiled Flow Inverter (CFI) with a single 90° inversion. [44]

1.2.2. Oscillatory Flow

One of the active mixing methods in continuous reactors is the use of oscillation. An oscillatory flow can be created using two general methods: installing vibrating/oscillating parts in contact with the fluid like vibrating baffles, and the use of a device that draws the fluid backward and push it forward through a reactor such as a pulsator pump which has a structure similar to reciprocating pumps with only one port for the suction and discharge and without any check valve at the port. The use of pulsators is more favored especially for solid-forming reactions because there is no need to install moving parts in the fluid path.

In pulsator pumps, a certain rotational motion is converted to a linear reciprocating motion (**Figure 1-7**). If this motion is transmitted to a stagnant fluid in a pipe via a piston/diaphragm, the mean fluid velocity has a sinusoidal profile versus time and is calculated by using the following expression:

$$u_o = 2\pi f x_o \, sin(\Omega_o t) \tag{1-2}$$

where f is the frequency of oscillation, x_o is the amplitude of oscillation, Ω_o is the angular speed of the pulsator driver and t is time. x_o is the distance passed by the fluid within a quarter of a cycle regardless of its direction. The maximum fluid velocity occurs at the phase angles π/2 (forward direction) and 3π/4 (backward direction):

$$u_{o,max} = 2\pi f x_o \tag{1-3}$$

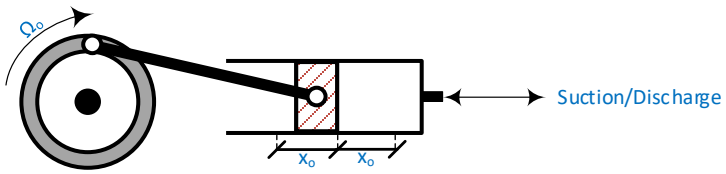

Figure 1-7. The conversion of rotational motion to reciprocating motion in a typical pulsator.

If this type of oscillation is applied on a continuous tubular reactor, depending on the net flow rate of the reaction medium (u_n), 5 modes may take place: [45]

a. **Steady Unidirectional Flow:** This type of flow which occurs in the absence of oscillation (Ω_o = 0) has only a net positive velocity of u_n (**Figure 1-8-a**)

b. **Pulsing Unidirectional Flow (Pulsatile):** It has a net flow velocity larger than the maximum oscillatory flow velocity ($u_n > u_{o,max}$), meaning that the flow always moves forward with a cycle of acceleration and deceleration (**Figure 1-8-b**).

c. **Start and Stop Flow:** When $u_n = u_{o,max}$, at the phase angle of $3\pi/4$, the flow stops and then continues (**Figure 1-8-c**).

d. **Asymmetrical Oscillatory Flow (Reverse Pulsatile):** This case occurs if $0 < u_n < u_{o,max}$ so that in a part of every oscillation cycle, the velocity becomes negative (**Figure 1-8-d**)

e. **Symmetrical Oscillatory Flow:** This type of flow takes place when there is no net flow ($u_n = 0$), therefore, only the fluid moves forward and backward at certain oscillatory conditions. Because this type of flow does not lead to a continuous throughput, it is kind of an oscillatory batch process (**Figure 1-8-e**)

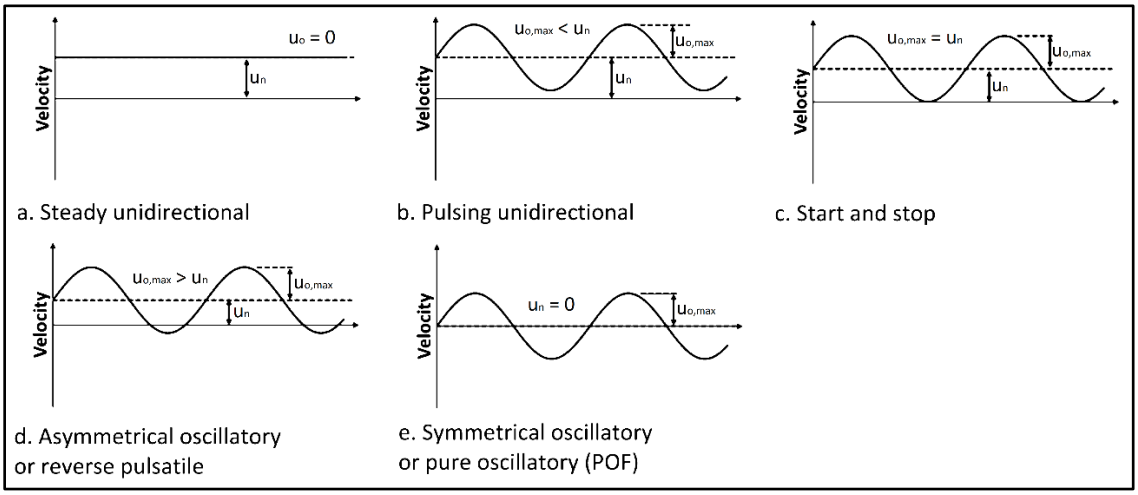

Figure 1-8. Types of oscillatory flow. [45]

Several structures of continuous reactors have been studied to evaluate their plug flow performance under oscillatory conditions such as baffled reactors and coil reactors. The overall consequence of applying oscillation is that the plug flow performance is improved provided that the velocity ratio $u_{o,max}/u_n$ ranges from 2 to 10 (pulsatile flow). [46] The mechanism of improving plug flow performance is different for every reactor. For instance, if oscillation is applied on a baffled reactor, at optimized oscillatory conditions, each interbaffle zone approaches a perfectly mixed reactor [23,46] due to the formation of longitudinal vortices inside it in both forward and backward directions (**Figure 1-9**). If the

number of interbaffle zones is high enough, the overall behavior of the reactor approaches a plug-flow reactor based on the tanks-in-series model. [47] Other structures with periodic constraints such as multi-orifice or integral baffles act similarly, but, the mechanism for the coil reactors is somewhat different.

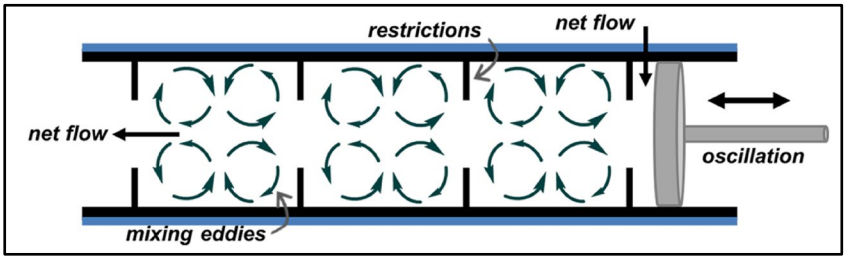

Figure 1-9. Generation of longitudinal vortices in interbaffle zones of a reactor with periodic constraints. [46]

As stated previously, if a coil reactor with only a steady unidirectional flow is employed, the formation of the secondary flow is considered a passive mixing method because the kinetic energy of the flow supplies the energy required for the formation of the vortices. If oscillation is applied to the flow, the secondary flow due to the reciprocating motion of the fluid intensifies, impacting considerably the radial mixing. The intensification of the secondary flow due to the oscillation is, in fact, an active mixing method. For this type of reactor, a reverse pulsatile flow is generally established so that during a part of an oscillation cycle, the flow velocity becomes negative. Accordingly, it is possible that the Dean vortices are formed in both forward and backward directions which can improve the radial mixing more effectively than when they are formed only in the forward direction with less intensity.

The parameters affecting the flow pattern in an oscillatory flow coil reactor comprise three independent operating variables ($\dot{m}$: net mass flow rate, x_o: oscillation amplitude, f: oscillation frequency) and four coil dimensions (L: length, $d_{t,i}$: inner diameter, R_c: radius of curvature, P_t: tube pitch). Based on the dimensional analyses provided in the literature, an oscillatory flow in a coil is characterized by the dimensionless groups furnished in **Table 1-1**. The physical meaning of the oscillatory Dean number (De_o) is similar to the Dean number (De, Equation (1-1)) with the difference that De_o is defined based on the maximum oscillatory velocity (Equation (1-3)) instead of net flow velocity.

Many numerical and experimental studies have been conducted since the 1970s on the formation of secondary flow at oscillatory conditions. One of the most comprehensive studies

is the one published by Sudo et al. [48] in which an exact classification for flow patterns at different oscillatory conditions has been provided based on both experimental and numerical studies. This classification has been the basis of interpretation in many articles and scientific reports so far. According to this article, 5 types of secondary flow patterns can be observed (Type I to Type V). The formation of these flow patterns is due to the interaction among three forces: inertial force, viscous force, and centrifugal force. The first and second ones are included in the Womersley number (Wo) while all of them are included in De_o (See **Table 1-1**). Therefore, the flow patterns have been classified using different ranges of these two dimensionless numbers as provided in **Table 1-2**:

Table 1-1. Dimensionless groups used to characterize oscillatory flows in curved pipes.

Dimensionless Group	Equation	Physical Meaning
Net flow Reynolds Number	$Re_n = \frac{\rho u_n d_{t,i}}{\mu}$	$Re_n = \frac{inertial\ forces}{viscous\ forces}$
Oscillatory Reynolds Number	$Re_o = \frac{2\pi f x_o \rho d_{t,i}}{\mu}$	$Re_o = \frac{transient\ inertial\ forces}{viscous\ forces}$
Oscillatory Dean Number	$De_o = Re_o \sqrt{\frac{d_{t,i}}{2R_c}}$	$De_o = \frac{\sqrt{\frac{1}{2}(transient\ inertial\ forces)(centrifugal\ forces)}}{viscous\ forces}$
Womersley Number	$Wo = \frac{d_{t,i}}{2}\sqrt{\frac{2\pi f \rho}{\mu}}$	$Wo = \sqrt{\frac{transient\ inertial\ forces}{viscous\ forces}}$
Velocity Ratio	$\Psi = \frac{Re_o}{Re_n}$	

Table 1-2. Ranges of Wo and De_o related to the secondary flow patterns. [48]

Flow Pattern Type	$De_o < 200$	$De_o > 200$
Type I	$Wo < 5.5$	$Wo < 0.64\ De_o^{0.5}$
Type II	$5.5 < Wo < 11$	$0.64\ De_o^{0.5} < Wo < 0.81\ De_o^{0.5}$
Type III	$11 < Wo < 14$	$0.81\ De_o^{0.5} < Wo < 2.38\ De_o^{0.357}$
Type VI	$14 < Wo < 17$	$2.38\ De_o^{0.357} < Wo < 3.11\ De_o^{0.333}$
Type V	$Wo > 17$	$Wo > 3.11\ De_o^{0.333}$

Type I (Dean Circulation): The secondary flow leads to the formation of two symmetrical vortices named the Dean vortices. This flow pattern takes place at low values of Wo and De_o when viscous effects are dominant (**Figure 1-10-a**).

Type II (Deformed Dean Circulation): At higher values of Wo, the viscous effects become restricted to a thin layer near the pipe wall, and the inertia effects increase in the middle of the pipe. In this condition, a stagnant region appears near the outer wall which pushes the Dean vortices toward the upper and lower walls (**Figure 1-10-b**).

Type III (Intermediate Circulation): This flow pattern is indeed the Lyne vortices formation threshold, meaning that further increase in Wo leads to the growth of the stagnant region toward the center of the pipe. In this flow pattern, an additional pair of vortices that rotate in the direction opposite to that of the primary vortices are formed for a short time during a cycle (**Figure 1-10-c**).

Type IV (Deformed Lyne Circulation): The additional pair of vortices which temporarily appear in the intermediate circulation become larger and are permanently observed at higher values of Wo. Nonetheless, their size is still small relative to the primary vortices, and their cores slightly deviate to the outside (**Figure 1-10-d**).

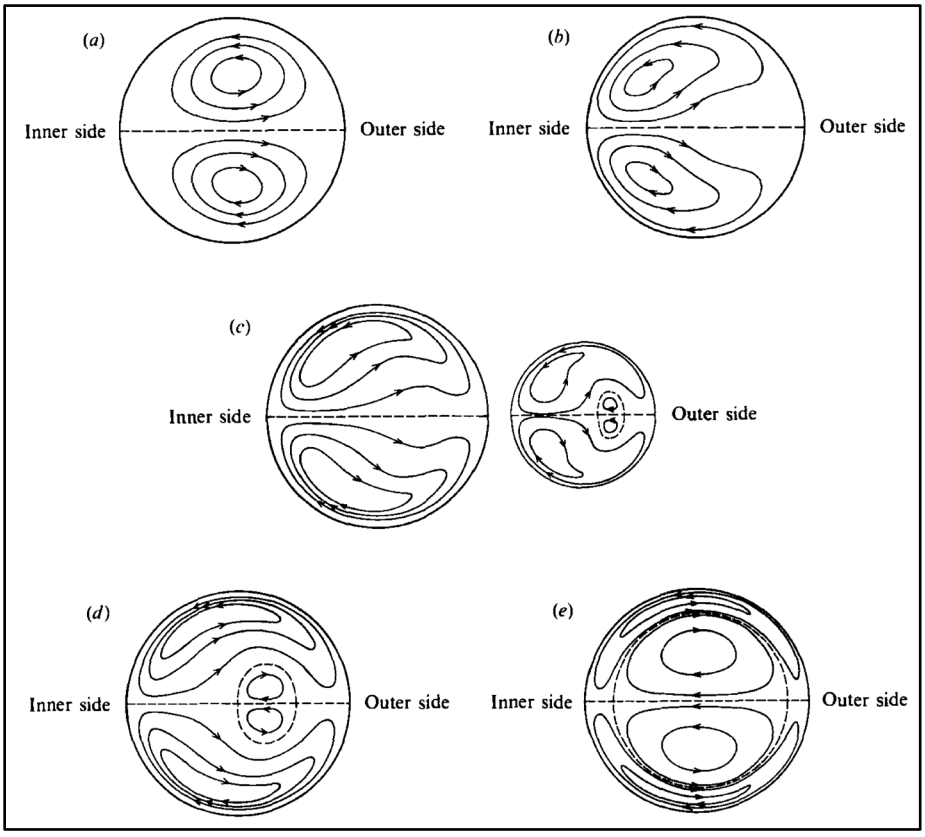

Figure 1-10. Schematic representation of the secondary flow patterns at oscillatory conditions: a. Type I: Dean Circulation. b. Type II: Deformed Dean Circulation. c. Type III: Intermediate Circulation. d. Type IV: Deformed Lyne Circulation. e. Type V: Lyne Circulation. [48]

Type V (Lyne Circulation): The growth of Lyne vortices pushes the primary vortices toward the upper and lower walls such that they only occupy a relatively thin layer near the walls. In this condition, the Lyne vortices occupy the majority of the cross-section of the pipe without any significant deviation to the outside (**Figure 1-10-e**).

Figure 1-11 shows the dependency of the oscillatory secondary flow patterns on the Wo and De_o. The borders between the zones are obtained from the correlations provided in **Table 1-2**. It should be noted that there are some uncertainties about the borders stated in **Table 1-2** but the reported values in the literature are in relatively good agreement. Furthermore, for De_o ranging from 100 to 200 no experimental data was provided in Sudo et al. article. [48] But based on their numerical analysis, for the mentioned range, the correlations provided for De_o < 100 are roughly valid.

Oscillation is applied on the continuous reactors to better improve the quality of mixing and decrease the rate of fouling. For a coil reactor, improving mixing quality means that the flow pattern through the reactor approaches the plug flow pattern more since the secondary flow is formed with higher intensity. As a result, there is less axial mixing of molecules of different ages in the reactor, leading to a narrower particle size distribution in cases where a solid-forming reaction is occurring in the reactor. [20] Furthermore, a plug flow reactor needs less volume because of its higher conversion.

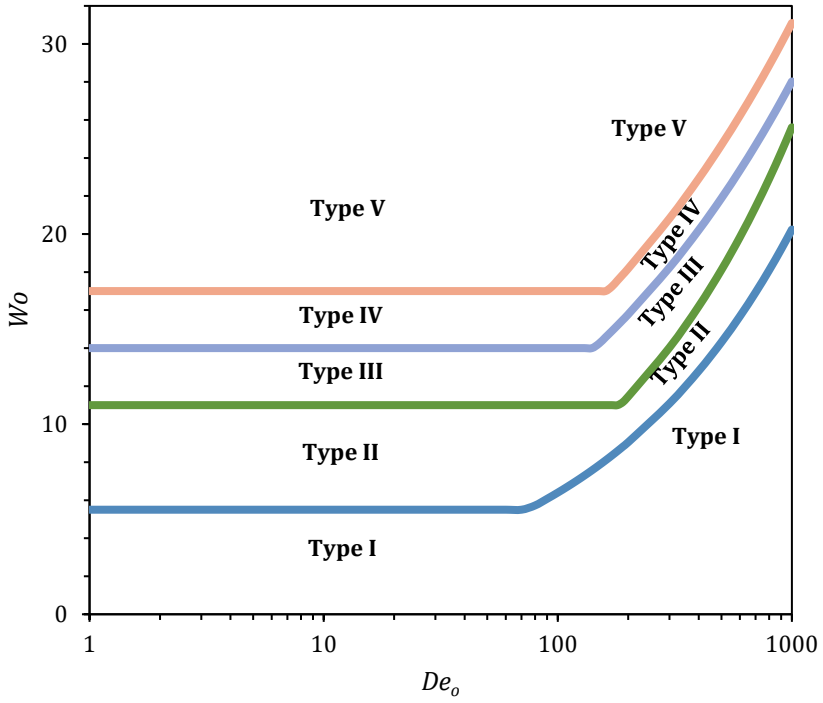

Figure 1-11. Graphical comparison among the ranges of Wo and De_o over which different secondary flow patterns occur. [48]

1.2.3. Mixing

Mixing as a physical phenomenon is an essential problem in process engineering and understanding the mechanism of mixing especially on the microscopic scale is complicated because it is involved in stochastic motion of fluids elements such as eddies. In a chemical reactor, the way reactants are added and mixed with the reaction medium can considerably affect the selectivity and conversion of the reaction. In many chemical processes, complete mixing is required within a short time scale such as a fast reaction in a CSTR reactor. On the other hand, in some other processes mixing must be limited in a specific direction, for instance in the axial direction for a plug flow reactor. For non-reactive operations such as heat/mass transfer, the quality of mixing can impact the transport resistance. In order to evaluate the mixing process of two miscible fluids in an operating unit, some mixing scales are defined as follows:

Macromixing: This term refers to mixing over the entire volume of a vessel or a flow recipient such as a reactor, separator, heat exchanger, column, etc., and describes how fluid elements are distributed over their volume. In this scale, mixing which is done by advecting fluids is dependent on the mean velocity through the vessel. To track the quality of macromixing, macroscopic quantities like temperature or concentration are generally measured.

Micromixing: This term refers to complete mixing on the microscopic scale. This scale is the smallest mixing scale in which complete homogeneity occurs via momentum/molecular diffusion. Mixing in this scale can be independent of macromixing, [49] meaning that the fluid inside a vessel may be macroscopically homogeneous but not microscopically.

Mesomixing: This scale of mixing, which is an intermediate one between micromixing and macromixing, refers to turbulent exchange between a fresh feed entering a vessel and its environment near the entrance/injection point and is governed by turbulent fluctuations. Mesomixing is highlighted in cases where feed pipes are used [50] like an injection nozzle on a large vessel, or a small pipe leading to a larger pipe/header, and describes mixing a fluid entering another fluid in scales comparable to the pipe diameter or the size of large eddies.

1.2.3.1. Macromixing

As stated before, mixing on the scale of the entire recipient depends on the mean flow velocity; therefore, it can be characterized by the residence time distribution (RTD) analysis because an RTD is directly dependent on the overall motion of the fluid and explains how long fluid elements reside in a vessel from its entrance to its exit. To obtain the RTD of a reactor at certain operating conditions, it is conventional that a measurable change is applied on the flow entering a continuous reactor in the form of a step change or pulse-like change in concentration, color, temperature, etc., and the reactor response to the change is measured vs. time at the outlet. Using some statistical equations, the response data are converted to a normalized RTD also named E-curve. For every E-curve which is in terms of dimensionless time (θ), several parameters can be defined, two of which are variance (σ_θ^2) and dimensionless mean residence time (θ_m):

$$\sigma_\theta^2 = \int_0^\infty (\theta - \theta_m)^2 E(\theta) d\theta \quad (1\text{-}4)$$

$$\theta_m = \int_{\theta_{min}}^{\theta_{max}} \theta\, E(\theta)\, d\theta \quad (1\text{-}5)$$

$$\theta = \frac{Q\ t}{V} \quad (1\text{-}6)$$

where Q is the volumetric flow rate, V is the volume of the reactor and t is time. σ_θ^2 ranging from 0 to large numbers (infinity) is a measure of the plug flow performance, meaning that as this parameter decreases at specific operating conditions, the behavior of the reactor under evaluation approaches an ideal plug flow thereby reaching a more uniform axial velocity profile with high intensity of radial mixing and negligible axial mixing. For an ideal plug flow, the obtained E-curve must be the Dirac delta function ($\sigma_\theta^2 = 0$), but it is practically impossible. Based on the axial dispersion model, [47] if an E-curve is almost symmetrical, and $\sigma_\theta^2 < 0.02$, the flow can be considered as an ideal plug flow with very low deviation.

θ_m is a criterion to verify the performance of a reactor in terms of shortcutting and dead zones. Shortcutting makes the average residence time shorter than the nominal one. Sometimes it creates a bimodal RTD with an early happening peak. [51]

Each input change (step change/pulse) has some advantages and disadvantages. The pulse input is more precise in indicating non-ideal conditions associated with reactors, and its E-

curve is directly obtained by continuous measurements at the outlet of the reactor. But the injection equipment must be highly precise so that the amount of the injected material is as accurate as possible and the pulse is as narrow as possible. On the other hand, the step-change method can be less accurate if the outlet measurements are not done with a high sampling rate, and its E-curve is obtained after collecting the data and performing some mathematical operations. Nonetheless, this method is easier.

As the plug flow performance increases (σ_θ^2 decreases), the radial mixing is very high in contrast to the axial mixing. This is very useful for solid forming reactions because under a perfect plug flow, solid particles are formed and grown as the fluid moves forward without any significant axial dispersion. This means that solid particles of different sizes (ages) are not mixed, causing a narrower particle size distribution.

1.2.3.2. Micromixing

When a fluid is mixed, its kinetic energy is converted to heat in microscopic scales; consequently, the internal energy of the fluid is increased. Accordingly, measuring the rate of energy (power) dissipated by the flow can be correlated to mixing on the microscopic scale (micromixing). If the flow is laminar, the power dissipated is related to the viscous effects and mixing between fluid layers via momentum/molecular diffusion. However, in the turbulent flow, the power dissipation is also affected by the interaction between eddies.

The basis of micromixing is diffusion which occurs when the size of eddies is small enough so that the convective mixing is no longer the effective mechanism. The smallest size of eddies before the viscous effect becomes important is equivalent to the Kolmogorov scale: [52]

$$\lambda_K = \left(\frac{\upsilon^3}{\varepsilon}\right)^{0.25} \tag{1-7}$$

where υ is the kinematic viscosity, and ε is the power dissipation. When the size of eddies becomes smaller than λ_K, the effect of momentum diffusion gradually diminishes, and molecular diffusion will be the only term affecting micromixing. The smallest size of eddies before the molecular diffusion becomes the only affecting term is obtained by the Batchelor scale: [52]

$$\lambda_B = \left(\frac{\upsilon \mathcal{D}}{\varepsilon}\right)^{0.25} = \lambda_K Sc^{-0.5} \quad (1\text{-}8)$$

where $\mathcal{D}$ is the molecular diffusivity and Sc is the Schmidt number. If the size of eddies is less than λ_K, both momentum and molecular diffusions affect micromixing, while for sizes less than λ_B, only molecular diffusion determines the characteristics of micromixing. Considering λ_K as the largest scale of micromixing, the diffusion between eddies and their environment occurs at maximum across half the maximum eddy size. Therefore, the maximum mixing time (or characteristic micromixing time) can be calculated as follows: [53]

$$\tau_{mix} = \frac{(0.5\lambda_K)^2}{\mathcal{D}} \quad (1\text{-}9)$$

τ_{mix} is not the exact micromixing time, instead, it provides an order of magnitude of the real micromixing time which is obtained experimentally. Although the mean residence time of a reactor is used to non-dimensionalize the experimental micromixing time, τ_{mix} seems to be a better choice for this purpose, because it can normalize the experimental micromixing time. The weak dependency of λ_K on the power dissipation in Equation (1-8) (because of its small exponent) implies that λ_K varies over a limited range from 5 to 50 microns for many industrial processes. [54] Considering typical diffusivity for low viscosity liquids, complete mixing takes place within milliseconds. For very fast reactions whose reaction times are faster than the micromixing time, the mixing phenomenon limits the overall rate of reaction, and these reactions are called mixing-limited reactions. Therefore, the micromixing quality affects the selectivity of competing reactions in a reaction medium. [55] As a result, establishing a desired macromixing condition such as high plug flow is often sufficient for good mixing, but it does not necessarily guarantee any perfect mixing in the microscopic scale (micromixing). [25] Consequently, measuring the concentration of species in the reaction medium cannot lead to the characterization of micromixing. Instead, some other methods are employed to qualitatively/quantitatively study micromixing in microreactors: [25]

- Visually tracking a dye
- Reactions producing colored materials
- Competing reactions

Using these methods, the micromixing time can be determined in a single-phase medium. The first two experimental methods do not provide satisfactory results in the presence of oscillation. [56] Therefore, the third one can be used to study the micromixing behavior of the reactor.

Two schemes of competing reactions sets are commonly used in the literature: competitive-consecutive and competitive-parallel:

Competitive-consecutive:

$$A + B \xrightarrow{k_1 \to \infty} R \qquad (1\text{-}10)$$

$$R + B \xrightarrow{k_2} S$$

Competitive-parallel:

$$A + B \xrightarrow{k_1 \to \infty} R \qquad (1\text{-}11)$$

$$C + B \xrightarrow{k_2} S$$

The first reactions in both schemes are quasi-instantaneous, and the rate of the second ones is comparable to the one of the micromixing phenomenon. Therefore, the reaction time of the first reaction is almost zero (i.e. always mixing limited) while that of the second reaction is almost equal to the mixing time (i.e. sometimes mixing limited). Several examples of the two schemes have been tabulated in a study [57] along with their rate constants, allowing for brief comparison and choosing a proper set of reactions. Some sets of competing reactions used in the literature are not fast enough to evaluate the mixing quality; [57] therefore, they are not widely used. The use of parallel reactions is favored because the kinetics of the second reaction is independent of the first one. Overall, to decrease the sensitivity of fast reactions to mixing, it is necessary to bring τ_{mix} considerably below (orders of magnitude) the characteristic reaction time to ensure that the reaction is rate-limited.

To characterize micromixing phenomena, two types of mathematical models have been proposed in the literature. Models of the first type quantitatively describe the earliness of

mixing, meaning how early a fluid in a reactor is mixed with the reaction medium. Those of the second type determine the time evolution of the concentration of species present in the reaction medium.

The micromixing models describing the earliness of mixing are based on the definition of two types of fluid produced after mixing. When two fluids enter a vessel and become macroscopically homogeneous, two circumstances may take place. If the two fluids also become microscopically homogeneous such that every molecule can move freely in the mixture and come in contact with other ones, this type of mixing is called maximum mixedness and the product of mixing is called micromixed fluid or microfluid. [47,49,58] Nonetheless, a macroscopically homogenized mixture may remain grouped into aggregates that have a very small macroscopic size but contain a very large number of molecules. These aggregate or segregated domains can move freely in the continuous medium of the other one without any molecular exchange or interaction among them, meaning that the molecules belonging to a given segregated domain remain bound to it and have the same age (residence time) as the domain. This type of mixing is named complete segregation, and the product of such mixing is completely segregated fluid or macrofluid. [47,49,58] An example of such a fluid is an emulsion of two immiscible fluids without any interaction (like mass transfer, agglomeration, and breakage) among the disperse fluid droplets. In practice, every real fluid has an intermediate state between a micro- and macrofluid. **Figure 1-12** shows the micromixed and segregated fluids schematically.

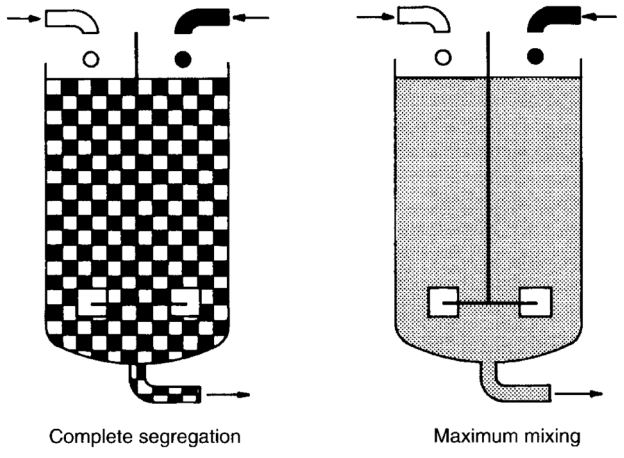

Figure 1-12. The two extreme states of mixing from the spatial standpoint. [49]

To completely characterize the segregation state of a fluid, two parameters must be considered: segregation intensity and segregation scale. The former describes to what extent the fluid is segregated, the highest value (generally normalized at 1) refers to a fully segregated fluid while very small values near zero show maximum mixedness. The segregation intensity can be shown by the degree of segregation: [49]

$$J = \frac{variance\ of\ the\ ages\ of\ the\ aggregates}{variance\ of\ the\ ages\ of\ the\ molecules} \tag{1-12}$$

For complete segregation, J = 1, and for maximum mixedness J = 0. The second parameter is the segregation scale which is associated with the size of aggregates. **Figure 1-13** schematically displays how the segregation scale and intensity affect the state of the fluid. These two types of mixing products delineate two extremes for mixing processes so that two micromixing models have been proposed based on their concepts.

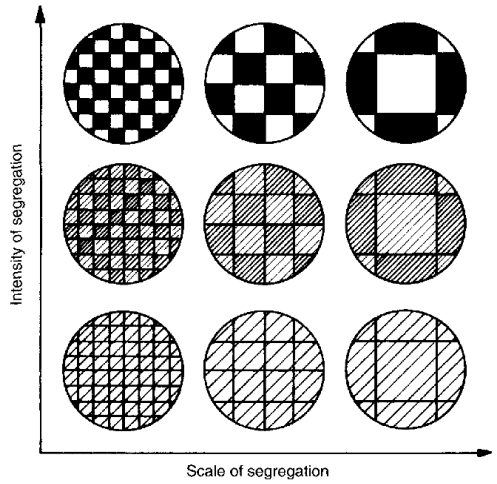

Figure 1-13. Schematic representation of the segregation intensity and scale. [49]

Segregation Model: This model assumes that the reaction medium remains fully segregated from the inlet to the outlet of a reactor. If the residence time distribution of the reactor ($E(t)$) and the kinetics of the reaction ($X(t)$: time evolution of conversion) are given, this model can predict the reaction conversion if the medium remains fully segregated: [58]

$$X_{seg} = \int_0^\infty X(t)\, E(t)\, dt \tag{1-13}$$

Maximum Mixedness Model: This model assumes that when two fluids enter a vessel or if a fluid is added to a medium, molecular homogeneity over the entire volume of the

vessel/medium occurs instantly (within a very short time approaching zero). By specifying the RTD of the reactor and the reaction kinetics (r_A), the reaction conversion is predicted as follows: [58]

$$\frac{dX_{mm}}{dt} = \frac{r_A}{C_{A0}} + \frac{E(t)}{1 - F(t)} X_{mm} \qquad Boundary\ Condition: t \to \infty : \ X_{mm} = 0 \qquad (1\text{-}14)$$

where $F(t)$ is the cumulative residence time distribution ($dF(t)/dt = E(t)$). For an ideal CSTR with a single-phase reaction, the reaction medium is a micromixed fluid and its conversion is consistent with the maximum mixedness model. For an ideal plug flow reactor, the reaction medium is fully segregated in the axial direction but micromixed in the radial direction. [49] Therefore, segregated domains for this reactor can be considered infinitesimal longitudinal slices. For every slice, the residence times of its molecules are the same as that of the slice itself which is consistent with the definition of the segregated fluid. Therefore, the conversion of a plug flow reactor is consistent with the one predicted by the segregation model.

1.2.3.3. Mesomixing

There are significantly fewer studies and quantitative interpretations of the mesomixing process. However, its quantitative description is similar to the one of micromixing with a different definition of characteristic length. If mixing occurs through the injection of a liquid into the tubular reactor (**Figure 1-14**), the dimensionless characteristic scale is defined as follows: [50]

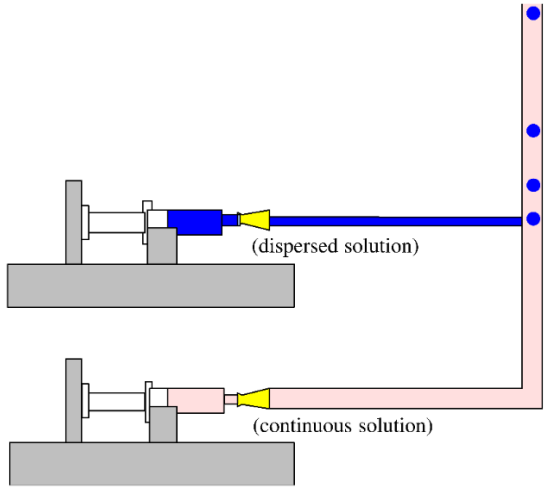

Figure 1-14. An example of mesomixing in a continuous tubular reactor. [50]

$$L^* = \frac{u_d}{u_t} \tag{1-15}$$

where u_d is the velocity of the disperse fluid and u_t is the velocity in the main channel. The selectivity of two competing reactions can be determined at different values of L^* to investigate the contribution of mesomixing effects.

1.2.4. Heat Transfer

As stated before, an oscillatory flow allows the quality of mixing, heat transfer, and mass transfer rates to be decoupled from the net flow rate. [21] Therefore, measuring the fluid-to-wall heat transfer coefficient shows to what extent, applying oscillation can enhance transport phenomena, particularly, heat transfer. Similar to the micromixing topic, there is no article in the literature specifically addressing the heat transfer in oscillatory flow coil reactors. Nonetheless, it has been demonstrated that the convective heat transfer coefficient is enhanced by the secondary flow created in curved pipes. [59,60] For a straight pipe followed by a curved pipe, the Nusselt number at low values of De is lower than or approximately equal to the one of the straight pipe. However, by increasing De, it increases in the curved part. In addition, the local Nusselt number in the curved part is higher near the concave wall relative to the convex one because of the higher velocity near the concave wall.

As the secondary flow affects the fluid-to-wall heat transfer coefficient, the formation of the secondary flows due to oscillation is expected to considerably affect it because the maximum oscillation velocity for oscillatory flow reactors is more than the net flow velocity. [46] In a recent article, the enhancement of the convective heat transfer coefficient for an oscillatory flow baffled reactor has been studied. [61] Based on the results provided, for a studied range of the net flow Reynolds number, the profile of the Nusselt number vs. the oscillatory Reynolds number has a maximum point, meaning that there is a small range of operating conditions in which the convective heat transfer coefficient is maximized. Accordingly, measuring the heat transfer between an oscillatory flow coil reactor and a fixed temperature external medium will be included in this research aiming to better understand the relationship between secondary flows and heat transfer and provide correlations in order to predict the heat transfer coefficient under oscillatory conditions which is very useful for

scale-up purposes. Because scaled-up equipment has a lower surface-to-volume ratio, the enhancement of the fluid-to-wall heat transfer coefficient is highlighted to prevent the needs to oversize reactors for heat transfer purposes.

1.2.5. Solid-Forming Reactions

Since the micromixing quality affects the selectivity of reactions in a reaction medium, [55] it can be an important factor in controlling the crystallization performance of solid-forming reactions. [62] Accordingly, solid particle properties such as PSD can be more precisely controlled in micro-reactors as there is greater control over mixing conditions, heat and mass transfer, and particle nucleation/growth. [63] When the plug flow performance increases, the reactants of different ages are not mixed, therefore, the obtained particle size distribution is expected to be narrower. [20] A recent study shows that high plug flow performance is quite attainable in relatively short-length coil reactors by employing proper oscillatory conditions. [44] Therefore, an oscillatory flow coil reactor can produce monodisperse PSDs provided that proper dimensions and operating conditions are selected.

Although the characteristics of miniaturized reactors such as high surface area and low hold-up appear to effectively improve heat transfer and mixing conditions, they can increase the risk of fouling and clogging in the presence of solid particles, especially in microreactors consisting of small channels and a number of micromixer units. [39] Plain coils have the advantage that there are no inserts or other micromixer elements inside them, and their diameter remains constant along the reactor. Therefore, the mentioned risks caused by internal parts or diameter changes are reduced. Nevertheless, they have a high ratio of surface area to volume and a low diameter. Thus, the risk of fouling as well as the risk of clogging caused by particle aggregation is still considerable. Strategies that have been used to help avoid plugging in microreactors include ultrasonic systems, buffer fluid flow to avoid direct contact with the wall, and periodic purges. [63–65] In addition, producing particles with a narrow PSD is favored because, in the presence of mono-size particles, the number of large particle aggregates decreases, leading to less risk of plugging. [39] In summary, the use of an oscillatory flow coil reactor for producing solid particles has the following advantages:

- There are no inserts or fixed internal parts inside them.

- Applying oscillation can improve the plug flow performance, leading to narrow PSDs as well as a low risk of clogging.
- Oscillatory flow provides additional shear at walls and more mixing within the fluid which should decrease the risk of fouling.

The selection of a solid-forming reaction to study oscillatory flow coil reactors is based on a toolbox approach developed by Plouffe et al. [7] This approach guides selection of microreactors based on a few criteria, firstly the rate of reaction. Reactions are categorized into three types based on the rate of reaction. Type A reactions have intrinsic reaction rates of milliseconds to seconds and are generally mass transfer limited (mixing limited). Reactors with rapid mixing and heat transfer are most appropriate for this type of reaction. Type B reactions have an intrinsic reaction rate of several seconds to minutes and impact the overall rate in single-phase reaction media. While a selected reactor should provide proper heat transfer and mixing for Type B reactions at the entrance, it must have a sufficient residence time to allow the reactions to reach high conversions. Type C reactions have an intrinsic reaction rate of several minutes to hours. Reactions of this type can benefit from increased temperature to increase the reaction rate. [7]

1.3. Research Objectives and Methodology

Based on the literature review performed in this research, there are not sufficient studies on the transport phenomena in oscillatory flow coil reactors which are promising choices for intensifying fine chemical reactions. The lack of comprehensive empirical models to predict the behavior of oscillatory flow coil reactors in terms of macromixing, micromixing and heat transfer, and the need for understanding connections between the flow field and mixing phenomena led to the objectives of this research:

1. The study of mixing conditions and the axial dispersion in oscillatory flow coil reactors with different dimensions at different operating conditions using the residence time distribution analysis in order to investigate the flow pattern of the reactor and create a baseline to size a reactor and predict the particle size distribution for solid-forming reactions.

2. The determination of viscous power dissipation and phase shift using a simplified model and CFD simulation under oscillatory conditions in a single-phase medium to better understand the relationship between the instantaneous flow field, power dissipation and the RTD variance.
3. The study of the convective fluid-to-wall heat transfer between the reaction medium of a coil reactor and a constant-temperature external environment in the presence and absence of oscillation to evaluate the extent of heat transfer enhancement in the presence of oscillation.
4. Experimental study of a solid-forming reaction (multi-phase medium) in a coil reactor to study particle size distribution at both oscillatory and non-oscillatory conditions.

The first part of this research is thus the characterization of mixing conditions and the degree of reaction conversion in this reactor using the analysis of residence time distribution (RTD). To obtain the RTD of a continuous reactor at specified operating conditions, it is conventional that a change is applied at the inlet of the reactor and the response to the change is measured at its outlet. A qualitative and quantitative comparison between the actual and expected responses reveals the plug flow performance and axial dispersion which occurs along the reactor. The comparison is feasible after converting the response data to normalized curves named exit time distribution or E-curves. The obtained E-curves can be characterized by models provided for the study of RTDs.

After determining the mixing conditions of the coil reactor at oscillatory and non-oscillatory conditions, the performance of the reactor in terms of achieving plug flow is compared to a recent study [44] which has been conducted with different coil dimensions at different operating conditions. In addition, the plug flow performance of the reactor is also compared to some recent articles that have studied straight coils, [39,40] coiled flow inverters (CFI), [40,42] and compact coiled flow inverters (CCFI) [42] to compare the plug flow performance of the oscillatory flow coil reactor benefiting from an active method with the ones of CFI and CCFI that utilize only a passive method. Finally, the performance of the reactor during some hypothetical reactions will be evaluated using the segregation and maximum mixedness micromixing models.

The study of power dissipation and phase shift between the pressure drop and velocity profiles in an oscillatory flow coil will be performed using two methods: CFD simulation and mechanical energy balance. CFD simulations will initially result in instantaneous axial and transverse velocity profiles and pressure drop gradient along the coil. The phase shift obtained from the CFD simulation will be also compared to the results from the mechanical energy balance. Finally, the behavior of viscous power dissipation as a key parameter in micromixing will be investigated in connection with the RTD variance as a measure of macromixing.

To study of the oscillatory heat transfer, first a set of non-oscillatory flow experiment will be performed to prepare a basis of evaluating the heat transfer enhancement under oscillatory conditions. Then, the effect of the oscillatory operating conditions (net flow rate, frequency, and amplitude) on the heat transfer will be investigated to study the impact of these parameters on the heat transfer coefficient and elucidate the governing physical mechanisms. The enhancement of the heat transfer coefficient will be correlated with the operating conditions and coil geometry to provide a robust basis for reactor design and scale-up.

The first three parts of this research are in fact essential bases for the last part: performing a solid-forming reaction under oscillatory flow conditions. For this part, a Type A solid-forming reaction will be selected and performed in a coil reactor under non-oscillatory and oscillatory conditions. The particle size distribution under oscillatory and non-oscillatory conditions will be then investigated and potentially correlated with the operating conditions. Some operability test at a high reagent concentration will be also performed to evaluate to what extend oscillation can decrease the risk of blocking.

Nomenclature

Latin Letters

C_{A0}	mol·L^{-1}	initial concentration of reactant A
$d_{t,i}$	mm	tube inner diameter
$\mathcal{D}$	m^2·s^{-1}	diffusivity
De	-	Dean number
De_o	-	oscillatory Dean number
E	-	exit time distribution function (RTD)/ engulfment rate
f	Hz	oscillation frequency
F	-	cumulative residence time distribution
J	-	degree of segregation
k	s^{-1} (mol·L)$^{(1-n)}$	reaction rate constant
L	m	tube length
L^*	-	dimensionless mesomixing scale
$\dot{m}$	g·min^{-1}	mass flow rate
P_t	mm	tube pitch
Q	m^3·min^{-1}	volumetric flow rate
r	m	radial position
r_A		reaction rate of component A
$r_{t,i}$	mm	tube inner radius
r'		cylindrical toroidal coordinate
R_c	mm	coil radius
Re_n	-	net flow Reynolds number
Re_o	-	oscillatory Reynolds number
R'		cylindrical polar coordinate
Sc		Schmidt number
S_n		swirl intensity
t	s	time
u	m·s^{-1}	local flow velocity
u_d	m·s^{-1}	disperse fluid velocity (mesomixing)
u_n	m·s^{-1}	net flow velocity
u_o	m·s^{-1}	oscillatory flow velocity
$u_{o,max}$	m·s^{-1}	maximum oscillatory flow velocity
u_t	m·s^{-1}	velocity in main channel (mesomixing)
V	m^3	reactor volume
Wo	-	Womersley Number
x_o	mm	oscillation amplitude
X	-	conversion
X_{mm}	-	completely micromixed flow reaction conversion
X_{seg}	-	completely segregated flow reaction conversion
Z'		cylindrical polar coordinate

Greek Letters

α	-	cylindrical toroidal coordinate
ε	W·m^{-3}	power dissipation

θ	-	dimensionless time / cylindrical polar coordinate / cylindrical toroidal coordinate
θ_m	-	dimensionless mean residence time
θ_{min}	-	dimensionless t_{min}: when the response is sensed
θ_{max}	-	dimensionless t_{max}: when the response disappears/reaches steady state
λ_B	m	Batchelor scale
λ_K	m	Kolmogorov scale
μ	Pa·s	viscosity
υ	$m^2 \cdot s^{-1}$	kinematic viscosity
ρ	$kg \cdot m^{-3}$	density
σ_θ^2	-	variance of E-curve
τ_{mix}	ms	characteristic mixing time
Ψ		velocity ratio
Ω	s^{-1}	flow angular speed
Ω_o	s^{-1}	pulsator angular speed

Abbreviations

CCFI	coiled flow inverter
CFI	compact coiled flow inverter
PSD	particle size distribution
RTD	residence time distribution

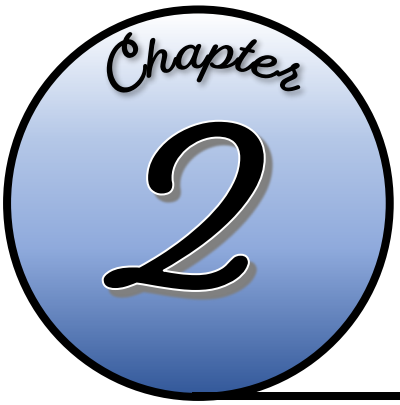

Residence Time Distribution

2.1. Introduction

Process intensification aims to enhance reactor space-time yields and energy efficiencies via methods such as synergistic combination and/or volume reduction of equipment, selection of alternative reaction pathways, and operation at greater temperature, pressure and concentration.[10–12,66] The fine chemical and pharmaceutical industries can benefit from process intensification as there are many batch operations, some short-lived, at relatively mild conditions and small production capacities. There are thus efforts to render these processes, or at least some of the unit operations, continuous and intensified to benefit from the lower material holdup and smaller transport scales. [14–17] A continuous and dedicated manufacturing process can also be advantageous when producing a single compound or a limited number of compounds at similar operating conditions to better respond to fluctuating market demand and reduce the lead-time associated to multi-purpose batch equipment. [19]

Miniaturized structured mixers and serpentine channels in plates have been used for miscible and immiscible fluids, especially when a plug flow pattern and rapid transport rates are desired. [67] On the other hand, small-scale coil and stirred tank reactors have been employed, each depending on desired flow pattern, for slower reaction rates with longer residences time, and/or when solids are present. [20,68] Mixing rates are controlled via passive and active energy inputs, where both macroscopically affect the fluid velocity magnitude and/or direction. Passive mixing takes advantage of the energy from a pump moving the fluid forward by inducing mixing through changes in flow channel geometry, while active mixing uses energy from an additional external source. [21] For a given working volume, active mixers thus dissipate power for the desired transport phenomena independently of the fluid nominal residence time.

A coil operated in continuous oscillatory flow is a promising contactor for intensifying fine chemical reactions as both passive and active mixing occur and there is ease of cleaning and lower probability of fouling. [20,68] Most experimental and numerical research in oscillatory flow reactors have central mixing elements such as integral (periodic constrictions of the wall), [69–73] central axial, helical, or single/multiple orifice baffles. [25,74–79] The few and recent studies on baffleless oscillatory flow reactors experimentally investigated the tube

geometry and oscillatory flow conditions that minimize liquid [44,80] and solid [81] axial dispersion while avoiding particle sedimentation. The objective of this study is thus to determine the impact of an expanded range of oscillatory flow conditions in a baffleless coil on liquid macromixing via analysis of the residence time distribution (RTD). The RTD is analyzed with a statistical model considering the limitations of the axial dispersion model. [82] The interpretation of the experimental data is also supported by numerical evidence obtained from simulations of the instantaneous three-dimensional liquid flow field. The liquid RTD statistical model parameters are correlated to an oscillatory flow dimensionless number, a normalized coil geometry, and net flow rate for greater generality. Finally, the conversion performance of the coil for first- and second-order single phase reactions is assessed using the segregation and maximum mixedness micromixing models combined with selected experimental RTDs.

2.2. Experimental and Numerical Methodologies

2.2.1. Equipment, materials, and experimental procedure

Residence time distributions were measured at different oscillation intensities in a coiled tubular reactor made of Hastelloy ($V = 409$ mL, $L = 24$ m, $d_t = 4.57$ mm, $R_c = 154.2$ mm, $P_t = 10$ mm) using a feed pump (HNP mzr-7255 micro annular gear pump), a mass flow controller (Endress & Hauser Promass 83A Coriolis MFC), a pulsator pump (LEWA LDB1 pulsator pump), and a 2-electrode conductivity sensor (Endress & Hauser CLS82D conductivity probe) equipped with a transmitter (Endress & Hauser CM444 transmitter). **Figure 2-1** shows a sketch of the experimental setup, with all data acquired and stored on a personal computer.

Two aqueous fluids were selected to apply negative/positive step changes in conductivity of the feed to the reactor: deionized water with a conductivity near zero, and 0.05% w/w NaCl solution with a conductivity around 950 µS/cm at 25°C. Experiments were conducted at three net mass flow rates: 30, 60, and 120 g·min^{-1}. For each net flow rate ($\dot{m}$), experiments without oscillation and 15 combinations of oscillation frequencies (f) and amplitudes (x_o) were performed (see **Table 2-1**). The flow amplitude (x_o) is the fluid length displacement in the coil divided by 2, with the latter determined using the pulsator pump discharge volume per stroke and the coil cross-sectional area. Around 15% of the experiments were repeated

four times to assess precision of the results; the average relative standard deviation of the first and second moments of the residence time distributions are respectively 0.6 and 5%.

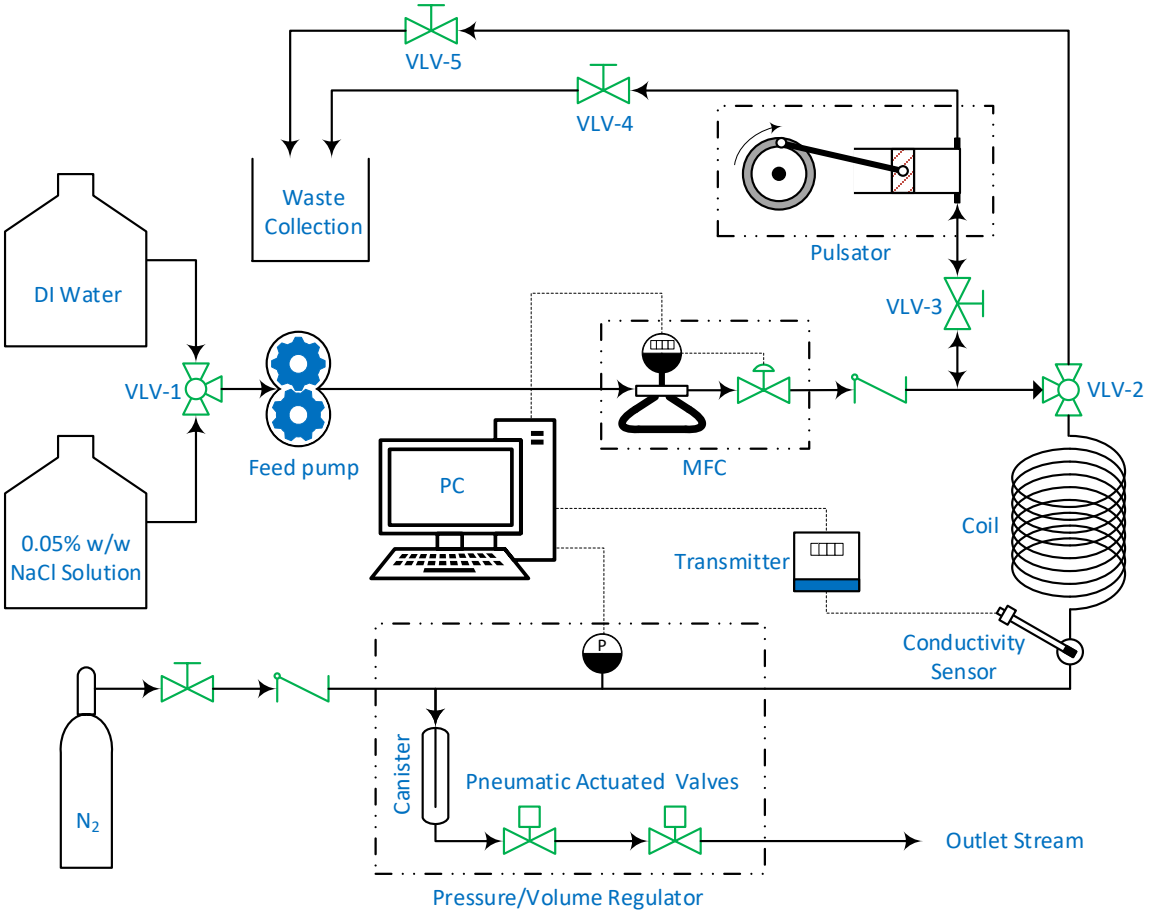

Figure 2-1. Schematic representation of the experimental setup.

Table 2-1. Oscillation conditions considered for all net flow rates $\dot{m} = 30, 60, 120$ g·min^{-1}.

f (Hz)	x_o (mm)				
1.23	11.75	23.50	35.25	47.00	58.75
2.46	11.75	23.50	35.25	47.00	58.75
3.68	11.75	23.50	35.25	47.00	58.75

Prior to starting an experiment, the coil was filled with a desired first fluid by starting the feed pump and opening VLV-1 and VLV-2 towards the coil. Then all the lines up to the coil entrance (VLV-2) including the feed line, the line leading to the pulsator and inside the pulsator were filled with the other fluid by simultaneously switching VLV-1 and VLV-2 and opening VLV-3, VLV4, and VLV-5 to lead the second fluid toward the pulsator and the coil

entrance and finally the waste tank. After this step, the feed pump was turned off and only VLV-4 and VLV-5 were shut. An experiment was started by simultaneously opening VLV-2 toward the coil, starting the feed pump at the desired flow rate, and the pulsator at a specified frequency and amplitude as well as supplying nitrogen for the regulator located at the outlet stream. From this time ($t = 0$) onward, the time evolution of the conductivity of the outlet stream was logged continuously. The end of the experiment was when the conductivity of the outlet stream reached a steady state after observing the response to the applied step change.

2.2.2. Data analysis and RTD model selection

The response to the fluid step change yields the cumulative residence time distribution (F-curve), while the associated E-curve (RTD) is obtained by the differentiation of the F-curve (the procedure is shown in Appendix A). [47] The mean residence time $\bar{t}$ was used to render time dimensionless ($\theta = t/\bar{t}$) such that the first moment of the RTD (i.e., θ_m) is equal to unity.

$$\theta_m = \int_{\theta_{min}}^{\theta_{max}} \theta\, E(\theta)\, d\theta = 1 \tag{2-1}$$

where θ_{min} and θ_{max} are the dimensionless terms of t_{min} and t_{max}, when the conductivity at the reactor outlet starts to change and reaches steady state within a measurement error of 0.05 %, respectively. RTD data from a reactor are often analyzed using one-parameter models such as the axial dispersion or tanks-in-series model. [47] If deviation from plug flow is very low (i.e., $Pe = uL/D > 100$ or $\sigma_\theta^2 < 0.02$), the $F(\theta)$ and $E(\theta)$ functions obtained from the axial dispersion model are as follows: [47]

$$F(\theta) = \frac{1}{2}\left(1 + \mathrm{erf}\left(\frac{\theta - 1}{\sqrt{4\frac{D}{uL}}}\right)\right) \tag{2-2}$$

$$E(\theta) = \frac{1}{\sqrt{4\pi\frac{D}{uL}}} \exp\left(-\frac{(1-\theta)^2}{4\frac{D}{uL}}\right) \tag{2-3}$$

For $Pe > 100$, the axial dispersion model creates a narrow symmetrical RTD with the mode located at $\theta = 1$. In practice, a very narrow RTD does not necessarily lead to symmetry. Alternatively, several models, that are mostly empirical, have been suggested to better fit the F-curve to experimental data. [83] A disadvantage of empirical models is that some parameters lack physical meaning, whereas some existing statistical models can quantitatively describe the tailing and skewness of an RTD using meaningful and correlatable parameters. Among a few statistical models tested in this work, the skewed normal distribution function (an adjusted form of the symmetrical distribution) provides an excellent fit: [84]

$$F(\theta) = \Phi\left(\frac{\theta - \xi}{\omega}\right) - 2\,T\left(\frac{\theta - \xi}{\omega}, \alpha\right) \tag{2-4}$$

$$E(\theta) = \frac{1}{\omega\sqrt{2\pi}} \exp\left(-\frac{(\theta - \xi)^2}{2\omega^2}\right)\left(1 + \operatorname{erf}\left(\frac{\alpha(\theta - \xi)}{\omega\sqrt{2}}\right)\right) \tag{2-5}$$

where

$$\Phi\left(\frac{\theta - \xi}{\omega}\right) = \frac{1}{2}\left(1 + \operatorname{erf}\left(\frac{\theta - \xi}{\omega\sqrt{2}}\right)\right) \tag{2-6}$$

T is a two-argument function defined by Owen: [85]

$$T\left(\frac{\theta - \xi}{\omega}, \alpha\right) = \frac{1}{2\pi}\int_0^{\alpha} \frac{\exp\left(-\frac{1}{2}\left(\frac{\theta - \xi}{\omega}\right)^2 (1 + x^2)\right)}{1 + x^2}\,dx \tag{2-7}$$

The role of the kurtosis ω^2 is similar to $2D/uL$ and changes the width and height of the E-curve. The location parameter ξ is equal to 1 in the dispersion model and shifts the E-curve right or left if it deviates from unity. The shape factor α is a measure of skewness and makes the RTD right- or left-skewed for positive or negative values, respectively. Note that the peak of a right-skewed distribution inclines toward the left side in contrast to its tailing. To obtain the parameters of the skewed normal distribution function, the nonlinear generalized

reduced gradient algorithm present in Microsoft Excel was used with the objective that the sum of squared residuals is minimized. Proper initial values were required to converge to the correct model parameter values. As such, ω^2 was equated with the variance (σ_θ^2) calculated by Equation (2-8), ξ was considered unity as its value is near 1, and α greater than zero (generally 1) was given as all obtained RTDs were right-skewed. Fitting the experimental F-curve resulted in R^2 greater than 0.99 for all conditions, with **Figure 2-2** being an example.

$$\sigma_\theta^2 = \int_0^\infty (\theta - \theta_m)^2 E(\theta) d\theta \tag{2-8}$$

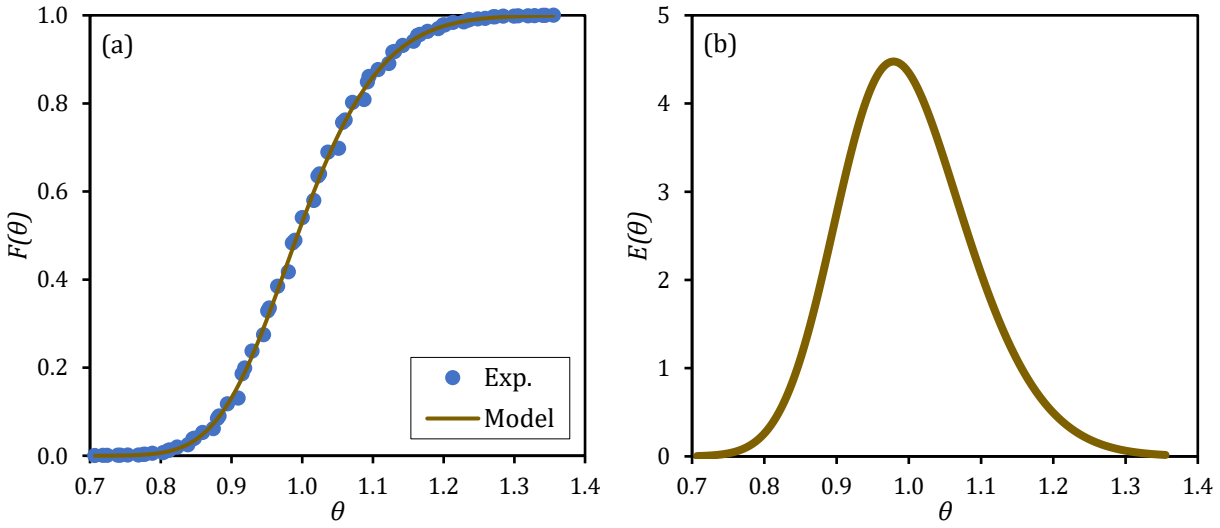

Figure 2-2. a. Experimental data and fitted F-curve by the skewed normal distribution model for the experiment at $\dot{m} = 30$ g·min^{-1}, $x_o = 58.75$ mm, and $f = 2.46$ Hz. b. Associated E-curve (RTD) generated.

2.2.3. Numerical Simulation

Transient incompressible flow was simulated using the *pimpleFoam* solver available in OpenFOAM. [86] This solver uses a combination of the pressure-implicit with splitting of operators (PISO) and semi-implicit-method-for-pressure-linked-equations (SIMPLE) algorithms to iteratively solve for the pressure and velocity fields at each time step. Neglecting gravity forces, the continuity and momentum equations for transient laminar incompressible flow can be written as follows:

$$\nabla \cdot \boldsymbol{U} = 0 \tag{2-9}$$

$$\frac{\partial \boldsymbol{U}}{\partial t} + \boldsymbol{U} \cdot \nabla \boldsymbol{U} = -\nabla p' + \nabla \cdot \nu[\nabla \boldsymbol{U} + (\nabla \boldsymbol{U})^T] \tag{2-10}$$

where $\boldsymbol{U}$ is the velocity vector, ν is the kinematic viscosity, and the modified pressure $p' = p/\rho$ is the pressure p normalized by density ρ.

For flow through straight tubes, the transition from laminar to turbulent flow occurs at Reynolds numbers greater than approximately 2300. For coiled tubes, this transition also depends on the curvature of the tube, and literature indicates that curvature stabilizes the flow and thereby delays the onset of turbulence. For the coil geometry investigated in this study, the correlation of Ito gives a critical Reynolds number greater than 5200. [87] Oscillatory conditions can destabilize the flow more than unidirectional conditions, but there is insufficient information in the literature about the laminar-to-turbulent flow transition for oscillatory flows in coils to predict when this transition occurs. Therefore, only conditions that provided $Re_n + Re_o < 5275$ were simulated for this study, and all simulations were performed without the use of a turbulence closure model. The simulated cases correspond to those listed in **Table 2-1**, but no cases with $x_o = 47$ mm were simulated because they were expected to fall within the trends given by other points. Additionally, the cases with $x_o = 58.75$ mm and $f = 3.68$ Hz were not simulated because $Re_n + Re_o > 7500$, which was deemed too high for applicability of the laminar model assumption without further validation.

Following a similar approach as Jimeno et al., [88] the inlet velocity was specified assuming instantaneously fully-developed laminar flow:

$$u_{in} = f(t, r) = 2(u_n + 2\pi f x_o \sin(2\pi f t))\left(1 - \frac{r^2}{r_t^2}\right) \tag{2-11}$$

Within the oscillation cycle, this boundary condition was applied to the inlet when the flow was forward, and a fixed pressure condition was used at the outlet. Conversely, when the flow was backward during the cycle, this condition was applied to the outlet, and a fixed pressure condition was used at the inlet.

Only three turns of the total coil length were simulated, and data were processed for the middle turn to eliminate the impact of the boundary conditions on the results. The results for the middle turn were confirmed to be independent of the boundary conditions by analyzing both the instantaneous pressure drop and velocity profiles over the oscillation cycle as well as the time-averaged pressure drop and velocity profiles for successive quarter turns. In all cases, the flow took no more than one half turn to develop, which is reasonable considering that the length-to-diameter ratio for a single turn of the simulated coil was approximately 210.

The computational mesh consisted of a modified O-grid that was extruded in the axial direction. A uniform axial resolution was maintained because data were only processed for the instantaneously fully-developed middle turn of the coil. The O-grid was graded towards the wall to ensure adequate resolution of the axial and secondary flow boundary layers. An image of the cross-section of the mesh that was used in the simulations is shown in **Figure 2-3**. This mesh had 829 440 cells.

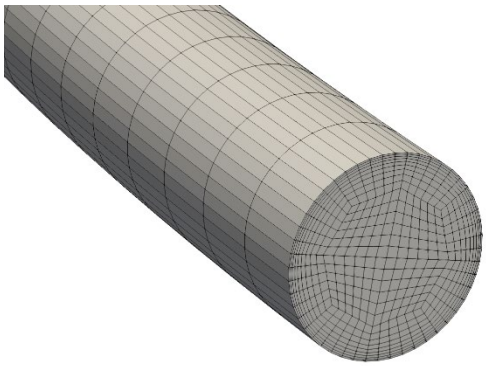

Figure 2-3. Cross-sectional view of the mesh used in all simulations other than the mesh dependence study (829 440 cells).

Mesh dependence was assessed for the case for the highest $Re_n + Re_o$ of approximately 5275: $x_o = 58.75$ mm, and $f = 2.46$ Hz. The four mesh resolutions listed in **Table 2-2** were used in the mesh resolution study. Following Plawsky [89] and neglecting gravity, the mechanical energy can be written as follows:

$$\underbrace{\int_V \frac{\partial}{\partial t}\left(\frac{1}{2}\rho\bar{\boldsymbol{U}}^2\right) dV + \int_V \left(\nabla\cdot\left(\frac{1}{2}\rho\bar{\boldsymbol{U}}^2\right)\boldsymbol{U}\right) dV + \int_V \nabla\cdot(p\boldsymbol{U})\, dV + \int_V \nabla\cdot[\boldsymbol{\tau}\cdot\boldsymbol{U}]\, dV}_{E_{ME}\,(Mechanical\ Power)} = \underbrace{\int_V (\boldsymbol{\tau}:\nabla\boldsymbol{U})\, dV}_{E_{\mu}\,(Viscous\ Power)} \quad (2\text{-}12)$$

Table 2-2. Mesh dependence of power dissipation predictions.

Mesh	Number of Cells	Viscous Power Dissipation, $\varepsilon_\mu = \frac{4E_\mu}{\rho\pi d_t^2 L}$ (W·kg^{-1})	Mechanical Power Dissipation, $\varepsilon_{ME} = \frac{4E_{ME}}{\rho\pi d_t^2 L}$ (W·kg^{-1})	$\frac{\lvert\varepsilon_\mu - \varepsilon_{ME,M4}\rvert}{\lvert\varepsilon_{ME,M4}\rvert}$ (%)
M1	245 760	1.330	1.507	11.74
M2	829 440	1.351	1.454	7.08
M3	2 877 120	1.378	1.452	5.10
M4	9 797 760	1.394	1.442	3.33

The term on the right-hand side of Equation (2-12) is the viscous dissipation. This term is strongly influenced by the accuracy of velocity and velocity gradient predictions. The first term on the left-hand side is equal to zero over an oscillation cycle. Summing the terms on the left-hand side of Equation (2-12) provides an alternative means to calculate the viscous dissipation. Avila et al. [90] noted that the third them on the left-hand side was dominant in their study on a different type of reactor. Similarly, in the present study, the third term was dominant, with the next largest term being three orders of magnitude lower. Avila et al. [90] also state that the third term on the left-hand side, which is based on the pressure drop, is much less sensitive to the mesh resolution than the viscous dissipation on the right-hand side. This is consistent with literature from many fields, where it is often reported that pressure gradients are easier to resolve than velocity gradients in CFD simulations. Therefore, the convergence of the viscous dissipation estimate (right-hand side of Equation (2-12)) towards the mechanical power dissipation estimate (sum of left-hand side of Equation (2-12)) for the finest mesh, both normalized by density, was used as an indicator of mesh convergence. As expected, the data in **Table 2-2** show little change in the mechanical power dissipation estimate with increasing mesh resolution. Conversely, the viscous power dissipation converges at a significantly slower rate. It would be ideal to use a mesh that fully resolves the viscous power dissipation, but this is impractical. In this study, mesh M2 was chosen considering that the mechanical power dissipation estimate is very close to the predictions from meshes M3 and M4 and that the offset of the viscous power dissipation estimate is well below 10%. It is also important to note that these differences would be significantly lower for all other cases because of the lower $Re_n + Re_o$ values.

To ensure temporal accuracy, the time step was specified to maintain a maximum Courant number below 0.5, and the second-order accurate Crank-Nicolson scheme was used. Second-order accurate schemes were used for discretization of all spatial terms. Within each time

step, sufficient pressure-velocity coupling iterations were performed to converge the scaled residuals to a tolerance of 10^{-4}. These specifications are consistent with current best practices for accurate simulation of transient flows. The results indicated that pseudo-steady state was reached after two oscillation cycles. Nonetheless, all simulations were performed for at least six oscillation cycles, and the data were time averaged over the last two cycles.

2.3. Results and Discussion

2.3.1. Observational impact of operating conditions (x_o, f, and $\dot{m}$) on the RTD

Figure 2-4 presents the evolution of the liquid mean residence time normalized by the space time ($\tau = V/Q$) at a net flow of 30 g·min^{-1} and different oscillation amplitudes and frequencies. Overall, $\bar{t}$ for both oscillatory and non-oscillatory flows are 2 to 6% greater than τ. A $\bar{t} < \tau$ implies that there are dead zones or shortcutting in the reactor, whereas $\bar{t} > \tau$ shows the combined experimental and computational errors. [47,51] As a result, the data suggest that the full volume of the reactor is active for reactions.

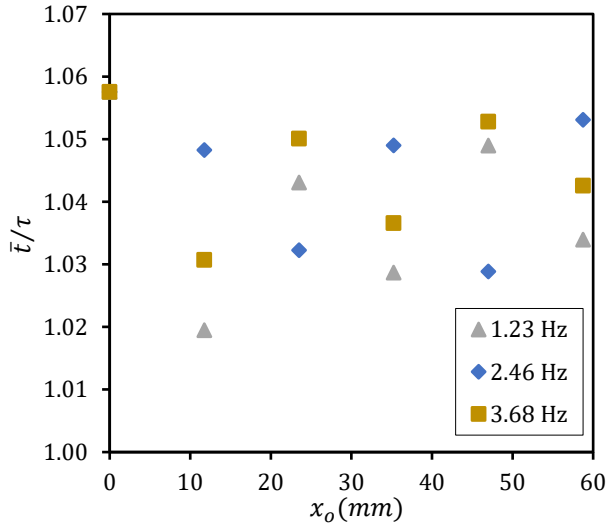

Figure 2-4. Ratio of the mean residence time to the space time ($\bar{t}/\tau$) at $\dot{m} = 30$ g·min^{-1} and several oscillation amplitudes and frequencies.

Figure 2-5-a shows the liquid residence time distributions at $\dot{m} = 30$ g·min^{-1}, $f = 1.23$ Hz, and several amplitudes. Relative to a non-oscillatory flow condition, an increase in oscillation amplitude initially leads to a narrower and taller E-curve. Further increases in amplitude eventually reverse the trend, where the E-curve now broadens and the peak value drops. At a given net flow rate and frequency, there is thus an amplitude at which the RTD is narrowest (σ_θ^2 is minimum, see **Figure 2-5-b**) and closest to a plug flow pattern, although all oscillatory

flow experiments are already near plug flow since their σ_θ^2 is less than 0.02. At some operating conditions, the amplitude that minimizes the RTD variance is rather blunt (i.e., greater practical range of x_o) such as shown in **Figure 2-6** for $\dot{m} = 60$ g·min^{-1} and $f = 3.68$ Hz where between amplitudes of 11.75 and 35.25 mm, the RTDs effectively overlap in terms of skewness, tailing, and location. The occurrence of a minimum σ_θ^2 agrees with the study performed by McDonough et al. [44] who used the one parameter tanks-in-series model to fit the E-curves and showed that oscillatory flow leads to a maximum number of tanks over a limited range of x_o.

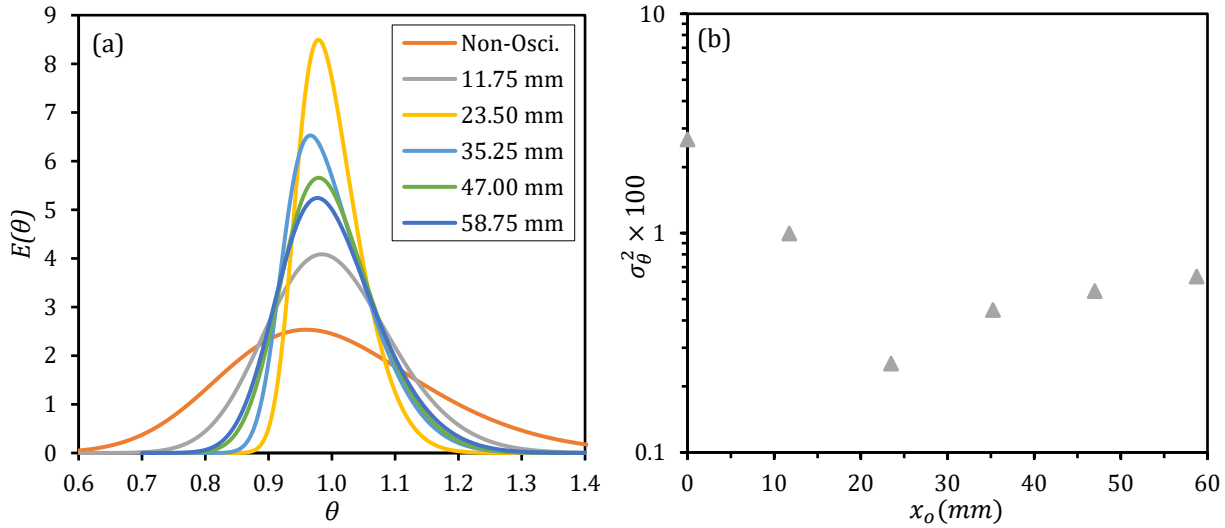

Figure 2-5. a. RTD for experiments at $\dot{m} = 30$ g·min^{-1}, $f = 1.23$ Hz, and several values of x_o. b. Evolution of σ_θ^2 as a function of x_o.

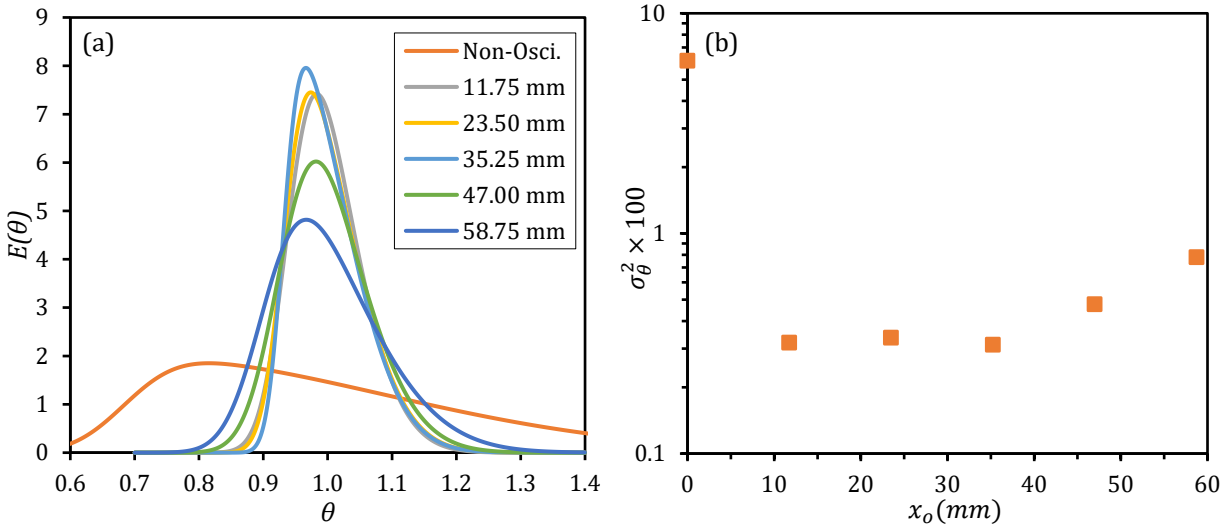

Figure 2-6. a. RTD for experiments at $\dot{m} = 60$ g·min^{-1}, $f = 3.68$ Hz, and several values of x_o. b. Evolution of σ_θ^2 as a function of x_o.

The impact of oscillation frequency on the RTD is shown in **Figure 2-7** at $\dot{m} = 120$ g·min^{-1} and amplitudes of 11.75, 35.25, and 58.75 mm. Overall, there is a progressive interaction between the effects of frequency and amplitude. At the lower amplitude, the RTDs become narrower and more symmetrical by increasing the frequency, where the modes gradually shift to $\theta = 1$ and become more late-happening. At the mid amplitude, the RTDs almost overlap suggesting that there is an amplitude (or a range of x_o) where the RTD is nearly independent of frequency. At the higher amplitude, the RTDs broaden with increasing frequency with potential position shifting.

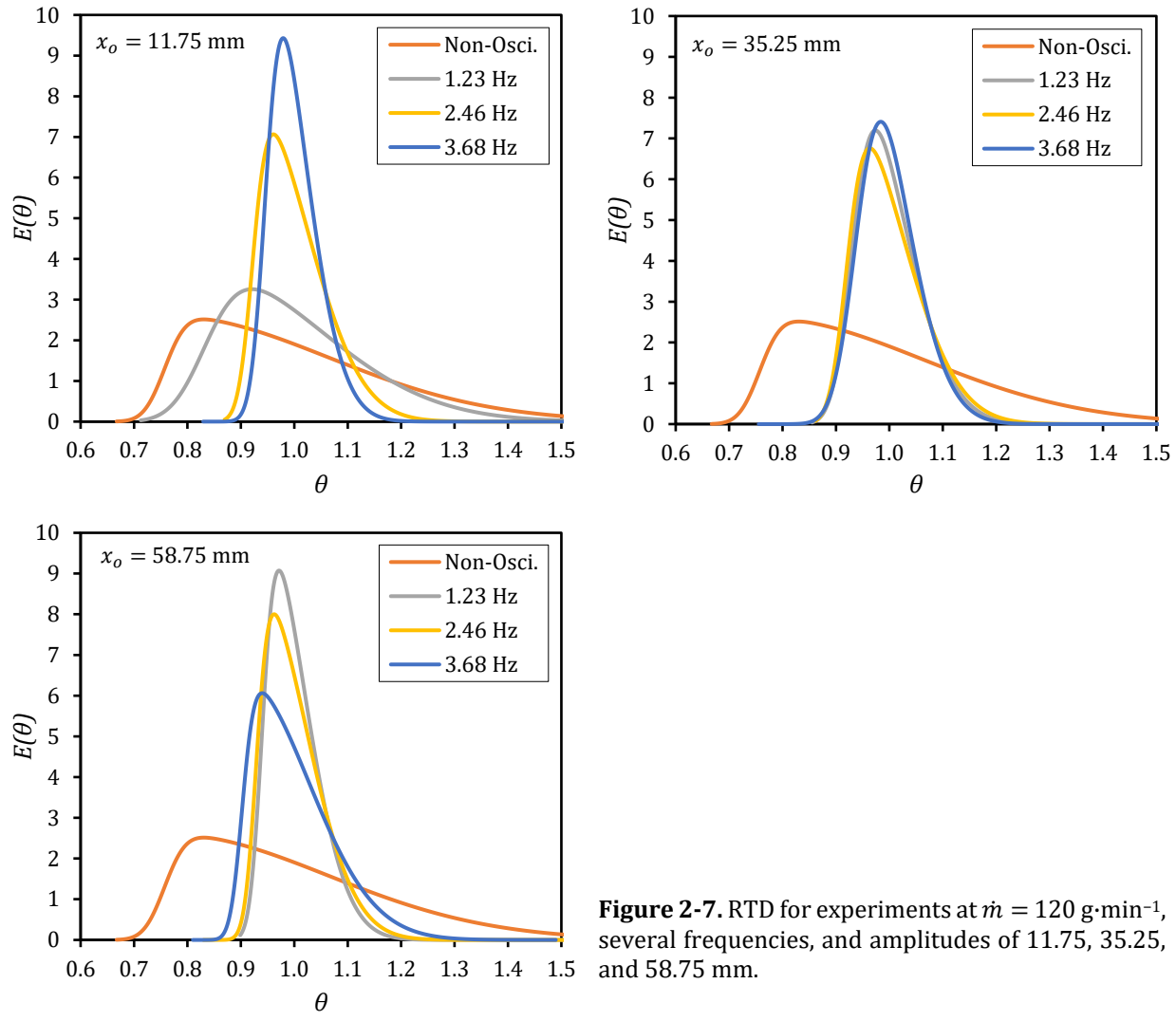

Figure 2-7. RTD for experiments at $\dot{m} = 120$ g·min^{-1}, several frequencies, and amplitudes of 11.75, 35.25, and 58.75 mm.

In a developing flow field, the thickness of the boundary layer is dependent on the distance passed by the fluid. [26] Since the flow field is always developing over an oscillation cycle,

the flow amplitude x_o (which is the fluid displacement divided by 2) is used as the characteristic length in the Reynolds number and the oscillation intensity is expressed as an oscillatory Dean number De_{ox} defined in Equation (2-13):

$$De_{ox} = Re_{ox}\sqrt{\frac{d_t}{2R_{c,cor}}} = \frac{2\pi f \rho\, x_o^2}{\mu}\sqrt{\frac{d_t}{2R_{c,cor}}} \tag{2-13}$$

where $R_{c,cor}$ (corrected radius of curvature) is the distance between the center lines of the coil and tube (R_c) corrected with the tube pitch (P_t), as defined in Equation (2-14) : [91]

$$R_{c,cor} = R_c\left[1 + \left(\frac{P_t}{2\pi R_c}\right)^2\right] \tag{2-14}$$

Figure 2-8-a presents the impact of the net mass flow rate on the RTD at $x_o = 58.75$ mm and $f = 1.23$ Hz. An increase in net mass flow rate leads to a narrower RTD. Interestingly, this observation arises when oscillatory conditions are after the range in which the minimum RTD variances occur (see **Figure 2-8-b** generated by Equation (2-16)); the trend reverses before that range where an increase in the net mass flow rate broadens the RTD (σ_θ^2 increases).

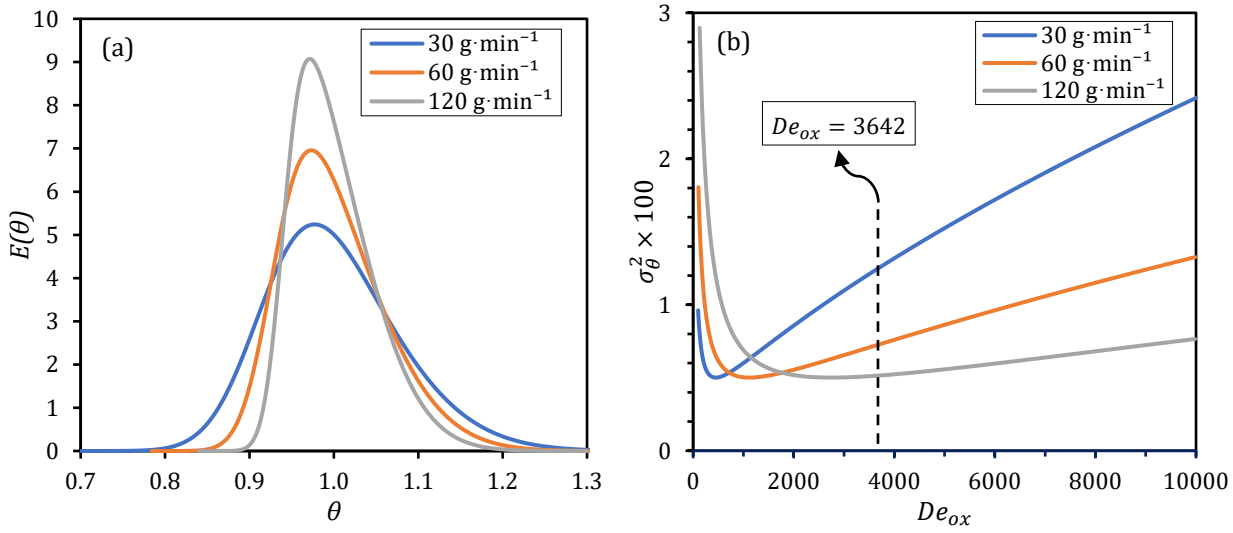

Figure 2-8. a. RTD for experiments at $x_o = 58.75$ mm, $f = 1.23$ Hz ($De_{ox} = 3642$), and several net mass flow rates. b. Impact of net mass flow rate on RTD variance for several oscillatory Dean numbers.

The flow fields from the CFD simulations in Section 2.3.2 provide some explanation to the trend in **Figure 2-8-b** where the time-averaged cross-sectional variance in axial velocity in **Figure 2-10** also presents a minimum as a function of De_{ox}. This minimum is dependent on the magnitude of gain in transverse relative to axial velocity, where the greater gains at lower net flow rates (see **Figure 2-13-b**) will lead to the minimum occurring at lower values of De_{ox}.

2.3.2. Discussion on the shape of the RTD and impact of the 3D flow field

The developed steady laminar flow field in a coil is affected by two factors: viscous effects and secondary flows when the Dean number is greater than around 40. [48] The internal flow boundary layer can then be separated into two zones: a near wall viscous layer where there is a considerable axial velocity radial gradient due to the no-slip condition at the wall and a central zone where the vortices occur and render the axial velocity spatially more uniform although with a swirling motion.

The coil geometry and operating conditions resulted in RTDs with variances (σ_θ^2) all below 0.02, indicating a near plug flow pattern. Nonetheless, deviation from ideality was observed in every RTD, with right-skewed asymmetry and relatively long tailing. A contributing factor to the RTD skewness is that the impact of axial dispersion in the forward direction is less than backwards for oscillatory flow. This can be related to the different fluid velocities during the suction and discharge stages. The net flow velocity is always in the forward direction, and accordingly the maximum flow velocity in the discharge half-cycle is $u_{f,max} = u_n + u_{o,max}$ ($u_{o,max} = 2\pi f x_o$) while in the suction half-cycle it is $u_{b,max} = u_n - u_{o,max}$. If two Peclet numbers are hypothetically defined for the forward and backward directions, Pe_f is always greater than Pe_b assuming equal dispersion coefficients in both half-cycles. This then suggests that the extent of axial dispersion in the forward direction is lower than backwards, leading to an RTD with a first half narrower than the second half, causing the right-skewness (illustrated in **Figure 2-9**). Data fitting using the skewed normal distribution function supports this thought as all experiments generated a shape factor α greater than zero.

Now considering the 3D instantaneous flow field generated by the numerical simulations, **Figure 2-10** displays the time-averaged variance of the simulated axial velocity profile $\overline{\sigma_{u_a}^2}$

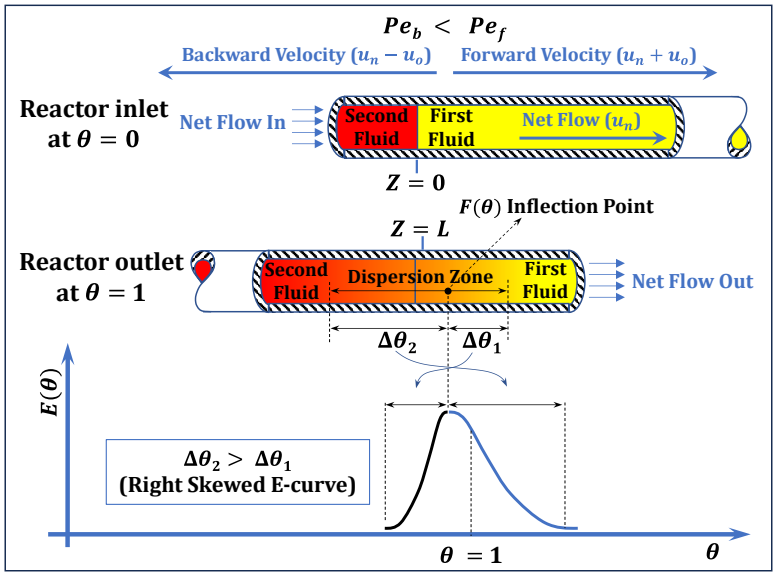

Figure 2-9. Schematic representation of a right-skewed RTD resulting from the difference between forward and backward fluid velocities.

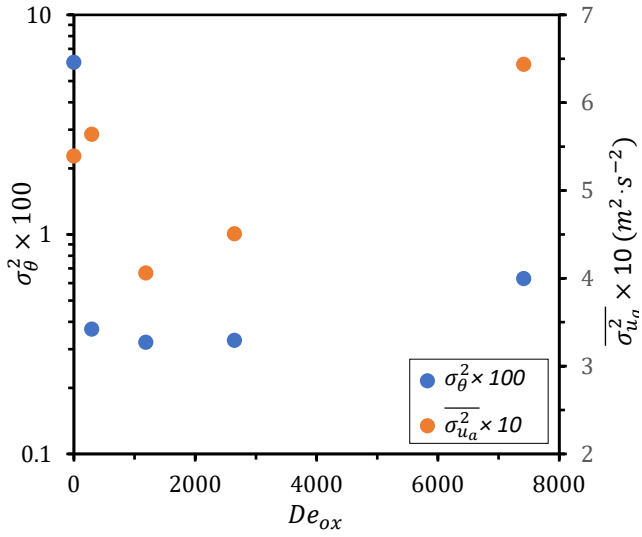

Figure 2-10. Evolution of $\overline{\sigma_{u_a}^2}$ and σ_θ^2 as a function of De_{ox} at $\dot{m} = 60$ g·min^{-1}, $f = 2.46$ Hz, and different amplitudes.

as well as the experimental RTD variance versus De_{ox} at $\dot{m} = 60$ g·min^{-1}, $f = 2.46$ Hz, and different amplitudes. Values of $\overline{\sigma_{u_a}^2}$ quantify axial velocity uniformity over the coil cross-section and, except at the lowest non-zero value of De_{ox}, its change is proportional to the RTD variance. The transverse velocity also contributes to the RTD, such that despite the initial increase in $\overline{\sigma_{u_a}^2}$ with De_{ox}, the RTD variance still drops due to the rapid initial gain in transverse velocity relative to axial velocity (see **Figure 2-13-a**).

Figure 2-11 shows the simulated axial velocity radial profiles time-averaged over an oscillation cycle and normalized by the net velocity ($\bar{u}_a/u_n$) for the operating conditions of

Figure 2-10. For both the horizontal and vertical radial profiles, the axial velocity is visually more uniform at the minimum σ_θ^2 (here $x_o = 23.5$ mm) as quantitatively demonstrated by $\overline{\sigma_{u_a}^2}$. The instantaneous axial velocity horizontal radial profiles are shown for four points in the oscillation cycle for experiments at $\dot{m} = 60$ g·min^{-1} and $f = 2.46$ Hz, and $x_o = 11.75$ and 58.75 mm in **Figure 2-12**. The instantaneous axial velocity profile greatly changes during a cycle such that the time-averaged profile does not fully capture all complexity.

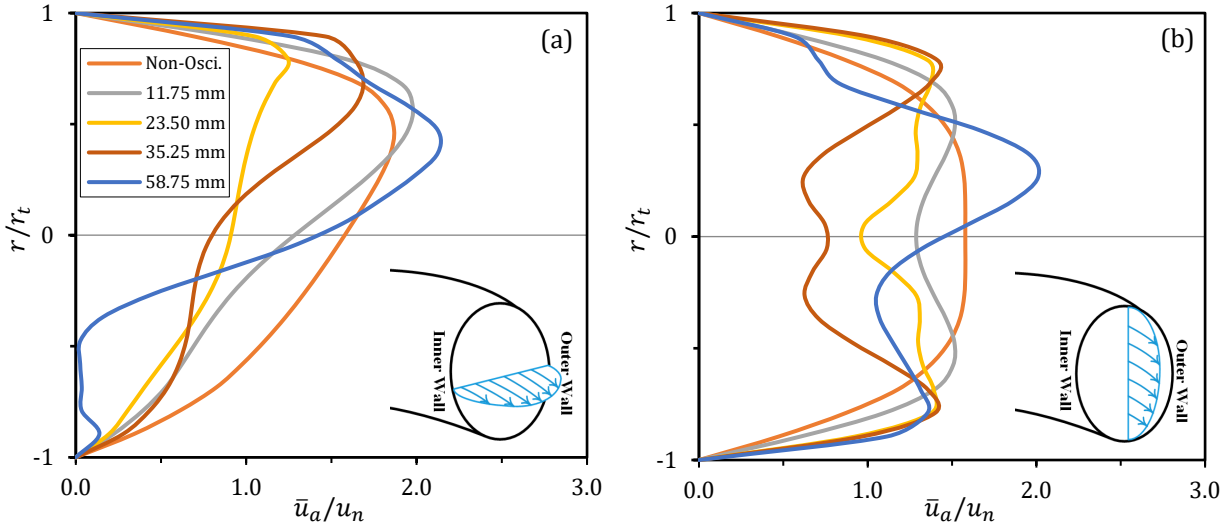

Figure 2-11. Simulated axial velocity radial profile at $\dot{m} = 60$ g·min^{-1}, $f = 2.46$ Hz, and different amplitudes. a. horizontal radial profile b. vertical radial profile. Minimum σ_θ^2 and $\overline{\sigma_{u_a}^2}$ occurs at $x_o = 23.5$ mm.

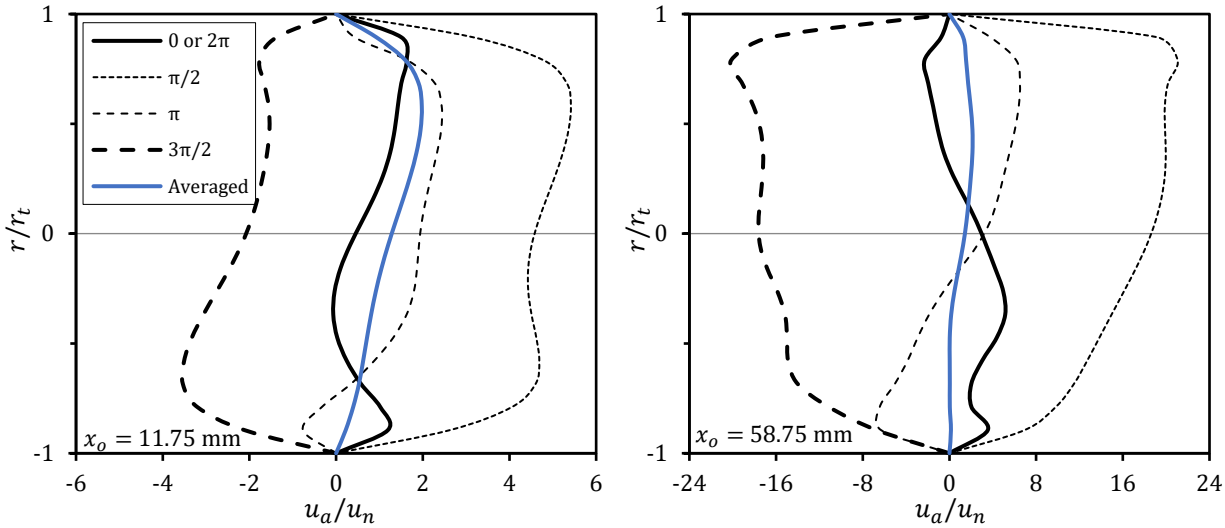

Figure 2-12. Instantaneous and time-averaged axial velocity horizontal radial profiles at $\dot{m} = 60$ g·min^{-1}, $f = 2.46$ Hz, and $x_o = 11.75$ mm and 58.75 mm. Times π/2, π, 3π/2, and 2π are the progressive end of quarters during a full cycle.

The internal boundary layer partition and the simulated 3D flow field support the resulting impact of first narrowing and then broadening the RTD upon oscillating the flow. An increase in oscillation intensity affects the secondary flows where their circulation radius extends further towards the wall. More near-wall fluid is then stirred within the pipe center (i.e., improved radial dispersion) as can be inferred from the time-averaged axial velocity radial profiles in **Figure 2-11**. More of the pipe cross-sectional area possesses a relatively uniform axial velocity leading to a narrower RTD. Further intensification of the oscillation (e.g., by increasing amplitude as in **Figure 2-5** and **Figure 2-6**) will eventually lead to the broadening of the RTD, albeit at a lower rate than the initial narrowing. This can be explained by the relative transverse and axial fluid velocities, where **Figure 2-13** presents the ratio of the time- and area-averaged transverse and axial velocities as well as the experimental RTD variance as a function of De_{ox} at $\dot{m} = 60$ g·min^{-1}, $f = 2.46$ Hz, and different amplitudes. Interestingly, the rate of increase in $\bar{u}_{tr,ave}/\bar{u}_{a,ave}$ with De_{ox} drops past the minimum σ_θ^2, which suggests a reduced relative radial/axial growth rate of the secondary flows from this condition onwards resulting in a broader RTD. Indeed, the size of the vortices that cause radial mixing is limited by the tube wall, [44] whereas there is no such growth limitation in the axial direction.

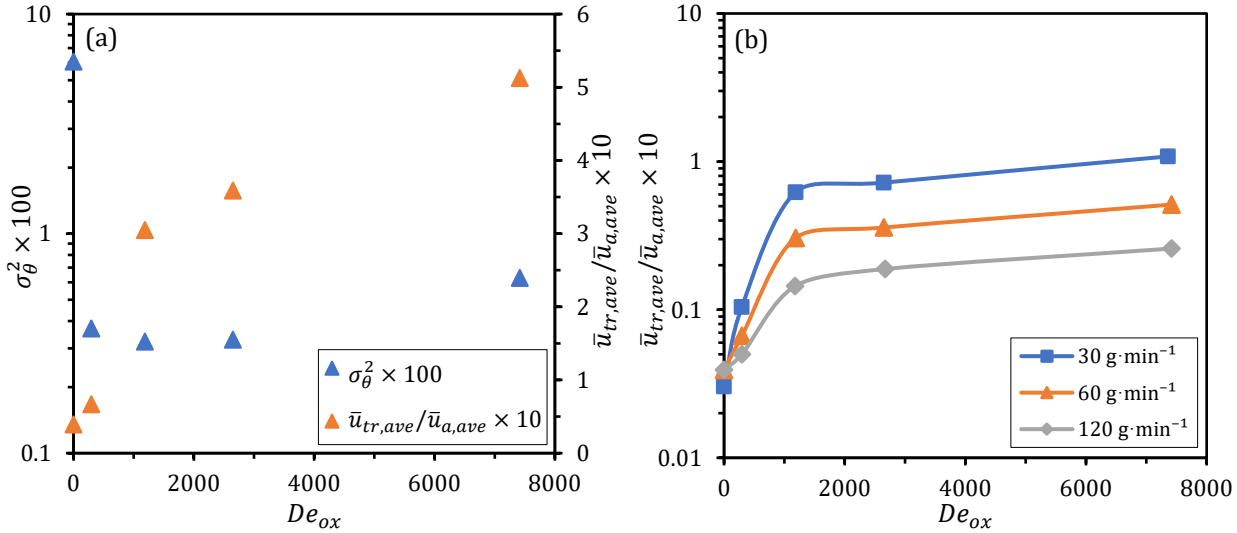

Figure 2-13. For an oscillation frequency of 2.46 Hz and different amplitudes: a. RTD variance and $\bar{u}_{tr,ave}/\bar{u}_{a,ave}$ as a function of De_{ox} at $\dot{m} = 60$ g·min^{-1}, b. Impact of net mass flow rate on $\bar{u}_{tr,ave}/\bar{u}_{a,ave}$ as a function of De_{ox}.

2.3.3. Correlation of RTD model parameters

In analyzing the impact of oscillatory flow conditions on the RTD, the Reynolds number based on the maximum oscillatory velocity and coil diameter (d_t) as characteristic length is often

selected. [25,44,69,71,73–75,77,81] In this study, the RTD variance correlated better using the oscillatory flow amplitude (x_o) as characteristic length in the Reynolds number considering that the flow field is always developing over the cycle. **Figure 2-14** shows the evolution of σ_θ^2 as a function of De_{ox}. At a given frequency and net mass flow rate, a rise in De_{ox} (via a greater amplitude) initially decreases and then increases σ_θ^2. The rate of change in σ_θ^2 is greater before than after the resulting minimum, with the magnitude of the ascending slopes decreasing with increasing net mass flow rate. Moreover, the σ_θ^2 minimum occurs within a relatively small range of De_{ox} (300 to 600) for the range of net mass flow rates.

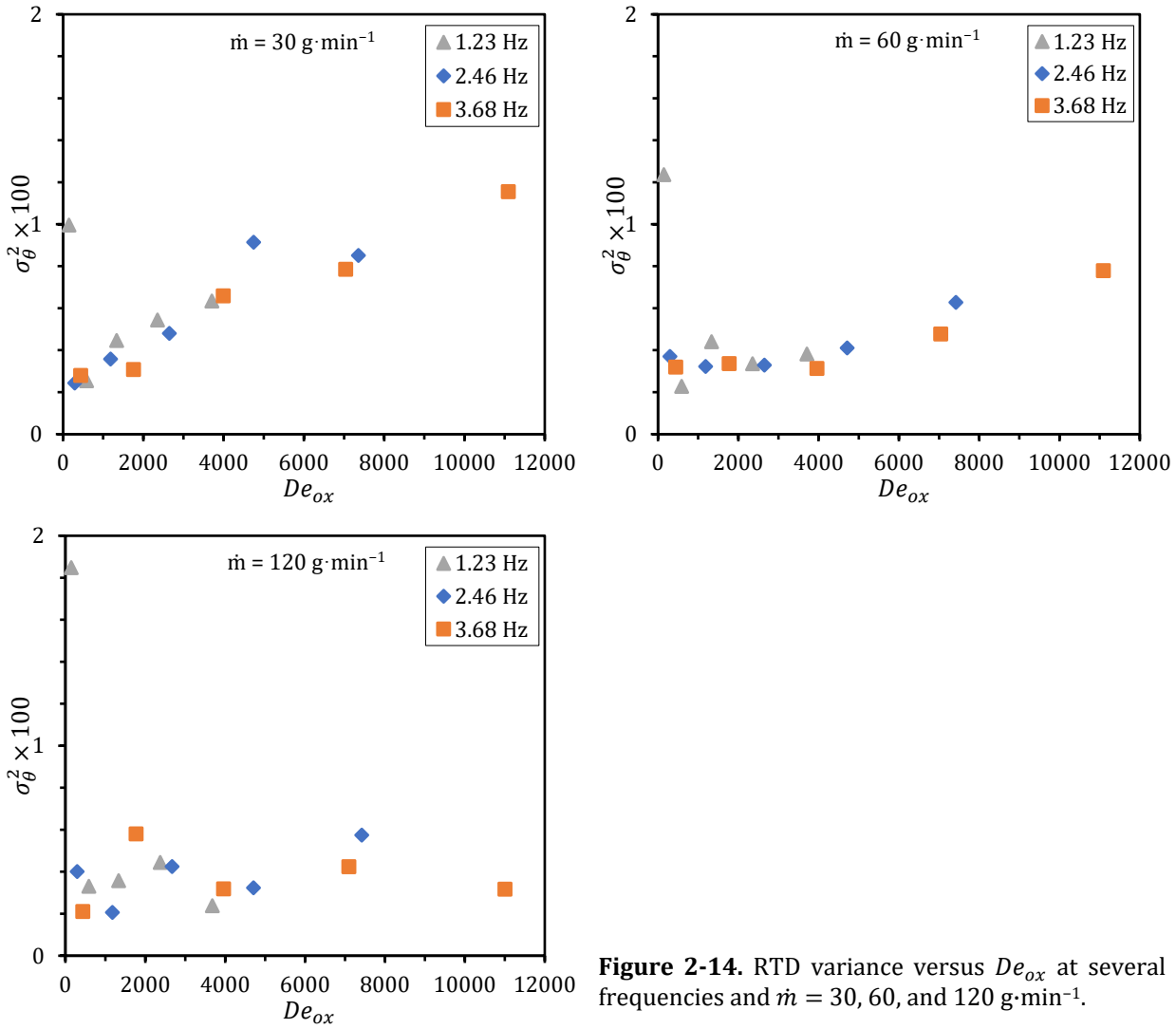

Figure 2-14. RTD variance versus De_{ox} at several frequencies and $\dot{m}$ = 30, 60, and 120 g·min^{-1}.

To provide a more comprehensive correlation for scaling purposes, we included the RTD data obtained by McDonough et al. [44] in coils that are 24 times shorter with a radius of curvature

~15 times smaller, where the flow oscillation frequencies are similar but amplitude and net flow rate are far lower (see **Table 2-3**). For a given operating condition, their calculated number of tanks-in-series was first converted to σ_θ^2 by Equation (2-15): [47]

$$\sigma_\theta^2 = \frac{1}{N} \tag{2-15}$$

Figure 2-15-a compares the two sets of data, with each exhibiting a minimum RTD variance whose location depends on Re_n. Furthermore, the magnitude of σ_θ^2 values obtained in the present study is far less due primarily to a much longer coil. As a result, De_{ox} was normalized by $Re_n^{1.294}$ and σ_θ^2 by $(L/d_t)^{0.578}$ with the power values obtained via best fit with R^2 and F_m (bias factor) values of 0.83 and 1.04, respectively, as presented in **Figure 2-15-b** and Equation (2-16).

$$\sigma_\theta^2 \left(\frac{L}{d_t}\right)^{0.578} = \frac{0.0974}{0.0170 + \Phi} + 0.291\Phi^{0.677} \quad , \quad \Phi = \left(\frac{De_{ox}}{Re_n^{1.294}}\right) \tag{2-16}$$

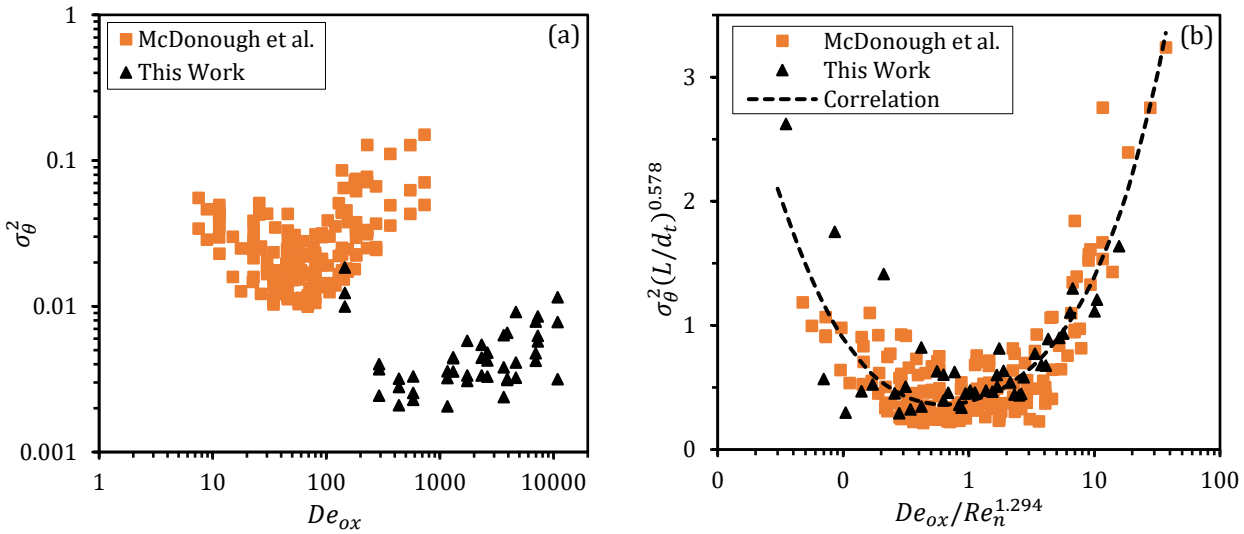

Figure 2-15. RTD variance as a function of De_{ox}. a. Before and b. After data normalization by coil geometry and net mass flow rate.

Now that the RTD variance has been modeled, the parameters of the skewed normal distribution function have the following relationships with σ_θ^2: [84]

$$\sigma_\theta^2 = \omega^2\left(1 - \frac{2\beta^2}{\pi}\right) \tag{2-17}$$

$$\beta^2 = \frac{\alpha^2}{1+\alpha^2} \quad \Leftrightarrow \quad \alpha^2 = \frac{\beta^2}{1-\beta^2} \tag{2-18}$$

$$\theta_m = \xi + \omega\beta\sqrt{\frac{2}{\pi}} \tag{2-19}$$

From **Figure 2-16**, ω^2 has a near linear relationship with σ_θ^2 even if β is a function of α; the correlation is presented in Equation (2-20). This is due to the slope being approximately independent of $\dot{m}$ and that β insignificantly varies for the obtained α values. The values of α can be calculated via Equations (2-17) and (2-18). The value of ξ can be determined by Equation (2-19) considering that $\theta_m = 1$. Based on the correlations provided, the overall algorithm to build an RTD using the coil dimensions and operating conditions is provided in Appendix B.

$$\omega^2 = 2.3014\,\sigma_\theta^2 \qquad 150 < De_{ox} < 11000 \tag{2-20}$$

2.3.4. RTD performance comparison to similar reactors

Table 2-3 compares the coil geometry and operating conditions to similar studies in the literature while **Figure 2-17** compares the geometry-normalized σ_θ^2 as a function of the Dean number ($De = Re_n(d_t/(2R_{c,cor}))^{0.5}$) because there is no De_{ox} for non-oscillatory flow. The selected data are for experiments performed at $f = 2.46$ Hz and $x_o = 23.5$ mm where σ_θ^2 is very close to the minimum σ_θ^2 over the range of De shown in **Figure 2-17**, similarly $f = 4$ Hz and $x_o = 2$ mm for the data of McDonough et al. [44] Non-oscillatory straight coils provide the lowest plug flow performance as they only use one passive energy input via curvature. Adding a few 90° bends (inversions) to a straight coil to make a coil flow inverter (CFI) can improve its plug flow performance to some extent because each bend causes the Dean vortices to rotate, improving the radial mixing by diminishing the effect of the stagnant points at the center of the Dean vortices. [43] Only compact coil flow inverters (CCFI) that have several inversions) provide a plug flow performance comparable to the oscillatory coil reactors. Nonetheless, the plug flow performance of the oscillatory coil reactors is still higher than the one of CCFI at low Dean numbers. Furthermore, for solids-forming reactions, there is often a need for chaotic secondary flows to improve micromixing rates and/or prevent

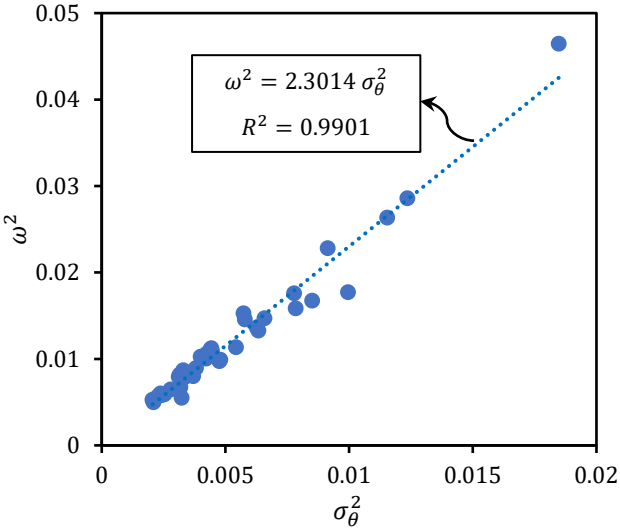

Figure 2-16. Correlation between ω^2 and σ_θ^2 in the skewed normal distribution model.

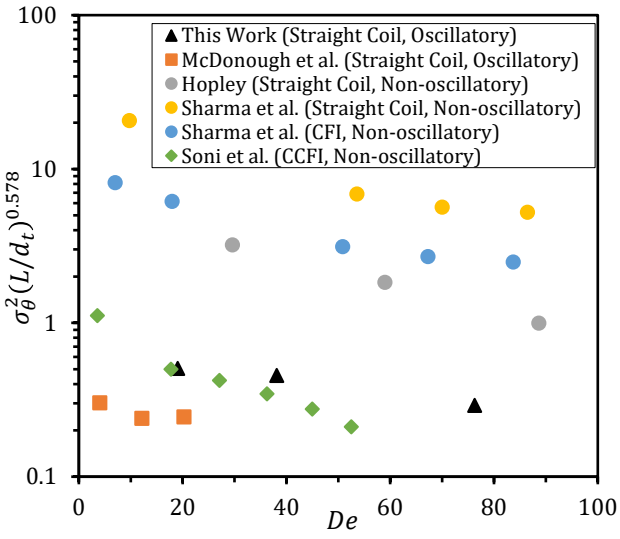

Figure 2-17. [26,44–46][26] Comparison of plug flow performance at $f = 2.46$ Hz, $x_o = 23.5$ mm and different values of De with data obtained by McDonough et al. [44] ($f = 4$ Hz, $x_o = 2$ mm, $d_t =$ 5mm, $R_c = 15$ mm, $P_t = 10$ mm), Hopley [39] ($d_t =$ 3.96 mm, $R_c = 33$ mm, $P_t =$ minimum), Sharma et al. [40] (straight coil: $d_t = 10$ mm, $R_c = 163$ mm, $P_t = 16$ mm, CFI: $d_t = 10$ mm, $R_c = 38$ mm, $P_t = 16$ mm), and Soni et al. [42] ($d_t = 10$ mm, $R_c = 38$ mm, $P_t = 16$ mm).

Table 2-3. Comparison of operating conditions and coil dimensions from this work and references [39,40,42,44]

	Articles	Operating Conditions			Coil Dimensions (mm)				Dimensionless Groups				Geometry
		$\dot{m}$ (g·min^{-1})	f (Hz)	x_o (mm)	d_t	L	R_c	P_t	Re_n	Re_o	De	De_o	De_{ox}	
Oscillatory	This Work	30–120	1.23–3.68	11.75–58.75	4.57	24000	154.2	10	156–627	465–6962	19–76.5	56.5–848	145–10895	Coil
	McDonough et. al. [44]	2.3–7	1–8	1–6	5	1000	15–35	7.5–12.5	10–50	70.5–1128	2.5–20.5	18.5–458	7.5–733	Coil
Non-oscillatory	Hopley et al. [39]	20–100	-	-	3.96	1600	33	Minimum	120–600	-	31–155	-	-	Coil
	Sharma et al. [40]	32–5250	-	-	10	14400	38–163	16	70–11150	-	12–3270	-	-	Coil/CFI
	Soni et al. [42]	5–70	-	-	10	14770–18130	38	16	10–145	-	4–53	-	-	CFI/CCFI

sedimentation and fouling (especially at low Re_n), justifying the use of the extra independent energy input.

2.3.5. Impact of RTD on coil performance for liquid phase 1st and 2nd order reactions

Although our coil geometry and operating conditions lead to low RTD variances (near plug flow pattern), we were interested in quantifying the impact of the non-ideal RTD shape on the reaction conversion of first-order ($r_A = kC_A$) and second-order ($r_A = kC_A^2$) liquid phase reactions along with their two micromixing extremes (completely segregated and micromixed). The conversion (X) of a reaction with a given $F(t)$ and $E(t)$ using the two micromixing models is calculated as follows: [58]

$$X_{seg} = \int_0^\infty X(t)\,E(t)\,dt \tag{2-21}$$

$$\frac{dX_{mm}}{dt} = \frac{r_A}{C_{A0}} + \frac{E(t)}{1-F(t)}X_{mm} \qquad Boundary\ Condition: t \to \infty : X_{mm} = 0 \tag{2-22}$$

For a first-order reaction, the conversion is dependent on only the RTD. For greater reaction orders, conversion in a plug flow reactor is independent of the micromixing model whereas the CSTR highest and lowest conversions are obtained with the segregation and maximum mixedness models, respectively. [58] The equations used to calculate conversion are summarized in **Table 2-4**. The conversions as a function of the first Damköhler number ($Da_1 = k\tau C_{A0}^{m-1}$) are presented in **Figure 2-18.** For the second-order reaction, the maximum mixedness model was used for the CSTR and selected experimental RTDs. The coil performance was ultimately always close to a PFR despite the RTD tailing and skewness since the variance was the most important parameter affecting conversion.

2.4. Conclusion

The fluid macromixing performance of an oscillatory baffleless coil reactor has been investigated via the RTD resulting from a tracer concentration step change at the reactor entrance. All RTDs were fitted to the skewed normal distribution function, which is a three-parameter statistical model. The reactor flow pattern was found to be near plug flow at all oscillation conditions, although deviations from ideality such as skewness and tailing were

observed. The RTD variance also exhibited descending and ascending trends at different oscillation conditions leading to a minimum at relatively low oscillation intensity. Superimposing a small amount of oscillation to the net flow therefore helps the flow pattern further approach ideal plug flow. Operating conditions were lumped into a new Dean number that uses the oscillation amplitude as the characteristic length. The RTD variance was minimized over a short range of this oscillatory Dean number (300 to 600) and was effectively independent of oscillation frequency.

The flow pattern performance was compared to recent mixing studies in coil reactors with different geometric dimensions and oscillatory conditions. A generalized correlation was ultimately developed using the new oscillatory Dean number and normalizing the data. Comparison to passive coil flow inverter reactors showed that they can also provide near plug flow. However, the advantage of an independent energy input via active mixing becomes valuable when considering power dissipation control for micromixing and particle sedimentation and wall fouling. Finally, the performance of the reactor for first- and second-order liquid reactions was evaluated by determining chemical conversion at different Damköhler numbers using the segregation and maximum mixedness micromixing models fed with selected RTDs. This analysis demonstrated that the coil reactor conversion is still consistent with that of an ideal plug flow pattern despite the observed skewness and tailing.

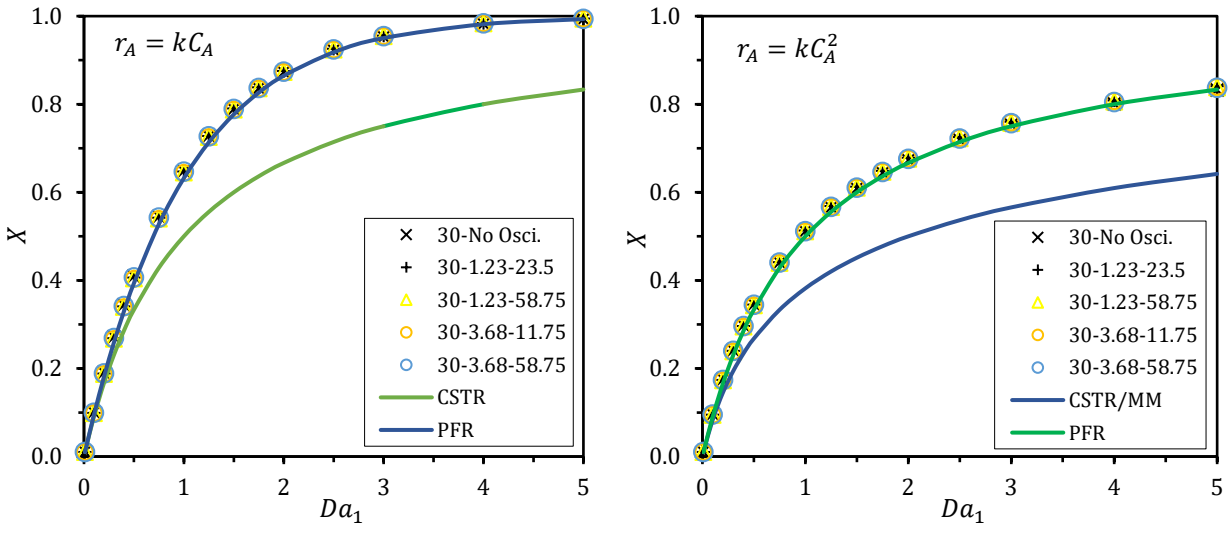

Figure 2-18. Conversion as a function of the first Damköhler number. a. first-order reaction and b. second-order reaction. For the second-order reaction, the maximum mixedness model was used for the CSTR and selected experimental RTDs. The first, second, and third numbers in the legend refer to $\dot{m}$ (g·min^{-1}), f (Hz), and x_o (mm), respectively.

Table 2-4. Reactor flow models using the segregation and maximum mixedness micromixing models.

Kinetics		RTD		Conversion
First-order: $r_A = kC_{A0}(1-X)$ $X(t) = 1 - e^{-kt}$ $Da_1 = k\tau$	PFR:	$F(t) = \begin{cases} 0 & t < \tau \\ 1 & t \geq \tau \end{cases}$	$E(t) = \delta(t-\tau)$	$X_{seg} = X_{mm} = 1 - e^{-Da_1}$
	CSTR:	$F(t) = 1 - e^{-\frac{t}{\tau}}$	$E(t) = \frac{e^{-\frac{t}{\tau}}}{\tau}$	$X_{seg} = X_{mm} = \frac{Da_1}{1+Da_1}$
Second-order: $r_A = kC_{A0}^2(1-X)^2$ $X(t) = \frac{kC_{A0}t}{1+kC_{A0}t}$ $Da_1 = k\tau C_{A0}$	PFR:	Same as above		$X_{seg} = X_{mm} = \frac{Da_1}{1+Da_1}$
	CSTR:	Same as above		$X_{seg} = \int_0^\infty \frac{kC_{A0}t}{1+kC_{A0}t}\left(\frac{e^{-\frac{t}{\tau}}}{\tau}\right)dt$ * $\frac{dX_{mm}}{d\theta} = -Da_1 + (1+2Da_1)X_{mm} - Da_1X_{mm}^2$ **

*No analytical solution exists for this equation.

** This equation is a form of the Riccati differential equation which has an analytical solution, but its integral constant(s) cannot be obtained using the boundary condition of the maximum mixedness model.

Nomenclature

Latin Letters

C_A	mol·L^{-1}	concentration of reactant A
C_{A0}	mol·L^{-1}	initial concentration of reactant A
d_t	mm	inner tube diameter
D	m^2·s^{-1}	axial dispersion coefficient
Da_1	-	first Damköhler number $= k\tau C_A^{m-1}$
De	-	Dean number $= Re_n\sqrt{r_t/R_c}$
De_o	-	oscillatory Dean number based on coil tube diameter $= Re_o\sqrt{r_t/R_c}$
De_{ox}	-	oscillatory Dean number based on oscillation amplitude $= Re_{ox}\sqrt{r_t/R_c}$
E	-	exit time distribution function (RTD)
E_μ	W	viscous power
E_{ME}	W	mechanical power
f	Hz	oscillation frequency
F	-	cumulative residence time distribution
F_m	-	bias factor $= exp\left[\frac{1}{n}\sum_{i=1}^{n} ln\left(\frac{Y_{correlation}}{Y_{experimental}}\right)\right]$
L	m	tube length
M	-	reaction order
$\dot{m}$	g·min^{-1}	net mass flow rate
n	-	number of data points
p'	m^2·s^{-2}	modified pressure
P	Pa	Pressure
Pe	-	Peclet number $= uL/D$
Pe_f	-	forward Peclet number
Pe_b	-	backward Peclet number
P_t	mm	coil tube pitch
Q	m^3·min^{-1}	volumetric flow rate
r_t	mm	inner tube radius
R	mm	radial distance
R^2	-	coefficient of determination
R_c	mm	coil radius of curvature
Re_n	-	net flow Reynolds number $= u_n\,\rho d_t/\mu$
Re_o	-	oscillatory Reynolds number based on coil tube diameter $= 2\pi f x_o \rho d_t/\mu$
Re_{ox}	-	oscillatory Reynolds number based on oscillation amplitude $= 2\pi f \rho x_o^2/\mu$
t	s	time
$\bar{t}$	s	mean residence time
t_{min}	s	start time of conductivity change
t_{max}	s	end time of conductivity change
T	-	Owen's T function
u_a	m·s^{-1}	axial velocity
$\bar{u}_a$	m·s^{-1}	axial velocity time-averaged over full oscillation cycle

$\bar{u}_{a,ave}$	m·s^{-1}	axial velocity area- and time-averaged over full oscillation cycle
$u_{b,max}$	m·s^{-1}	maximum backward velocity
$u_{f,max}$	m·s^{-1}	maximum forward velocity
u_{in}	m·s^{-1}	instantaneous velocity
u_n	m·s^{-1}	net flow superficial velocity
$\bar{u}_{tr,ave}$	m·s^{-1}	transverse (radial and angular) velocity that is area- and time-averaged over full oscillation cycle
U	m·s^{-1}	velocity vector
V	m^3	reactor volume
x_o	mm	oscillation amplitude
X	-	conversion
X_{mm}	-	conversion for maximum mixedness model
X_{seg}	-	conversion for segregation model
Z	-	coil axial direction

Greek Letters

α	-	shape factor in skewed normal distribution model
δ	-	Dirac delta function
ε_{ME}	W·kg^{-1}	mass mechanical power dissipation
ε_{μ}	W·kg^{-1}	mass viscous power dissipation
θ	-	dimensionless time
θ_m	-	RTD dimensionless mean time
θ_{min}	-	dimensionless t_{min}
θ_{max}	-	dimensionless t_{max}
μ	Pa·s	fluid dynamic viscosity
ν	m^2·s^{-1}	fluid kinematic viscosity
ξ	-	location parameter in skewed normal distribution model
ρ	kg·m^{-3}	fluid density
$\overline{\sigma_{u_a}^2}$	m^2·s^{-2}	time-averaged variance of axial velocity profile
σ_θ^2	-	RTD dimensionless variance
τ	s	space time $= V/Q$
ω	-	kurtosis in skewed normal distribution model

Abbreviations

CCFI	compact coil flow inverter
CFI	coil flow inverter
CSTR	continuous-flow stirred tank reactor
erf	error function
MFC	mass flow controller
PFR	plug flow reactor
RTD	residence time distribution
SSR	sum of squared residuals
VLV	valve

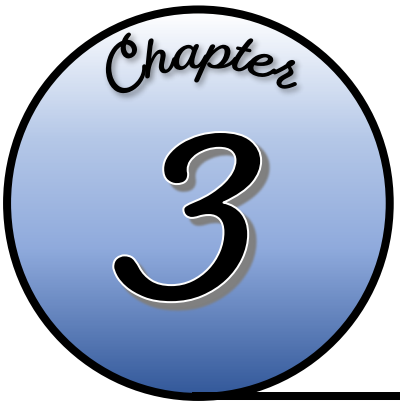

Power Dissipation and Phase Shift

3.1. Introduction

Continuous processing is ubiquitous in bulk chemicals manufacturing due to its inherent economies of scale and ease of automation. Conversely, fine chemicals and pharmaceuticals processing is traditionally batchwise to simplify product quality verification and enable equipment repurposing for diverse production campaigns. However, batch processing involving very fast and/or high energy reactions requires significant dilution to mitigate safety concerns, which leads to substantial quantities of waste and oversized equipment. Consequently, there is an impetus to incorporate intensified continuous-flow process equipment within these operations to allow safer operation at more intense conditions. In particular, intensified continuous-flow reactors with small length scales are commonly studied, and they have been commercialized for some applications because they can greatly increase mixing and energy transfer rates.

Oscillatory and pulsatile flows are commonly applied to intensify mixing and heat transfer in various tubular reactors. For example, mixing enhancement in oscillatory baffled reactors with various constrictions has been numerically and experimentally investigated in many studies. [88,90,92–97] Additionally, some studies have investigated heat transfer enhancement in coiled tubes. [98–100] Furthermore, oscillatory flow has been used in coiled tube reactors to enhance liquid-liquid mixing, [45] prevent fouling when used with solids-forming reactions, [20] and improve plug flow performance. [20,44,101]

In the present work, numerical simulations were used to investigate fluid dynamics and power dissipation in a baffleless coiled tube reactor operating under oscillatory flow conditions. Flow conditions were varied over a broad range, and the coiled tube geometry matched a configuration that was previously used in an experimental study. [101] The results provide new insight into the fluid dynamics and mixing occurring within coiled tube reactors under oscillatory flow conditions. Additionally, local and averaged velocity data and power dissipation predictions explain the observed trends in the variance of the residence time distribution. Furthermore, a new simplified calculation method provides a convenient way to estimate power dissipation and phase shift of the pressure drop for oscillatory flow in coiled tubes, which can be correlated with mixing times and transport rates in the future.

3.2. Methodology

3.2.1. Experimental Data

Residence time distributions (RTDs) measured for a wide range of oscillation intensities in a Hastelloy coil having an internal diameter D_t of 4.57 mm, a radius of curvature R_C of 151 mm, a length L of 24 m, and a tube pitch of 10 mm were reported in a previous study. [101] A minimum was observed in the variance of the RTD, σ_θ^2, for different oscillatory conditions at each net flow rate. Although the RTDs showed some asymmetry, reactor performance was close to plug flow for all experiments. As described in the previous study, the average relative standard deviation of the measured RTD variance is approximately 5 %.

3.2.2. Operating Conditions

The instantaneous cross-sectionally averaged axial velocity $\overline{\mathrm{U}}$ is given by the following expression:

$$\overline{\mathrm{U}} = \overline{\overline{\mathrm{U}}} + \mathrm{U}_o = \overline{\overline{\mathrm{U}}} + 2\pi f x_o \sin(2\pi f t) \tag{3-1}$$

where $\overline{\overline{\mathrm{U}}}$ is the axial velocity based on the net flow rate (cross-sectionally and time-averaged velocity), U_o is the oscillatory flow velocity, f is the oscillation frequency, and x_o is the oscillation amplitude. The net flow and oscillatory flow Reynolds numbers are defined based on the oscillatory and net flow velocities as follows:

$$Re_n = \frac{\overline{\overline{\mathrm{U}}} D_t}{\nu} \tag{3-2}$$

$$Re_o = \frac{\mathrm{U}_o D_t}{\nu} \tag{3-3}$$

where D_t is the tube inside diameter, and ν is the kinematic viscosity. For consistency with the previous experimental work, a kinematic viscosity of 8.926×10^{-7} $m^2 \cdot s^{-1}$ and a density of 997 $kg \cdot m^{-3}$ were used in the present simulation study. Net flow rates of 30, 60, and 120 $g \cdot min^{-1}$ were used, which are equivalent to net flow Reynolds numbers of 157, 313, and 626. **Table 3-1** summarizes the oscillation conditions that were investigated in the previous experimental work, which yield equivalent oscillatory flow Reynolds numbers of 464–6955.

However, it is important to note that only the conditions highlighted in green were simulated using CFD. These conditions were studied for each net flow rate.

Table 3-1. Oscillation conditions considered for all net flow rates (cases highlighted in green were used in CFD simulations).

f (Hz)	x_o (mm)				
1.23	11.75	23.5	35.25	47.00	58.75
2.46	11.75	23.5	35.25	47.00	58.75
3.68	11.75	23.5	35.25	47.00	58.75

3.2.3. Computational Fluid Dynamics (CFD)

3.2.3.1. Geometry and mesh

The simulated geometry is based on the coil used in the previous experimental investigation. However, considering that end effects are expected to be negligible due to the very high length-to-diameter ratio of the coil, only three turns of the total coil length were simulated. As shown in **Figure 3-1**, volumetric data were processed for the sixth quarter turn from the inlet and cross-sectional data were processed halfway through the coil to eliminate the impact of the boundary conditions on the results. The results for the sixth quarter turn and middle cross-section were confirmed to be independent of end effects caused by the boundary conditions by analyzing both the instantaneous pressure drop and velocity profiles over the oscillation cycle as well as the time-averaged pressure drop and velocity profiles for successive quarter turns. In all cases, the velocity profile took no more than one half turn to

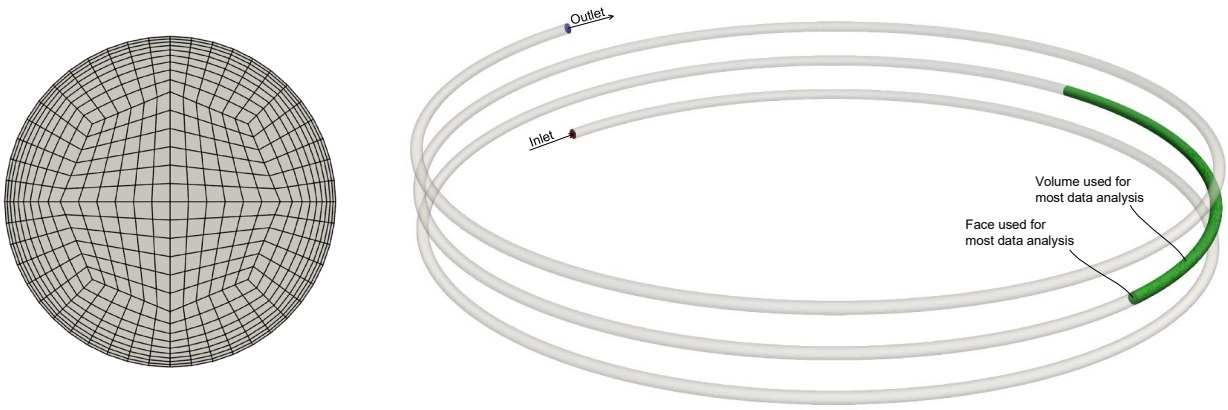

Figure 3-1. Cross-section of the mesh used in simulations other than the mesh dependence studies (left), and diagram showing the coil and volume and face regions for which most post-processing was performed (right).

develop, which is reasonable considering that the length-to-diameter ratio for a single turn of the coil was approximately 210.

The computational mesh consisted of a modified O-grid that was extruded in the axial direction with a uniform distribution. The mesh was graded towards the wall to ensure adequate resolution of the axial and secondary flow boundary layers. An image of the cross-section of the mesh that was used in the simulations is shown in **Figure 3-1**. This mesh was used in all simulations other than the mesh dependence studies and has 829 440 cells.

3.2.3.2. Governing equations

Transient incompressible flow was simulated using the *pimpleFoam* solver available in OpenFOAM v9. [86] This solver uses a combination of the pressure-implicit with splitting of operators (PISO) and semi-implicit-method-for-pressure-linked-equations (SIMPLE) algorithms to iteratively solve for the pressure and velocity fields at each time step. The solver was customized to print additional field information for the computation of power dissipation and phase shift. Neglecting gravity forces, the continuity and momentum equations for transient laminar incompressible flow can be written as follows:

$$\nabla \cdot \mathbf{U} = 0 \tag{3-4}$$

$$\frac{\partial \mathbf{U}}{\partial t} + \mathbf{U} \cdot \nabla \mathbf{U} = -\nabla p' + \nabla \cdot \nu [\nabla \mathbf{U} + (\nabla \mathbf{U})^T] \tag{3-5}$$

where $\mathbf{U}$ is the velocity vector, ν is the kinematic viscosity, and the modified pressure $p' = p/\rho$ is the pressure p normalized by density ρ.

Laminar flow is known to persist in straight tubes for Reynolds numbers up to approximately 2300. The transition to turbulence in coiled tubes is known to normally occur at higher Reynolds numbers than in straight tubes because the curvature stabilizes the flow and thereby delays the onset of turbulence. The correlation of Ito [102] gives a critical Reynolds number greater than approximately 5200 for the coil used in the present study. Although it may seem logical that oscillatory flow should destabilize the velocity field and lead to an earlier transition to turbulence, there is insufficient information in the published literature to draw this conclusion. Furthermore, flow oscillation leads to a constantly developing

velocity profile, and it is known that developing flows which are not innately turbulent require a minimum distance to transition to turbulence. Therefore, conditions up to $Re_n + Re_o \approx 5275$ were simulated without the use of a turbulence closure model. A summary of the oscillation conditions used in the simulations is provided in **Table 3-1**. The case having the highest combined Reynolds number that was simulated has the highest net flow rate of 120 g·min^{-1} with x_o = 58.75 mm and f = 2.46 Hz. The cases with x_o = 58.75 mm and f = 3.68 Hz were not simulated because $Re_n + Re_o > 7000$ was judged too high for applicability of the laminar model assumption without further validation and/or significantly higher mesh resolution.

3.2.3.3. Numerical methods

The flow boundary conditions must accommodate forward and backward flow during the oscillation cycle and minimize end effects. Therefore, following the approach used by Jimeno et al. [88] for a different geometry, the inlet velocity was specified assuming instantaneously fully-developed laminar flow in a straight tube:

$$\mathrm{U}_{in} = 2\left(\overline{\overline{\mathrm{U}}} + 2\pi f x_o \sin(2\pi f t)\right)\left(1 - 4\frac{r^2}{D_t^2}\right) \tag{3-6}$$

where U_{in} is the axial inlet velocity, and r is the radial coordinate referenced to the centre of the inlet boundary. This boundary condition was applied to the side labelled as inlet in **Figure 3-1** when the flow was forward during the oscillation cycle, and a fixed pressure condition was used at the side labelled as outlet. Conversely, when the flow was backward, this condition was applied to the side labelled as outlet, and a fixed pressure condition was used at the side labelled as inlet.

Transient simulations were performed, and sufficient pressure-velocity coupling iterations were used within each time step to converge the scaled residuals to a tolerance of 10^{-4}. Temporal accuracy was realized by restricting the time step to a maximum Courant number of 0.5 and using the second-order accurate Crank-Nicolson scheme. Second-order accurate schemes were used for discretization of all spatial terms. These specifications are consistent with current best practices for accurate simulation of transient flows.

The simulations reached pseudo-steady state within two oscillation cycles. Nonetheless, all simulations were performed for at least six oscillation cycles, and the data were time-averaged over the last two cycles.

3.2.3.4. Data processing

Following Plawsky [89] and neglecting gravity, the mechanical energy conservation equation can be written as follows:

$$\underbrace{\int_V \frac{\partial}{\partial t}\left(\frac{1}{2}\rho\mathbf{U^2}\right)\,dV + \int_V \left(\nabla\cdot\left(\frac{1}{2}\rho\mathbf{U^2}\right)\mathbf{U}\right)\,dV + \int_V \nabla\cdot(p\mathbf{U})\,dV + \int_V \nabla\cdot[\boldsymbol{\tau}\cdot\mathbf{U}]\,dV}_{E_{ME}} = \underbrace{\int_V (\boldsymbol{\tau}\colon\nabla\mathbf{U})\,dV}_{E_\mu} \quad (3\text{-}7)$$

where the stress tensor $\boldsymbol{\tau} = \nu[\nabla\mathbf{U} + (\nabla\mathbf{U})^T]$, E_{ME} is the mechanical power, E_μ is the viscous power, and V is the control volume being assessed.

Avila et al. [90] noted that the third term on the left-hand side of Equation (3-7)was dominant for an oscillatory baffled reactor (OBR). Avila et al. [90] also stated that the third term on the left-hand side of Equation (3-7), which is based on the pressure drop, is much less sensitive to the mesh resolution than the viscous dissipation on the right-hand side. Therefore, the difference between these terms is used as one mesh dependence metric in Section 3.3.1 of the present work.

The first term on the left-hand side of Equation (3-7) is equal to zero when averaged over an oscillation cycle. Therefore, for comparison and to judge mesh dependence, the time-averaged power dissipation was estimated using three approaches. Method 1 was to time and volume average the left-hand side of Equation (3-7) over the last two oscillation cycles:

$$\bar{\varepsilon}_{ME} = -\left[\frac{\int_{t_1}^{t_2}\left[\int_V \left(\nabla\cdot\left(\frac{1}{2}\rho\mathbf{U^2}\right)\mathbf{U}\right)\,dV\right]\,dt}{\rho V(t_2-t_1)} + \frac{\int_{t_1}^{t_2}\left[\int_V \nabla\cdot(p\mathbf{U})\,dV +\right]\,dt}{\rho V(t_2-t_1)} + \frac{\int_{t_1}^{t_2}\left[\int_V \nabla\cdot[\boldsymbol{\tau}\cdot\mathbf{U}]\,dV\right]\,dt}{\rho V(t_2-t_1)}\right] \quad (3\text{-}8)$$

where $t_2 - t_1$ is the time-averaging period, which was specified to be two complete cycles.

Method 2 computes the power dissipation by time and volume averaging the right-hand side of Equation (3-7) over the last two oscillation cycles:

$$\bar{\varepsilon}_{\mu} = -\frac{\int_{t_1}^{t_2}\left[\int_V (\boldsymbol{\tau}:\nabla\mathbf{U})\,dV\right]dt}{\rho V(t_2-t_1)} \tag{3-9}$$

Method 3 estimates the power dissipation by time averaging the pressure gradient:

$$\bar{\varepsilon}_{p} = -\frac{\int_{t_1}^{t_2}\overline{\mathrm{U}}\frac{\Delta p}{L}\,dt}{\rho(t_2-t_1)} \tag{3-10}$$

where $-\frac{\Delta p}{L}$ is the pressure drop per unit length. This is equivalent to applying the divergence theorem to the third term on the left-hand side of Equation (3-7). The phase shift was determined by fitting the pressure gradient data to a sine function:

$$\frac{\Delta p}{L} = A\sin(2\pi f t+\phi)+B \tag{3-11}$$

where ϕ is the phase shift.

3.2.4. Simplified Calculation Method (Macroscopic Mechanical Energy Balance)

Assuming incompressible flow, neglecting gravity, recognizing that the tube cross-section remains constant, neglecting viscous work, and recognizing that there are no external power inputs within the control volume, the macroscopic mechanical energy balance equation for the coil can be written as follows: [89]

$$-\frac{1}{2}\rho A_C L\frac{d}{dt}(\overline{\mathrm{U}}^2) = A_C\overline{\mathrm{U}}\Delta p - E_{\mu} \tag{3-12}$$

where A_C is the tube cross-sectional area. If Equation (3-12) is time-averaged over an integer number of oscillation cycles, the term on the left-hand side will be zero, and Equation (3-10) can be recovered. The equation for the instantaneous cross-sectionally averaged velocity $\overline{\mathrm{U}} = \overline{\overline{\mathrm{U}}} + 2\pi f x_o\sin(2\pi f t)$ can be differentiated in time and substituted into Equation (3-12). The

resulting expression can be divided by $A_C L\overline{\mathrm{U}}$ and rearranged to yield an explicit equation for the instantaneous pressure drop per unit length:

$$-\frac{\Delta p}{L} = \rho(2\pi f)^2 x_o \cos(2\pi f t) - \frac{E_\mu}{A_C L\overline{\mathrm{U}}} = \rho(2\pi f)^2 x_o \cos(2\pi f t) + F_{loss} \tag{3-13}$$

where F_{loss} are frictional losses. The frictional losses term in Equation (3-13) is normally written in terms of the instantaneous kinetic energy and Fanning friction factor, $f_{fanning}$:

$$-\frac{\Delta p}{L} = \rho(2\pi f)^2 x_o \cos(2\pi f t) + 2 f_{fanning} \frac{\rho}{D_t} \overline{\mathrm{U}}^2 \tag{3-14}$$

Unfortunately, friction factor correlations are only available for steady flows in coiled tubes. Therefore, it was expected that this method would only provide an approximate rather than a precise estimate of the power dissipation or phase shift and thus selection of the friction factor model was not critical. Consequently, the relatively simple steady-state friction factor correlation of Van Dyke [103] was selected under the assumption that it could be applied instantaneously at any time in the oscillation cycle.

$$f_{fanning} = \frac{16}{Re_t} \max\left(1, 0.47136\, {De_t}^{1/4}\right) \tag{3-15}$$

where Re_t was calculated as $Re_n + Re_o$, and De_t was calculated as $De_n + De_o = (Re_n + Re_o)(D_t/2R_c)^{0.5}$. Although many other friction factor correlations exist for coiled tubes, only one correlation was tested because other relationships are anticipated to yield similar trends.

The procedure to estimate power dissipation and phase shift is to first obtain the instantaneous pressure drop per unit length by using Equation (3-15) in combination with Equation (3-14). The power dissipation is then estimated by using the pressure drop per unit length in Equation (3-10). Similar to the treatment of the CFD data, the phase shift is determined by fitting the pressure gradient data to a sine function as shown in Equation (11).

3.3. Results and Discussion

3.3.1. Mesh dependence

Mesh dependence was assessed for the case with the highest Re_t of approximately 5275: x_o = 58.75 mm, and f = 2.46 Hz. Four mesh resolutions were used in the mesh resolution study: M1 = 245 760, M2 = 829 440, M3 = 2 877 120, and M4 = 9 797 760 mesh cells. As noted in Section 3.2.3.4, Equation (3-8), Equation (3-9), and Equation (3-10) can be used to estimate the power dissipation. However, it is known that pressure estimates, which are the basis of Equation (3-8) and Equation (3-10), are much less sensitive to the mesh resolution than velocity gradient estimates, which are the basis of Equation (3-9). Therefore, since Equation (3-9) includes the local velocity gradients in calculation of the power dissipation, convergence of the power dissipation estimate from Equation (3-9) towards the values estimated using Equation (3-8) or Equation (3-10) is one rigorous criterion that can be used to judge mesh convergence.

Power dissipation predictions from Equation (3-8) or Equation (3-10) were within 2 % for most cases and were within 1 % for the case with $Re_t = 5275$. Therefore, only the CFD results from Equation (3-8) and Equation (3-9) are compared in this section. **Figure 3-2** shows the power dissipation predictions for the four mesh resolutions. The mechanical power dissipation estimate (Equation (3-8)) changes minimally for the three highest mesh resolutions, whereas the viscous power dissipation (Equation (3-8)) converges at a significantly slower rate. It is impractical to always use a mesh that fully resolves the viscous power dissipation. Hence, M2 was selected for all case studies because the mechanical power dissipation estimate is very close to the predictions from the two finer meshes and the relative difference of the viscous power dissipation estimate is well below 10 %. It is also important to remember that the mesh dependence study was performed for the highest Re_t, and consequently these differences are lower for other cases.

Convergence of the viscous power dissipation is only one mesh dependence metric. Although this parameter includes velocity in its calculation, it is logical to also consider changes in the velocity profiles with mesh resolution directly. Thus, time-averaged and instantaneous axial velocity profiles are provided for two cut lines on the middle cross-section of the coil in **Figure 3-3** and **Figure 3-4**. Although there are clearly some differences in the predicted

velocity profiles, M2 was selected as a compromise between computational resources and accuracy.

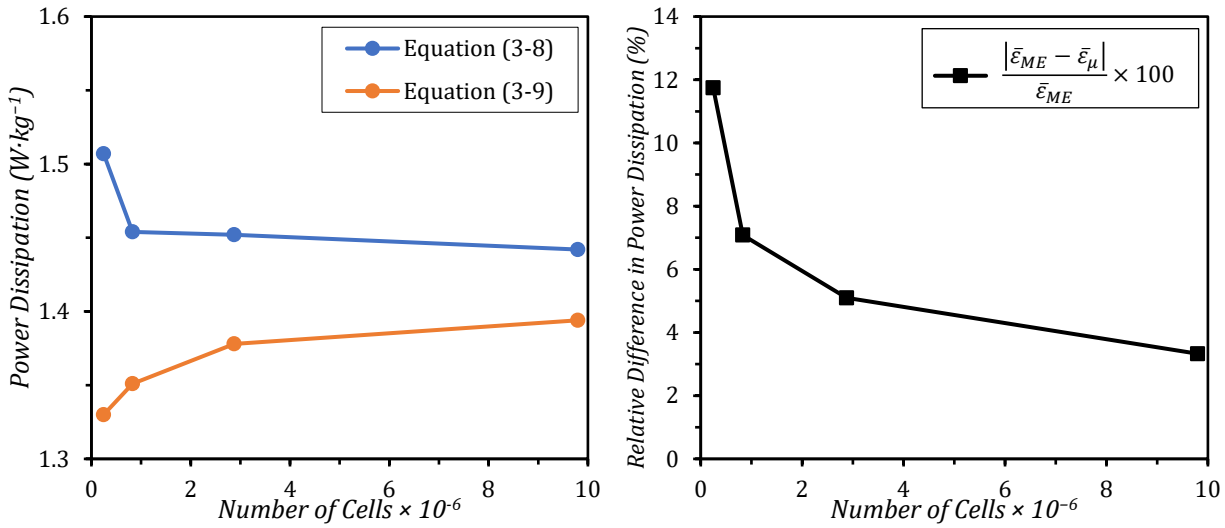

Figure 3-2. Power dissipation estimated using Equation (3-8) and Equation (3-9) for four mesh resolutions (left), and relative difference between predictions (right). Simulated case has $Re_t = 5275$, $Re_n = 626$, $x_o = 58.75$ mm, and $f = 2.46$ Hz.

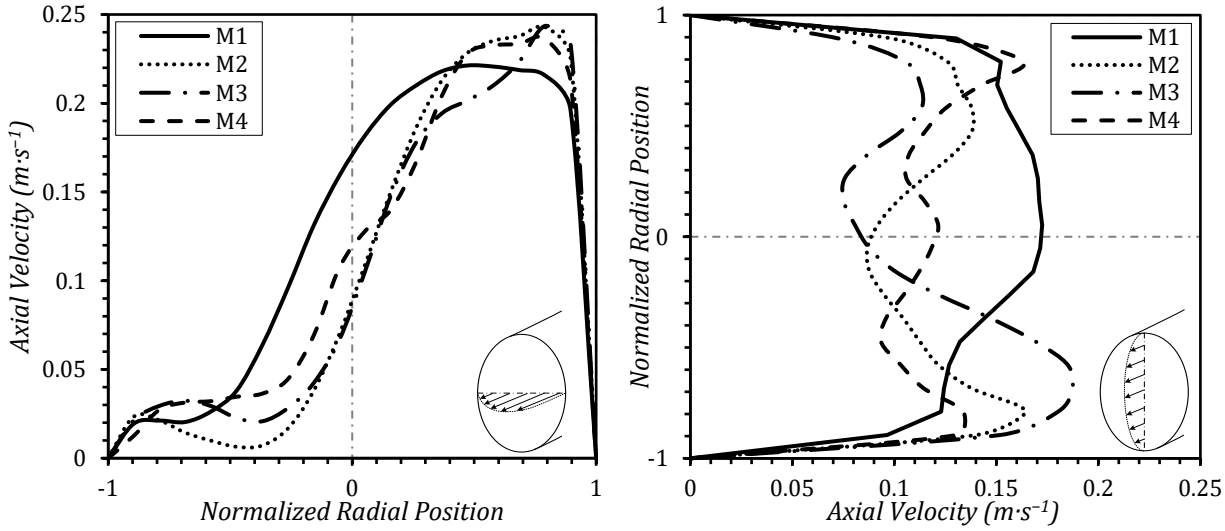

Figure 3-3. Time-averaged axial velocity profiles at the middle cross-section for the four mesh resolutions. Simulated case has $Re_t = 5275$, $Re_n = 626$, $x_o = 58.75$ mm, and $f = 2.46$ Hz.

3.3.2. Residence time distribution

In the previous experimental work, the variance of the RTD was correlated with several dimensionless parameters. One goal of the present study is to provide an analysis of the observed RTD variance in terms of the time-averaged power dissipation and other key flow

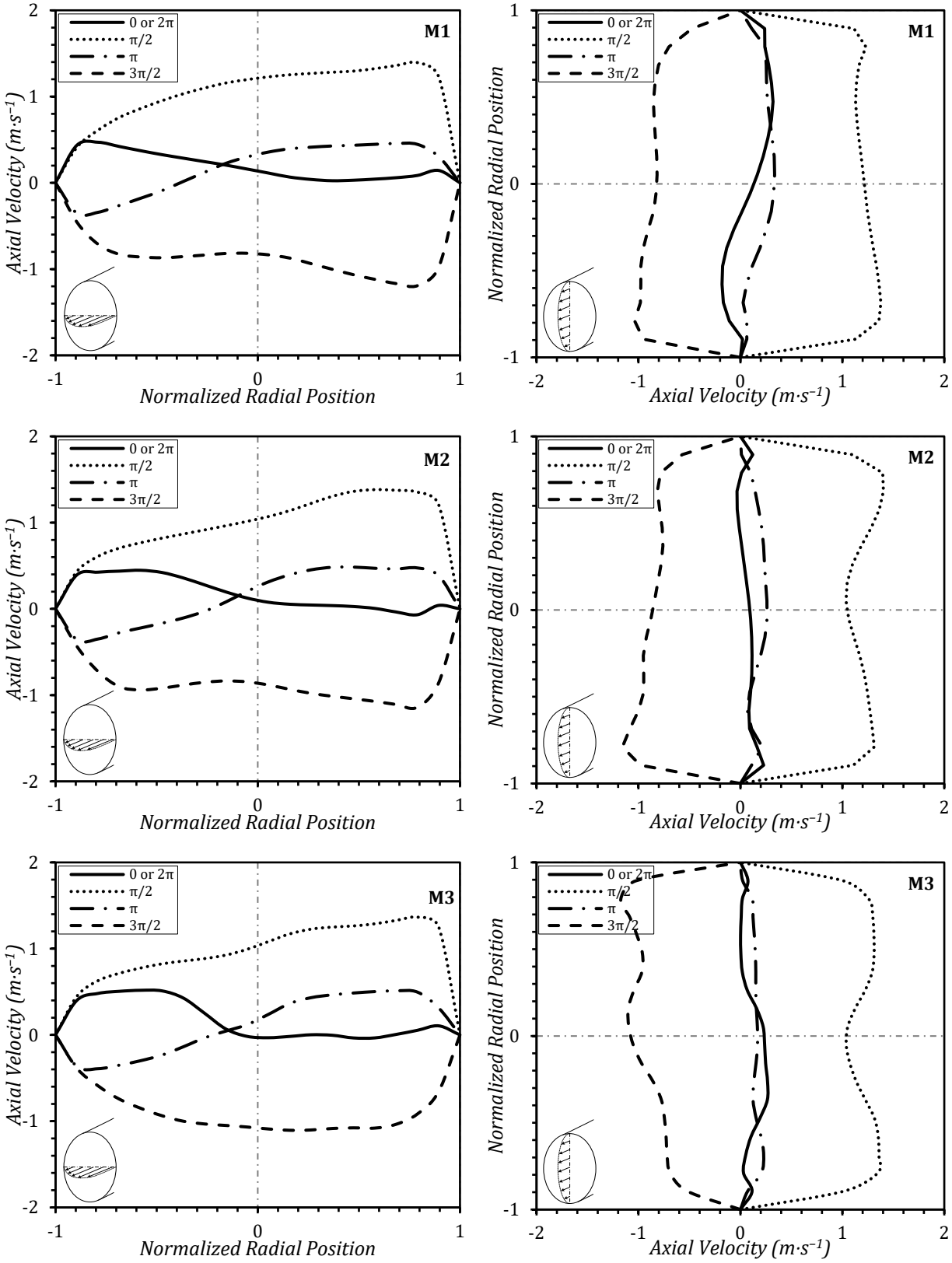

Figure 3-4. Instantaneous axial velocity profiles at the middle cross-section for the four mesh resolutions. Simulated case has $Re_t = 5275$, $Re_n = 626$, $x_o = 58.75$ mm, and $f = 2.46$ Hz.

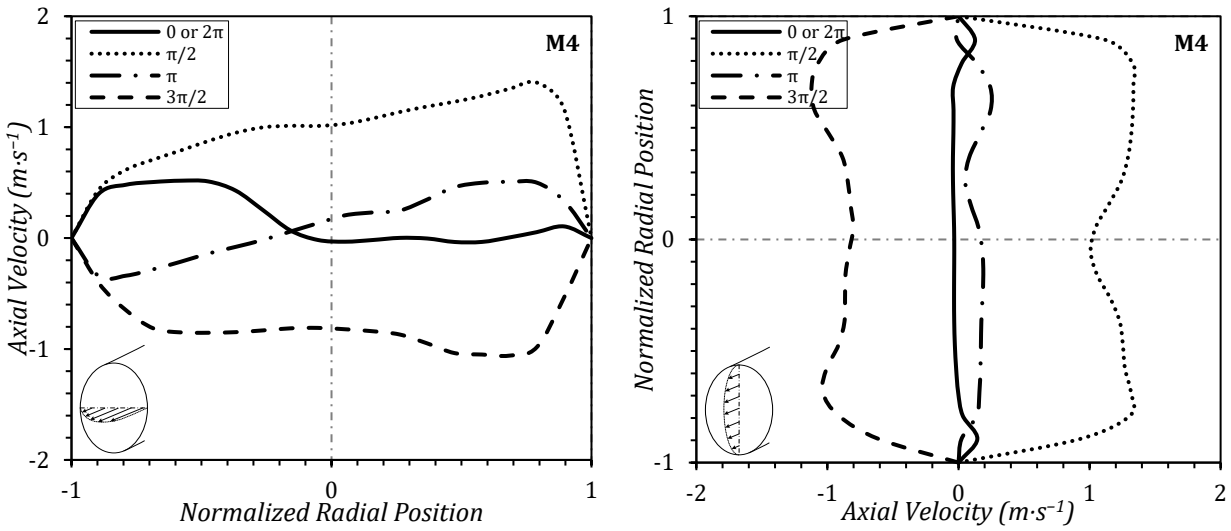

Figure 3-4. (Continued)

parameters. The RTD variance experimental data is summarized as a function of the total Reynolds number in **Figure 3-5** to facilitate this analysis in the following sections. The data clearly shows that a minimum occurs in the observed RTD variance for Re_t in the range of 1000 to 2500 depending on the operating conditions.

Florit et al. developed a correlation for the axial dispersion coefficient for steady flow through coiled tubes. [104] Although the data in the present study is for oscillatory flow, steady flow serves as a reasonable reference for comparison. Therefore, the RTD variance data is plotted alongside the correlation of Florit et al. in **Figure 3-6** with an assumed Schmidt number Sc of 600. Clearly, the steady-flow correlation provides values within the range of the observed experimental RTD variance, and the data also shows a minimum. Consequently, the total Reynolds number appears to be a reasonable scaling parameter.

3.3.3. Velocity profiles

Time-averaged velocity profiles are presented for a selected set of representative conditions in **Figure 3-7**. In addition, the RTD variance and time-averaged axial-to-transverse velocity ratio are also provided in **Figure 3-8**. As shown in the first two rows of **Figure 3-7**, neither the flattening of the axial velocity profile nor the increase in intensity of the transverse velocity profile are monotonic for fixed net flow rate and oscillation frequency. The minimum in the RTD variance (**Figure 3-8**) appears to occur when the intensity of the transverse

velocity is high and the time-averaged axial velocity profile is relatively flat (**Figure 3-7**). At very high oscillation amplitude, the axial velocity profile becomes more complex while the transverse velocity does not significantly increase, which leads to an increase in RTD variance. Comparison of the RTD variance plot with the plot of time-averaged axial-to-transverse velocity ratio in **Figure 3-8** shows that the minimum of the RTD variance seems to occur near the inflection point of the axial-to-transverse velocity ratio data.

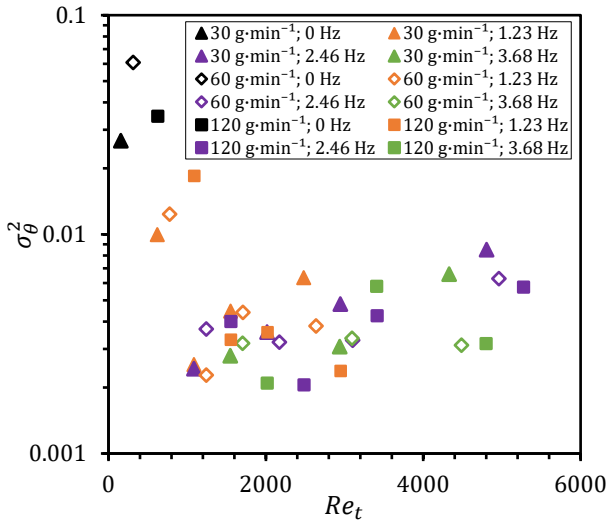

Figure 3-5. Variance of the RTD plotted as a function of the total Reynolds number for various oscillation conditions.

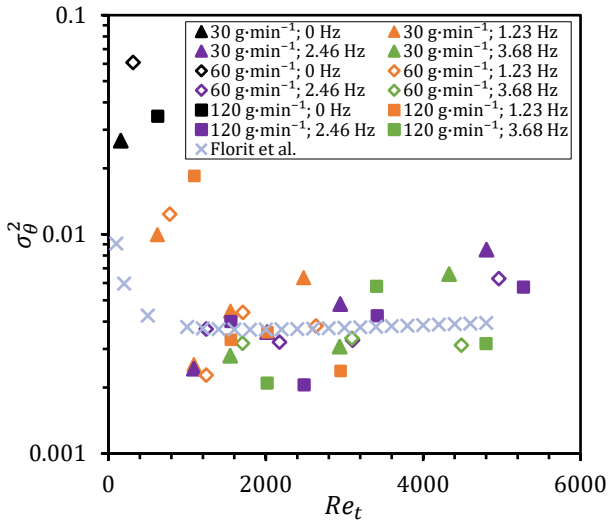

Figure 3-6. Variance of the RTD plotted as a function of the total Reynolds number for various oscillation conditions with comparison against the steady-flow correlation of Florit et al. [104]

The impact of net flow rate on the time-averaged velocity profiles is shown in the third row of **Figure 3-7**. For fixed oscillation frequency, the RTD variance increases with net flow rate for low oscillation amplitudes and decreases with net flow rate for high oscillation amplitudes. This seems to occur because the transverse velocity magnitude is higher for low net flow rate at low oscillation amplitude and lower for low net flow rate at high oscillation amplitude. The trend does not appear to be strongly linked to the change of the shape of the axial velocity profiles.

3.3.4. Power dissipation and phase shift

Viscous power dissipation and phase shift predicted using the simplified calculation method and CFD simulations are compared in **Figure 3-9**. Overall, the simplified calculation method provides a reasonable approximation of both the viscous power dissipation and the phase

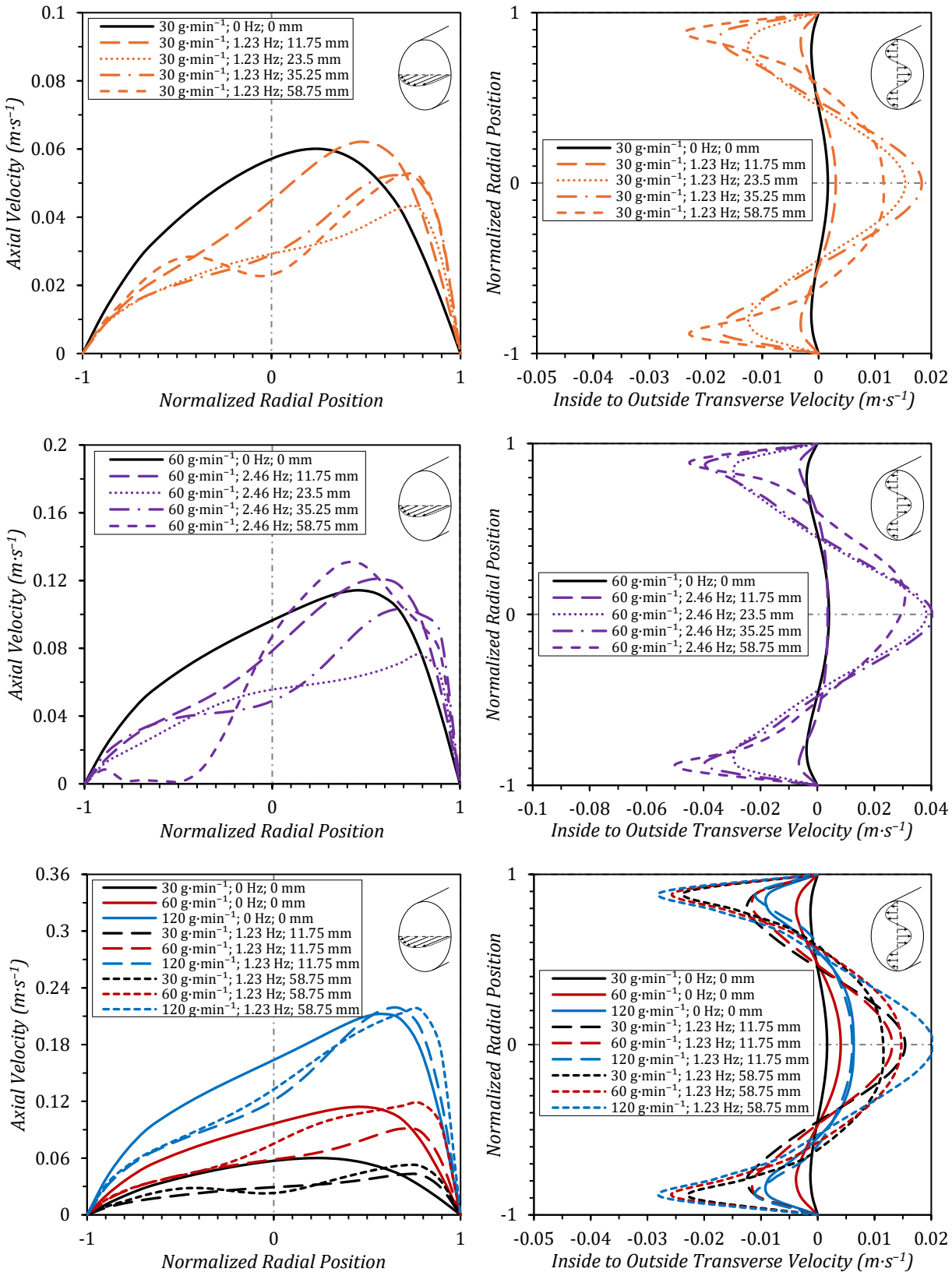

Figure 3-7. Time-averaged axial and transverse velocity profiles for representative conditions.

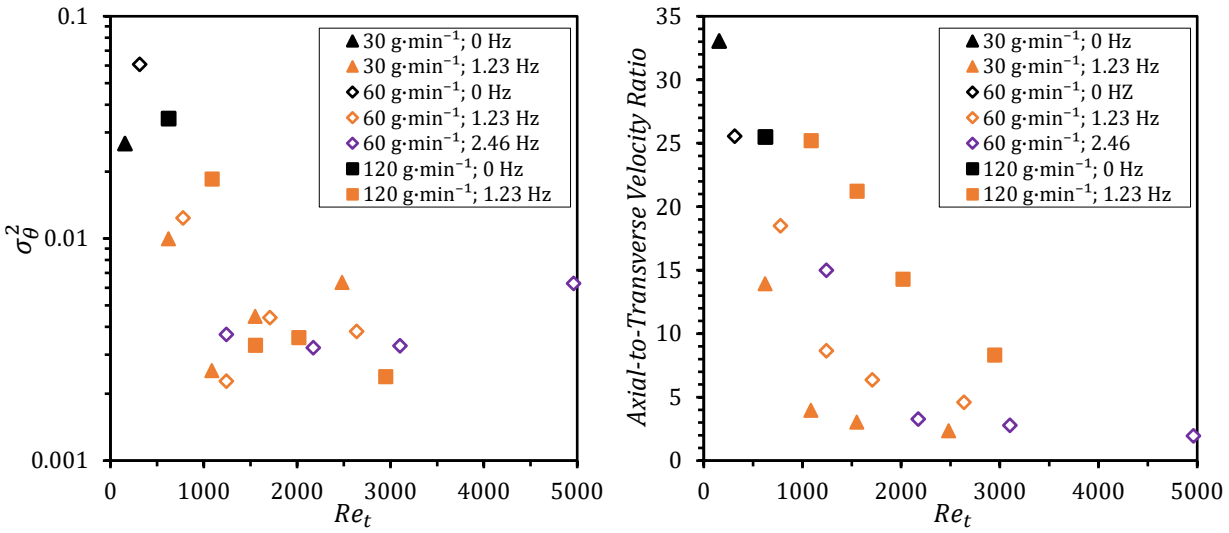

Figure 3-8. Abbreviated summary of RTD variance for the selected conditions in **Figure 3-7** (left), and axial-to-transverse velocity ratio for the selected conditions in **Figure 3-7** (right).

shift. The maximum relative error between predictions is 35 %, but only six conditions have relative errors above 20 %, and the mean relative error is only 11.5 % for all data points. Therefore, the simplified method can be used as a convenient shortcut to estimate power dissipation and phase shift.

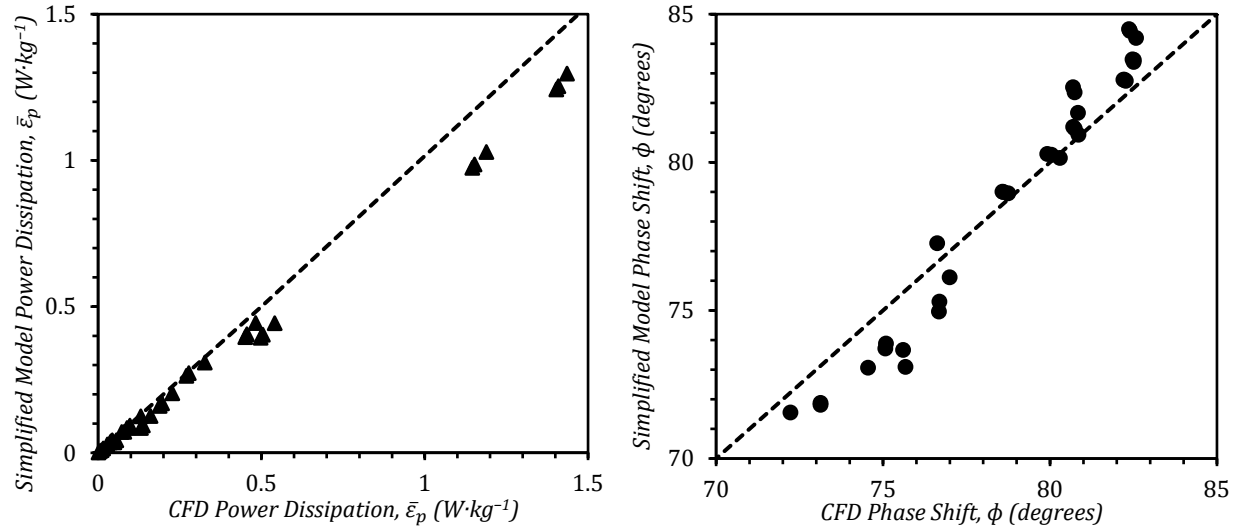

Figure 3-9. Comparison between power dissipation (left) and phase shift (right) predicted using the simplified calculation method and the CFD model.

Nonetheless, power dissipation at some conditions is not as well approximated using the simplified approach as for others. Generally, the conditions where the simplified approach

yields higher errors are those with lower oscillation amplitude because the flow profile develops less throughout the oscillation cycle and the steady-flow friction factor correlation becomes less valid. Instantaneous velocity profiles and the relative error in the viscous power dissipation estimate using the simplified calculation method are presented in **Figure 3-10** for representative conditions. The lowest relative error is obtained for pulsatile (unidirectional oscillatory) flow, and the highest error occurs for low oscillation amplitude.

As discussed in the Methodology in Section 3.2.4, the major limitation of the simplified calculation method is the use of a steady-flow friction factor model. Consequently, the accuracy of the instantaneous power dissipation prediction should be assessed. Instantaneous velocity profiles and the relative error in the viscous power dissipation estimate using the simplified calculation method are presented in **Figure 3-11** for representative conditions. The magnitude of the deviations in the simplified calculation varies throughout the oscillation cycle, which is reasonable considering the development of the velocity profile. In general, better agreement is obtained when the flow is more developed before acceleration/deceleration. Overall, the agreement is reasonable.

Power dissipation can be used as a scaling parameter to make the observed trend in the RTD variance monotonic. The RTD variance normalized by the power dissipation is plotted in **Figure 3-12** for both oscillatory and steady flow. The experimental oscillatory flow data were scaled using power dissipation values obtained from CFD. The steady flow data were obtained by using the correlation of Florit et al. to calculate the RTD variance and using the combination of Equation (3-10), Equation (3-14), and Equation (3-15) to calculate power dissipation.

3.4. Conclusions

In the present work, the fluid dynamics of a single-phase oscillatory flow in a baffleless coil reactor was numerically simulated to determine the viscous power dissipation and the phase shift between the velocity and pressure drop using simulated the instantaneous axial and transverse velocity profiles and pressure drop gradient along the coil. Based on the mechanical energy balance equation, a simplified method was developed to estimate the

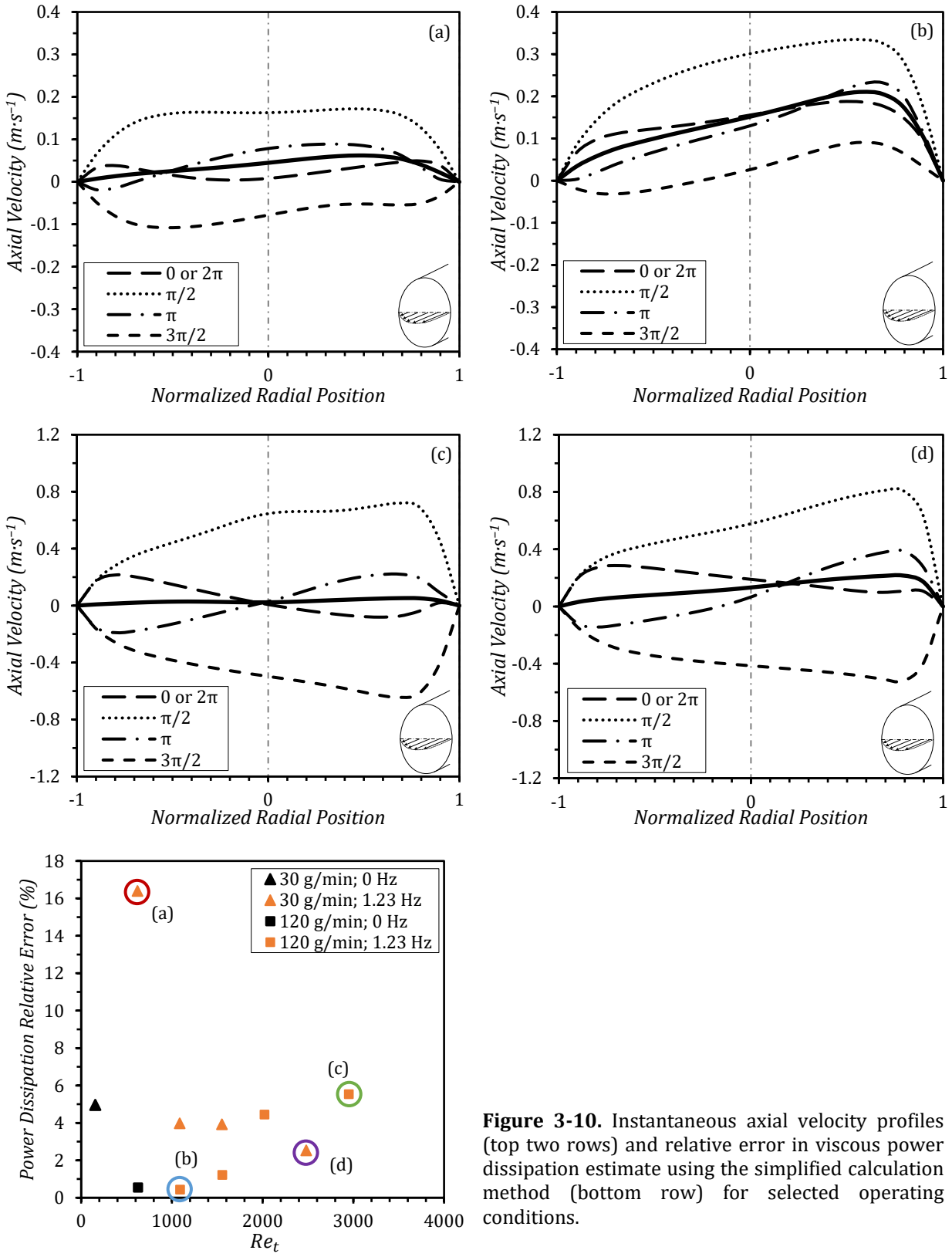

Figure 3-10. Instantaneous axial velocity profiles (top two rows) and relative error in viscous power dissipation estimate using the simplified calculation method (bottom row) for selected operating conditions.

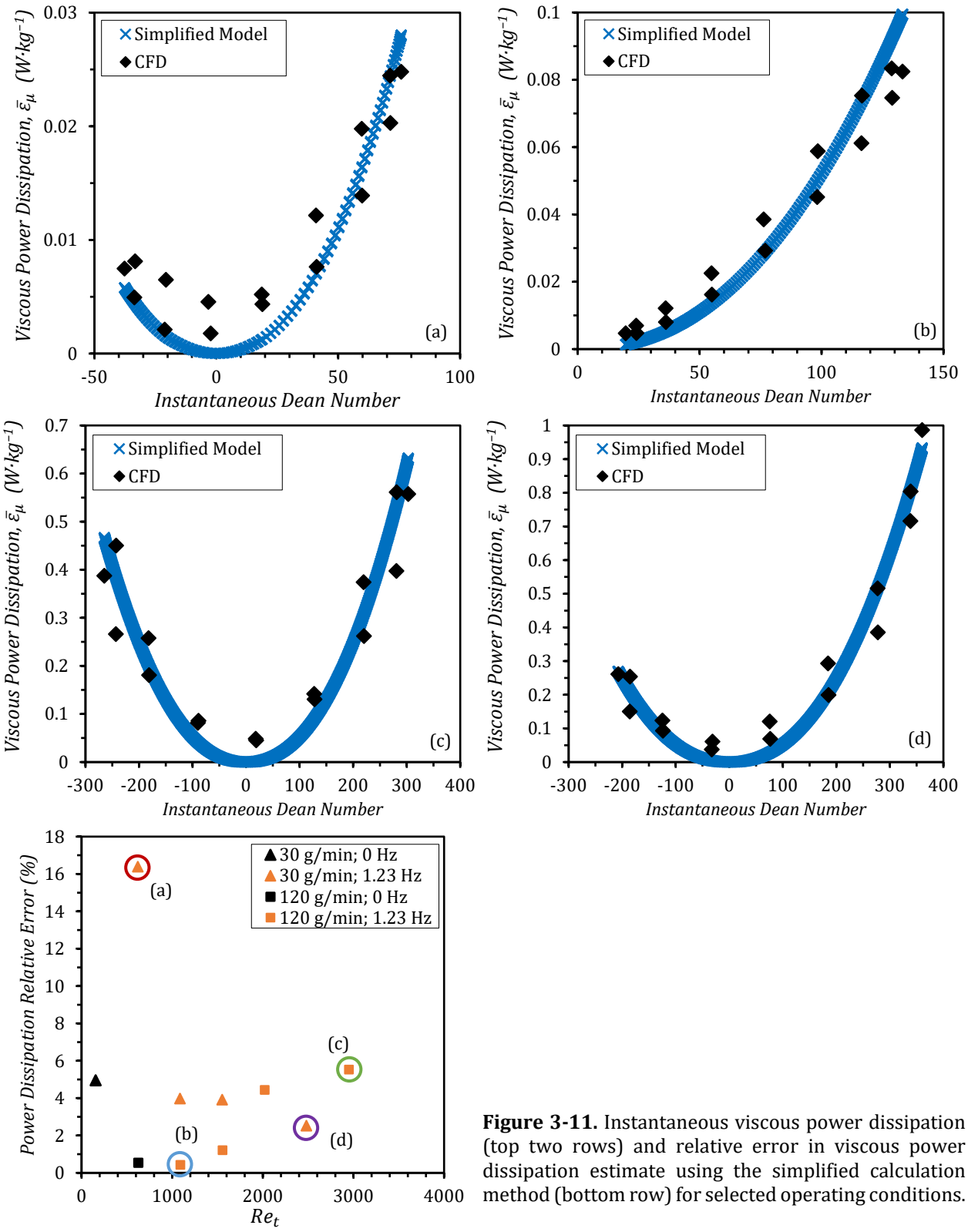

Figure 3-11. Instantaneous viscous power dissipation (top two rows) and relative error in viscous power dissipation estimate using the simplified calculation method (bottom row) for selected operating conditions.

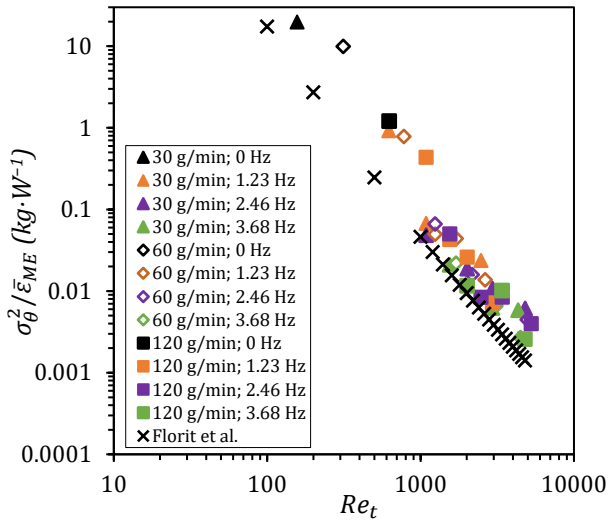

Figure 3-12. Variance of the RTD normalized by the mechanical power dissipation and plotted as a function of the total Reynolds number for various oscillation conditions with comparison to steady flow.

viscous power dissipation and phase shift using a correlation for the steady flow Fanning friction factor. Comparison of the simulated quantities and the estimated ones using the simplifies method displays satisfactory agreement between the two methods, suggesting that the simplified method can be used as a convenient shortcut to estimate the viscous power dissipation and phase shift. Nonetheless, the error associated with the simplified method increases at low values of the oscillation amplitude because the flow is less developed at lower amplitudes while the Fanning friction factor is essentially for developed flow.

The evolution of the viscous power dissipation vs. the instantaneous Dean number displays a minimum, similar to what was observed in the RTD variance trends. In addition, their minimums occur in a similar range of the instantaneous Dean number as both viscous power dissipation and RTD variance strongly depend on the axial to transverse velocity ratio. According to this relation, the RTD variance was normalized with the viscous power dissipation to attain a monotonic trend of the normalized RTD variance vs. the total Reynolds number.

Nomenclature

Latin Letters

A_C	m^2	internal coil cross-sectional area
D_{AB}	$m^2 \cdot s^{-1}$	Mass diffusivity
D_t	m	internal coil diameter
De_n	-	net flow Dean number
De_o	-	oscillatory flow Dean number
E_{ME}	W	mechanical power
E_μ	W	viscous power
f	Hz	oscillation frequency
$f_{fanning}$	-	Fanning friction factor
F_{loss}	$kg \cdot m^{-2} \cdot s^{-2}$	frictional losses
L	m	coil length
p	Pa	pressure
p'	$m^2 \cdot s^{-2}$	pressure normalized by density, p/ρ
Pe	-	Péclet number
r	m	radial coordinate referenced to the centre of the inlet boundary
R_c	m	coil radius of curvature
Re_n	-	net flow Reynolds number
Re_o	-	oscillatory flow Reynolds number
Re_t	-	total Reynolds number, $Re_t = Re_n + Re_o$
Sc	-	Schmidt number, $Sc = \nu/D_{AB}$
t_1 or t_2	s	time integration limits
U_{in}	$m \cdot s^{-1}$	axial velocity on the inlet boundary
$\overline{U}$	$m \cdot s^{-1}$	instantaneous cross-sectionally averaged axial velocity
$\overline{\overline{U}}$	$m \cdot s^{-1}$	time and cross-sectionally averaged axial velocity or net velocity
$\mathbf{U}$	$m \cdot s^{-1}$	velocity vector
U_o	$m \cdot s^{-1}$	oscillatory flow velocity
x_o	m	oscillation amplitude

Greek letters

$\bar{\varepsilon}_{ME}$	$W \cdot kg^{-1}$	time-averaged power dissipation based on mechanical power
$\bar{\varepsilon}_\mu$	$W \cdot kg^{-1}$	time-averaged power dissipation based on viscous power
$\bar{\varepsilon}_p$	$W \cdot kg^{-1}$	time-averaged power dissipation based on pressure drop
σ_θ^2	-	variance (second moment) of the RTD
ϕ	°	phase shift
ν	$m^2 \cdot s^{-1}$	kinematic viscosity
ρ	$kg \cdot m^{-3}$	density
$\boldsymbol{\tau}$	Pa	stress tensor

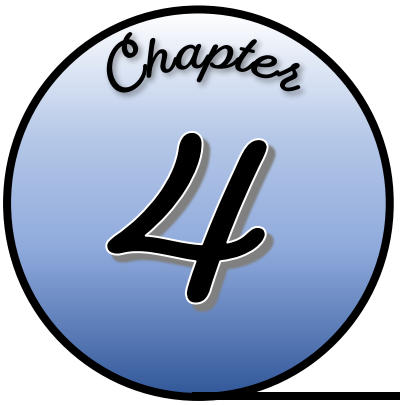

Oscillation-intensified Heat Transfer

4.1. Introduction

In some applications of the fine chemicals industry, there is a tendency for migration from batch to continuous reactors [14–17]. Therefore, continuous microreactors are gradually being commercialised, especially where the production scale is relatively small. [19] Microreactors have small characteristic dimensions; thus, in the absence of a secondary perturbation agent, the flow regime is laminar. The enhancement of transport coefficients is therefore of interest, especially when microreactors are to be employed as an industrial option. For example, an increase in mass transfer coefficients in single-phase and multiphase reactors is possible when the quality of mixing is improved by adding inner inserts or changing the flow path/cross-section (passive mixing). [21,105] Applying energy from an external source to the flow (active mixing) can also lead to higher transfer coefficients while decoupling transfer rates from the net flow rate. [21]

One of the most commonly used continuous microreactors is a baffleless coil reactor. These reactors are easy to manufacture because of their simple structure, and they do not need inserts to increase mixing since secondary flows are generated at the center of their cross-sections due to curvature. This feature is an important advantage over other types of reactors when a solid-forming reaction occurs because they are less prone to fouling/blocking and easier to clear.

Creating curvature in a tube as a passive mixing method can also enhance the convective heat transfer coefficient due to the generation of secondary flows. [59,60] For a straight rectangular channel followed by a single curved section, the Nusselt number in the curved section at low Dean numbers (the product of the Reynolds number and the square root of the relative curvature) is lower than or approximately equal to that in the straight channel. [59] However, at higher Dean numbers, the Nusselt number increases in the curved section beyond that in the previous straight channel. Moreover, the local Nusselt number in the curved section is higher near the concave wall since the velocity is greater than near the convex wall. Enhancement of the convective heat transfer coefficient has been investigated for longer curved tubes in the shape of helical and spiral coils and the results have been correlated with the operating conditions, fluid properties, and coil dimensions, especially the relative curvature. [60,106,107] Some studies show that the results can be correlated with

the Dean number, while others show that the Reynolds number and relative curvature should be considered in a correlation individually with different exponents to better correlate data. [60,106,107] A study on local heat transfer in helical coils [108] shows that the local Nusselt number initially increases over the tube length and then decreases and reaches a plateau (thermally developed region) so that a maximum is observed in the local Nusselt number profile. The location and value of this maximum are both functions of the Reynolds number as well as the local Nusselt number in the thermally developed region, unlike straight pipes.

Employing an active mixing method can enhance the quality of mixing and convective transport coefficients in baffleless coil reactors. Applying oscillation as an active mixing method to the fluid flowing in a coil generates the secondary flows more intensely, increasing the transverse dispersion as well as the plug flow performance. [44,101] Furthermore, intensifying the secondary flows by oscillation can enhance the fluid-to-wall heat transfer coefficient. [46] In a recent article by Law et al. [61], the enhancement of the convective heat transfer coefficient for an oscillatory flow baffled reactor was studied. Based on the results provided, for a studied range of the net flow Reynolds number, the profile of the Nusselt number vs. the oscillatory Reynolds number has a maximum point because the radial mixing is limited by the tube walls, while there is not such a limitation for the axial mixing beyond the maximum point. In two other studies, the effect of pulsating on-off flow with a square pulse velocity profile on fluid-to-wall heat transfer was studied for helical and conical coils. [98,99] These studies showed that the pulsating flow can increase the convective heat transfer coefficient, and this pulsating enhancement can be correlated with the Womersley number and coil dimensions. However, a pulsating on-off flow cannot be considered oscillatory as the fluid always moves forward, and the pulsating amplitude is not independent of the net flow so that this parameter has not been considered in the analyses provided by the aforementioned studies.

Oscillatory flow coil reactors are a promising choice for intensifying batch reactors, especially when handling solid-forming reactions [20,81] and when thermal management is critical. Therefore, a major objective of the present study is to measure the heat transfer rate between an oscillatory flow in a coil reactor and a fixed-temperature external medium and to provide comprehensive robust correlations to accurately predict the convective heat transfer

coefficient under oscillatory conditions, which is essential for reactor design and scale-up. Because scaled-up equipment has a lower surface-to-volume ratio, the enhancement of the fluid-to-wall heat transfer coefficient is highlighted to prevent the need to increase coil length for heat transfer purposes. The convective heat transfer coefficient for steady flow is analyzed in detail in relation to coil dimensions and operating conditions to prepare a basis for comparison between oscillatory and non-oscillatory flow. A custom experimental system is used to apply a sinusoidal velocity profile as this type of oscillation is the most conventional one, and the obtained data points can be used in possible numerical studies in the future. Since the length of a continuous reactor is one of the most important quantities in its design, the relation between the coil heat transfer coefficient and its length is also studied, considering that this quantity has not been taken into account in the literature for heat transfer in helical coils. Furthermore, coils with varying diameters and radii of curvature are investigated to explore the impact of these important geometric parameters. The experimental data are used to develop comprehensive correlations and to explore the underlying physical mechanisms.

4.2. Experimental

Heat transfer studies were performed using the experimental apparatus having the process flow diagram shown in **Figure 4-1.** This apparatus comprised an insulated spool made of 6-inch CPVC NPT pipe (schedule = 80, height = 1.1 m, inner diameter ($D_{j,i}$) = 146.3 mm) as the jacket to heat coils, a heating circulator (Huber Ministat 230, maximum heating power = 1000 W) thermally reinforced by a 3200 W immersion heater as the heat source, a refrigerated bath (Fisher, Isotemp 4100) equipped with a metal coil to cool the inlet water when required, a magnetic drive pump with a stainless steel impeller and casing (Laing SM-1212-STW-26) connected to a mixing nozzle (orifice diameter = 3/16 inch, circulation rate = 36.8 gpm at 50 psi) installed in the jacket to provide turbulence in the jacket, a syringe pump (SyrDos, Hitec Zang) capable of continuously injecting fluids for low flow rates up to 300 ml·min^{-1}, an oscillator (explained subsequently), and two stainless steel valve arrangements at the inlet and outlet of the jacket. The oscillator consisted of a glass syringe with a capacity (1/2.5/10 ml) connected to a reciprocating rod actuated by a high-torque variable-speed DC gear motor (E-S motor, maximum rotational speed = 666 rpm, maximum voltage = 24 V, maximum power = 120 W).

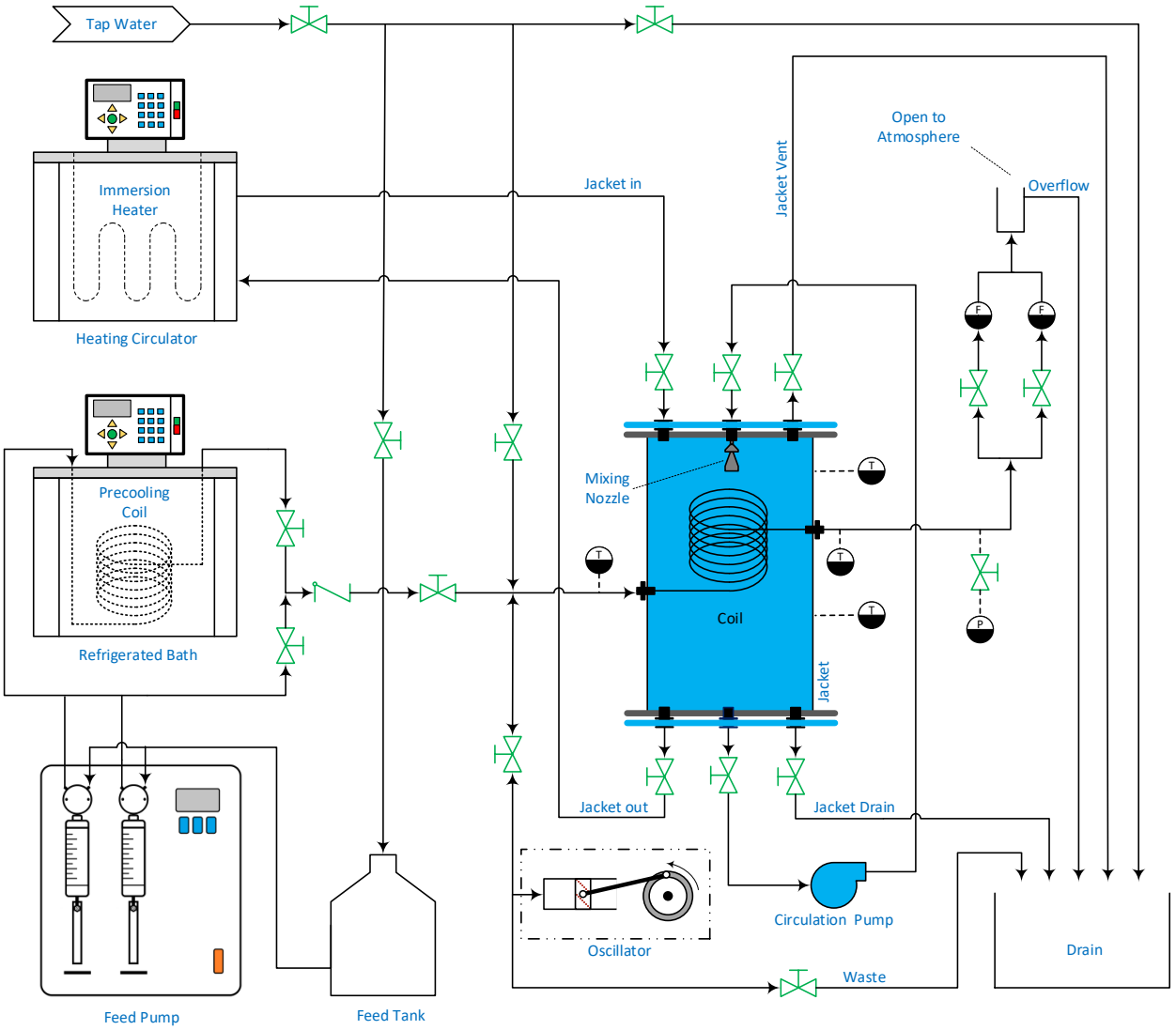

Figure 4-1. Process flow diagram of the experimental setup.

The inlet valve arrangement was used to adjust the operating modes (non-oscillatory or oscillatory) and deaerate the oscillator when required. The outlet valve arrangement was used to measure high feed flow rates (supplied by tap water) using two rotameters with different ranges (0.2–2 and 2–20 GPM, King Instrument) and also measure oscillatory velocity profiles by a pressure transmitter (Omega PX409-015GI, 0–1 barg) connected to a high sampling rate current-input data acquisition system (National Instrument, NI-9203 installed on NI-cDAQ-9171 chassis). Four temperature sensors (PT-1000, Omega PR-10L-4-1000-1/8-4) connected to a data acquisition system (Moxa ioLogik E-2260) were installed at the inlet and outlet of the coil and in the jacket at the top and bottom of the coil to measure

the temperature with a precision of ± 0.1 °C. A cylindrical overflow container (ID = 5 cm) was connected to the outlet stream to minimize pressure fluctuations at the outlet under oscillatory conditions and provide the coil with a proper fluid head, avoiding two-phase flow at low flow rates.

Ten coils (3003 aluminum, $k_{Al} \approx 173$ W.m^{-1}.K^{-1}) with different lengths (l), tube diameters ($d_{t,i}$), and mean diameter of curvature ($\bar{D}_c = (D_{c,i} - D_{c,o})/2$) were constructed to analyze heat transfer enhancement under both non-oscillatory and oscillatory conditions. Their tube pitches (P_t) were approximately 1.25 $d_{t,o}$. However, they were slightly varied depending on the inlet and outlet tube connectors. **Table 4-1** summarizes the dimensions of the coils along with the ranges of relevant dimensionless groups used in this study. To eliminate any perturbation at the inlets of the coils and reduce the pressure drop, their inlets and outlets in the jacket were tangent to the circumference of the coils. The number of turns for each coil was an integer, and only a short straight length at the inlet and outlet was used to connect the coil to the inlet and outlet connectors. This extra length at maximum (i.e., for the shortest Coil 8) was less than 2.5% of the entire coil length. The inlet and outlet of the installed coil were connected to thick plastic tubes with a plastic connector to minimize heat transfer outside the outer surface of the coil.

After installing a coil in the jacket, the jacket and coil piping were filled with water and deaerated by flowing water through the coil at a high flow rate. Then the jacket was heated by the heating circulator up to 85 °C. Once the jacket temperature reached a steady state, the circulation pump was started, and the flow rate was set by the syringe pump or the tap water valve. Waiting until steady state (constant temperature ±0.1°C), the temperatures were recorded for 2 min, and their averages were considered as the steady-state non-oscillatory temperatures.

The tap water had a temperature around 20 °C, and the jacket temperature was initially selected as 85 °C for low flow rates. However, as the flow rate increased, the heating circulator and immersion heater were not able to keep the jacket at this temperature because the sum of the heat transferred to the coil and the heat loss of the jacket and piping exceeded their maximum power. Therefore, at higher flow rates, the steady-state jacket temperature

Table 4-1. Coil dimensions and ranges of related dimensionless groups for non-oscillatory and oscillatory flows.

Coil	$d_{t,i}$ *(mm)*	$d_{t,o}$ *(mm)*	$\bar{D}_c$ *(mm)*	*l (m)*	P_t *(mm)*	N_t	*Le*	*Cu*	$Re_{t,n}$ *(Non-osci.)*	De_n	$Re_{t,n}$ *(Osci.)*	$Re_{t,o}$	*Flow*
Coil 1	10.92	12.70	104.7	1.955	16	6	179.0	0.104	86–31113	27–10037	-	-	Non-osci.
Coil 2	6.17	7.94	99.9	2.197	10	7	356.0	0.062	77–30818	19–7655	-	-	Non-osci.
Coil 3	6.17	7.94	69.9	1.545	10	7	250.3	0.088	76–30236	22–8973	-	-	Non-osci.
Coil 4	6.17	7.94	50.9	1.113	10	7	180.3	0.121	76–32627	26–11335	-	-	Non-osci.
Coil 5	3.35	4.76	54.8	1.212	6	7	361.5	0.061	141–34467	34–8523	-	-	Non-osci.
Coil 6	3.35	4.76	39.8	0.864	6	7	257.7	0.084	140–33126	41–9608	-	-	Non-osci.
Coil 7	3.35	4.76	26.8	0.585	6	7	174.5	0.125	140–338645	49–13644	-	-	Non-osci.
Coil 8	3.35	4.76	26.8	0.204	10	2	60.8	0.124	112–36622	39–12871	112–9778	410–8043	Non-osci. & Osci.
Coil 9	6.17	7.94	50.9	0.330	12	2	53.5	0.120	62–35770	21–12416	62–7521	849–9247	Non-osci. & Osci.
Coil 10	3.35	4.76	54.8	0.376	10	2	109.5	0.061	113–34776	28–8590	113–10316	387–8159	Non-osci. & Osci.

was lower. The water flow rate was between 10 and 15000 ml·min^{-1}, so that the lower limit was identical for all the coils, but the upper limit was limited by the installed coil friction or the source of water.

Following a non-oscillatory flow experiment, a set of oscillatory flow experiments at different values of frequency (1–6 Hz) and amplitude (14–42 mm) was performed for Coils 8, 9, and 10. After setting the frequency and amplitude to certain values, the position of the valve between the oscillator and the coil inlet was changed to open, and the oscillator started. The procedure for recording the data after reaching a cyclic steady state was identical to previously described. Accurate calculation of the convective heat transfer coefficient requires a sufficiently high temperature difference between the coil outlet and the jacket. Since the convective heat transfer coefficient was increased by oscillation, it was necessary to maintain an effective temperature difference by using only short coils (Coils 8, 9, and 10) and passing the inlet water through a cooling coil in the refrigerated bath set to 5°C to decrease the coil inlet temperature. In addition, the mentioned coils were installed very close to the mixing nozzle in the jacket to decrease the jacket-side heat transfer resistance, which made the tube-side resistance comparable to the jacket side and thereby decreased the error of calculating the resistances (see the Section 4.3).

For both non-oscillatory and oscillatory experimental plans, around 20 % of the experiments were repeated three times to assess precision of the results; the relative standard deviation of the measured temperatures was at maximum 3 %.

4.3. Data Analysis

The first step in determining the tube-side heat transfer coefficient is the calculation of the overall heat transfer coefficient, which needs the heat transfer rate from the jacket to the coil at a steady state:

$$\dot{Q} = \dot{m}\, C_{p,m}\left(T_{t,o} - T_{t,i}\right) \tag{4-1}$$

where $\dot{Q}$ is the heat transfer rate, $\dot{m}$ is the water mass flow rate, $C_{p,m}$ is the mean fluid heat capacity at the film temperature (discussed later), and $T_{t,o}$ and $T_{t,i}$ are the coil outlet and inlet

temperatures. Using the LMTD (logarithmic mean temperature difference) method [109] the overall heat transfer coefficient (U) is determined as follows, considering that the flow arrangement is counter-current:

$$\dot{Q} = U\ A\ LMTD \quad \Longrightarrow \quad U = \frac{\dot{Q}}{A\ LMTD} \tag{4-2}$$

$$LMTD = \frac{(T_{j,o} - T_{t,i}) - (T_{j,i} - T_{t,o})}{ln[(T_{j,o} - T_{t,i})/(T_{j,i} - T_{t,o})]} \tag{4-3}$$

where A is the heat transfer surface area, and $T_{j,o}$ and $T_{j,i}$ are the jacket temperatures at the bottom and top of the coil.

The second step is to determine the jacket-side and the conduction heat transfer resistances and subtract them from the overall heat transfer resistance. A common method to estimate the jacket-side resistance is the calculation of the overall heat transfer coefficient at very high values of the Reynolds number in the tube and then the determination of the limiting resistance by extrapolation when the tube-side heat resistance approaches zero (i.e., when the Reynolds number approaches infinity).[110] Although this method provides a good estimation, it does not account for the temperature dependence of the tube-side Prandtl number or jacket-side fluid properties, which introduces error into the estimated value. In this work, a better estimate of the jacket-side resistance will be provided. Equation **(**4-4) expresses the overall heat transfer resistance:

$$R_{total} = \frac{1}{U\ A} = \frac{1}{\pi d_{t,i}\ l\ \bar{h}_t} + \frac{ln(d_{t,o}/d_{t,i})}{2\pi k_{Al} l} + \frac{1}{\pi d_{t,o}\ l\ \bar{h}_j} \tag{4-4}$$

where $d_{t,i}$ and $d_{t,o}$ are the inner and outer diameters of the coiled tubes, k_{Al} is the aluminum thermal conductivity, and $\bar{h}_t$ and $\bar{h}_j$ are the tube-side and jacket-side average convective heat transfer coefficients. If A is considered as the inner surface area of the tube ($A_{t,i} = \pi d_{t,i}\ l$), Equation (4-5) is simplified as follows:

$$\frac{1}{U} = \frac{1}{\bar{h}_t} + \frac{d_{t,i}\ ln(d_{t,o}/d_{t,i})}{2k_{Al}} + \frac{d_{t,i}}{d_{t,o}\ \bar{h}_j} \tag{4-5}$$

Given that k_{Al} is known and is not sensibly changed over the range of temperature in this work, the conductive resistance can be subtracted from the right-hand side of Equation (4-5) to obtain the total convective resistance:

$$R_{Conv}A_{t,i} = \frac{1}{U} - \frac{d_{t,i}\,ln(d_{t,o}/d_{t,i})}{2k_{Al}} = \frac{1}{\bar{h}_t} + \frac{d_{t,i}}{d_{t,o}\,\bar{h}_j} \tag{4-6}$$

The jacket-side average Nusselt number ($\overline{Nu_j}$) can be expressed by a power-law equation in terms of the Reynolds and Prandtl numbers (Re_j and Pr_j).[111] As data trends will show later, the tube-side Nusselt number ($\overline{Nu}_{t,n}$) at high Reynolds numbers can be expressed in terms of the Reynolds and Prandtl numbers ($Re_{t,n}$ and Pr_t) and the relative curvature (Cu).[60]

$$\overline{Nu_j} = \frac{\bar{h}_j D_{j,i}}{k_{f,j}} = a\,Pr_j^{1/3} Re_j^b \quad \Longrightarrow \quad \bar{h}_j = \frac{a\,Pr_j^{1/3} Re_j^b\,k_{f,j}}{D_{j,i}} \tag{4-7}$$

$$\overline{Nu}_{t,n} = \frac{\bar{h}_t d_{t,i}}{k_{f,t}} = c\,Pr_t^{1/3} Re_{t,n}^d\,Cu^e \quad \Longrightarrow \quad \bar{h}_t = \frac{c\,Pr_t^{1/3} Re_{t,n}^d\,k_{f,t}}{d_{t,i}}\,Cu^e$$
$$Cu = \frac{d_{t,i}}{\bar{D}_{c,corr}} \tag{4-8}$$

$$\bar{D}_{c,corr} = \bar{D}_c\left[1 + \left(\frac{P_t}{\pi \bar{D}_c}\right)^2\right]$$
$$\bar{D}_c = \frac{D_{c,i} + D_{c,o}}{2} \tag{4-9}$$

where $D_{c,corr}$ is the mean of the coil inner and outer diameters corrected by P_t, [91] and $k_{f,j}$ and $k_{f,t}$ are the thermal conductivities of the fluids flowing in the jacket and coiled tube, respectively. The subscript n, standing for net flow, was added to the tube-side Reynolds number and heat transfer coefficient to distinguish between the net flow and oscillatory flow which will be discussed later. The exponent 1/3 for both Prandtl numbers is the most common value in the literature and is not generally affected by the flow regime. In Equation (4-7), the jacket-side fluid velocity (included in Re_j), a, and $D_{j,i}$ are constant. Substituting

Equations (4-7) and (4-8) into Equation (4-6) and combining the constants yields Equation(4-10):

$$R_{Conv}A_{t,i} = \frac{d_{t,i}}{c\ Pr_t^{1/3} Re_t^d\ k_{f,t} Cu^e} + \frac{m}{Pr_j^{1/3}\left(\rho_j/\mu_j\right)^b\ k_{f,j}} \tag{4-10}$$

The second term of Equation (4-10)(the jacket-side resistance) is valid for all values of $Re_{t,n}$ as the jacket fluid velocity remains constant for each coil during the experiments. The experimental R_{Conv} data at high values of $Re_{t,n}$ (greater than the critical Reynolds number, Re_{cr}) were initially calculated at the estimated film temperatures (Equations (4-11) and (4-12)). Then the data points of each coil were fitted with Equation (4-10) using the nonlinear generalized reduced gradient algorithm present in Microsoft Excel with the objective that the fitting R^2 is maximized.

$$T_{f,t}^{initial} = \frac{T_{t,i} + T_{t,o} + T_{j,i} + T_{j,o}}{4} \tag{4-11}$$

$$T_{f,j}^{initial} = \frac{T_{f,t}^{initial} + (T_{j,i} + T_{j,o})/2}{2} \tag{4-12}$$

From the initial fits, the values of c, d, and e did not show dependence on the tube length. The average value of b was 0.595, which agrees with the Reynolds number exponent in the literature (0.62).[111] To decrease the error of fitting, b was set at 0.62, and the data points were again fitted to obtain $\overline{Nu}_{t,n}$:

$$\overline{Nu}_{t,n} = \frac{h_{t,n}d_{t,i}}{k_{f,t}} = \frac{d_{t,i}}{k_{f,t}}\left(R_{Conv}A_i - \frac{m}{Pr_j^{1/3}\left(\rho_j/\mu_j\right)^{0.62}\ k_{f,j}}\right) \tag{4-13}$$

The iterative procedure shown in **Figure 4-2** was then followed to correct the constants c, d and e, and the film temperatures using Equations (4-15) and (4-17) so that these constants and m converged to constant values. It is important to note that the procedure explained above provides a more accurate jacket resistance than the one obtained from a limiting resistance because the temperature dependence of the fluid properties is included in the calculations, and the film temperatures are iteratively corrected.

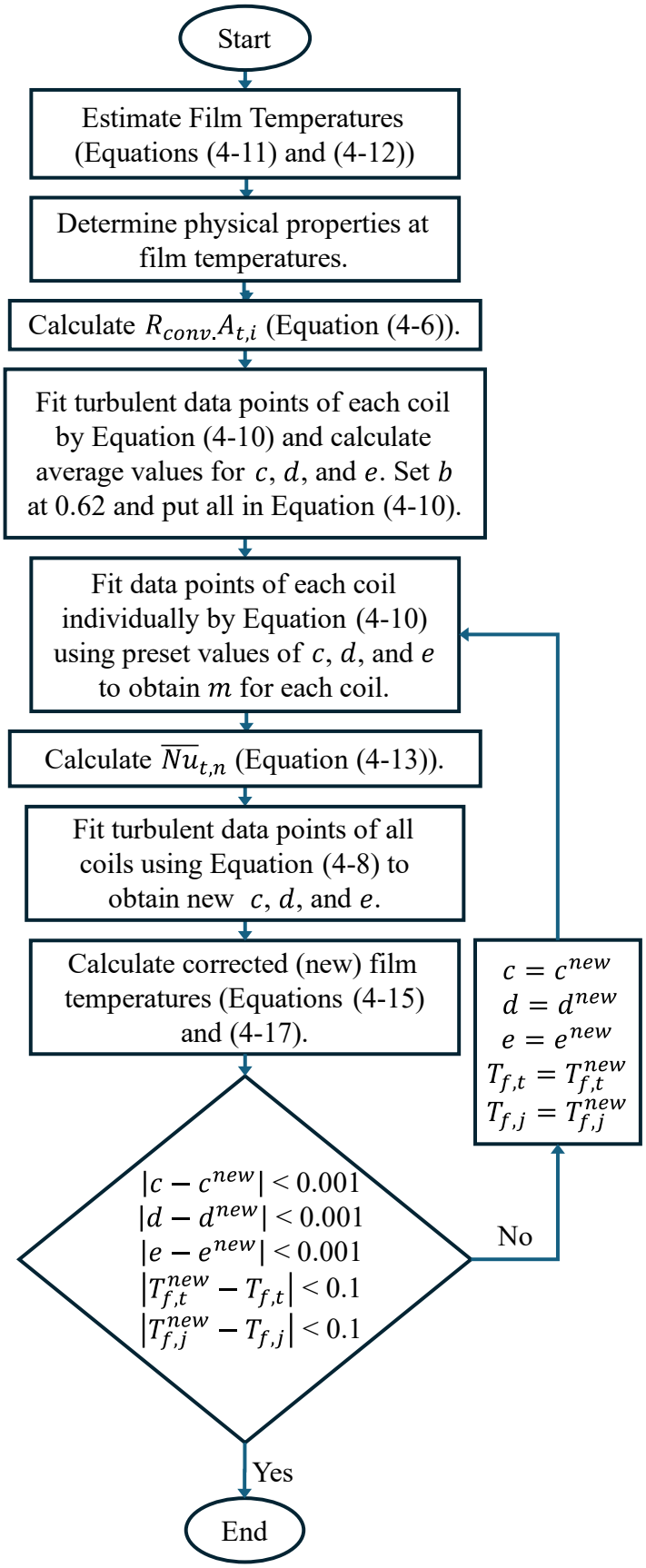

Figure 4-2. Procedure for the determination of the jacket-side convective resistance.

$$\bar{T}_{s,i} = \frac{\dot{Q}}{h_t A_{t,i}} + \frac{T_{t,i} + T_{t,o}}{2} \tag{4-14}$$

$$T_{f,t}^{corrected} = \frac{\bar{T}_{s,i} + (T_{t,i} + T_{t,o})/2}{2} \tag{4-15}$$

$$\bar{T}_{s,o} = \frac{\dot{Q}\, ln\left(d_{t,o}/d_{t,i}\right)}{2\pi k_{Al} l} + \bar{T}_{s,i} \tag{4-16}$$

$$T_{f,j}^{corrected} = \frac{\bar{T}_{s,o} + (T_{j,i} + T_{j,o})/2}{2} \tag{4-17}$$

For the oscillatory flow, the non-oscillatory jacket-side resistance obtained by the aforementioned procedure was used to calculate the average total Nusselt number ($\overline{Nu}_{t,total}$). This quantity was split into the net flow (non-oscillatory, $\overline{Nu}_{t,n}$) and oscillatory flow ($\overline{Nu}_{t,o}$) terms (Equation (4-18)), and then the values of $Nu_{t,o}$ were correlated with the operating conditions. This will be discussed in Section 4.4.2.

$$\overline{Nu}_{t,total} = \overline{Nu}_{t,n} + \overline{Nu}_{t,o} \quad \Rightarrow \quad \overline{Nu}_{t,o} = \overline{Nu}_{t,total} - \overline{Nu}_{t,n} \tag{4-18}$$

4.4. Results and Discussion

4.4.1. Non-Oscillatory Flow

Figure 4-3-a presents the evolution of $\overline{Nu}_{t,n}$ with $Re_{t,n}$ for Coil 1 where a substantial change in the trend forms of a breaking point (BP). The Reynolds number at the breaking point ($Re_{t,BP}$) was numerically calculated around $Re_{t,BP}$ = 1348 by equating the line equations obtained from the data points at both sides of BP, as shown in **Figure 4-3-b**. The values of Re_{cr} for the helical coils in this study were determined using the correlation suggested by Ito et al. [102]:

$$Re_{cr} = 2000(1 + 13.2Cu^{0.6}) \tag{4-19}$$

BP and Re_{cr} divide the plot in **Figure 4-3-a** into 3 zones. In Zone I, the plot curvature before BP is concave up at lowest values of $Re_{t,n}$ and then changes to concave down so that the behavior of $\overline{Nu}_{t,n}$ at values of $Re_{t,n}$ up to the breaking point is S-shape, and an inflection point thus appears. At Re_{cr}, no change in the slope is observed and the trend remains similar to just before this point.

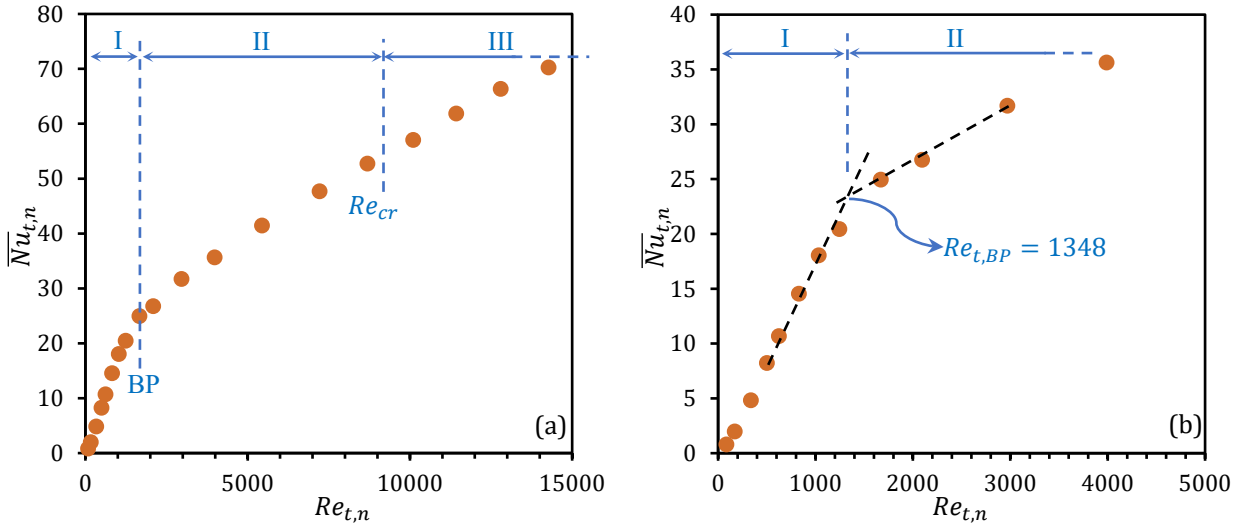

Figure 4-3. Evolution of $\overline{Nu}_{t,n}$ vs. $Re_{t,n}$ for Coil 1: a. Zones I, II, and III according to BP and Re_{cr}, b. Determination of $Re_{t,BP}$.

According to a recent study, [112] the flow field is disturbed by the secondary flows as soon as there is curvature. Therefore, the flow in curved pipes cannot be considered unidirectional even at very low values of $Re_{t,n}$. This agrees with the trend of $Nu_{t,n}$ at low values of $Re_{t,n}$ in which the $Nu_{t,n}$ increases with increasing $Re_{t,n}$ (see **Figure 4-3**). The breaking point can be observed in several experimental studies, [113–118] and has been predicted numerically.[100] However, it has not been reported and discussed. To identify the nature of this point, the flow regime at the breaking point needs to be determined. **Table 4-2** lists the values of $Re_{t,BP}$ and Re_{cr} for different coils listed in **Table 4-1**. These values show that BP occurs at values of $Re_{t,n}$ which are much less than Re_{cr}. As a result, the BP is not related to the change in the flow regime but due to relative proportion of developing and developed flow in the coil.

For two coils having the same values of $d_{t,i}$ and Cu but different lengths, $Re_{t,BP}$ is lower in the shorter coil (e.g., Coils 10 versus 5). According to the models of flow development, if two similar pipes with different lengths encounter heat transfer at identical operating conditions, the shorter one has a higher average fluid-to-wall heat transfer coefficient because the local heat transfer coefficient decreases with increasing length. [109] **Figure 4-4** indeed shows that the shorter Coil 10 provides a greater heat transfer coefficient than Coil 5.

Table 4-2. Values of $Re_{t,BP}$ and Re_{cr} for different coils.

Coil	$Re_{t,BP}$	Re_{cr}
Coil 1	1348	8792
Coil 2	1918	6963
Coil 3	1503	8145
Coil 4	1209	9424
Coil 5	2415	6937
Coil 6	1658	7978
Coil 7	1328	9569
Coil 8	506	9528
Coil 9	236	9416
Coil 10	450	6930

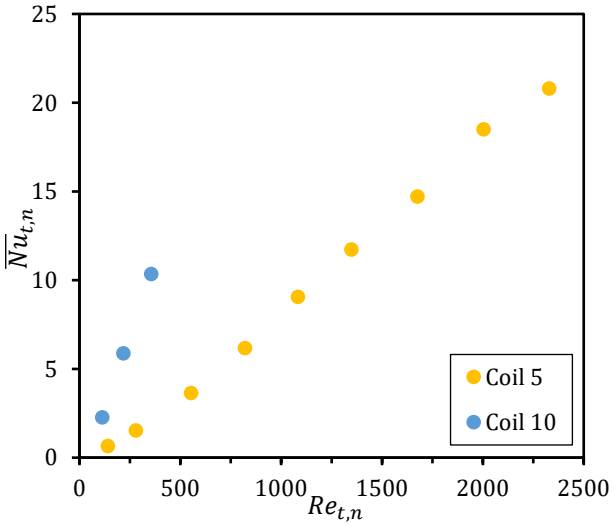

Figure 4-4. Dependence of $\overline{Nu}_{t,n}$ on l in two coils having the same $d_{t,i}$ and Cu but different l.

For straight pipes having both developing and developed flow regions (when $Re_{t,n}$ is low enough and/or the pipe is long enough), the slope of $\overline{Nu}_{t,n}$ vs. $Re_{t,n}$ is higher than when the flow is only developing (when $Re_{t,n}$ is high enough and/or the pipe is short enough). Since the thermal entry length increases with $Re_{t,n}$ (for straight pipes: $l_{th}/d_{t,i} \approx 0.05\, Re_{t,n}Pr_t$), [109] by increasing $Re_{t,n}$, the developing region increases at the expense of the developed region. Accordingly, a change in the slope of the $\overline{Nu}_{t,n}$ vs. $Re_{t,n}$ or a breaking point occurs when the thermal entry length approaches the pipe length because the dependence of $\overline{Nu}_{t,n}$ on $Re_{t,n}$ changes when the flow field changes. In other words, when $Re_{t,n} < Re_{t,BP}$, there are both developing and developed flow regions in the pipe, while at $Re_{t,n} > Re_{t,BP}$, the flow field is effectively developing. **Figure 4-5** represents this interpretation schematically. This interpretation supports the higher slope of the plot in **Figure 4-3** before BP, as the developed region which has higher convective resistance (lower $\overline{Nu}_{t,n}$) becomes shorter by increasing $Re_{t,n}$.

When the majority of the pipe is occupied by the developed flow region (at low values of $Re_{t,n}$), the $\overline{Nu}_{t,n}$ vs. $Re_{t,n}$ plot is concave up and the inflection point occurs once the developing region starts becoming dominant. According to **Figure 4-3-b**, the length of the S-shape region is slightly greater than Zone I. The BP can therefore be considered as a point at which the developed flow region is marginal, and developing flow effectively governs $\overline{Nu}_{t,n}$.

According to this explanation, the developing region completely occupies the pipe length at a value of $Re_{t,n}$ greater than but close to $Re_{t,BP}$.

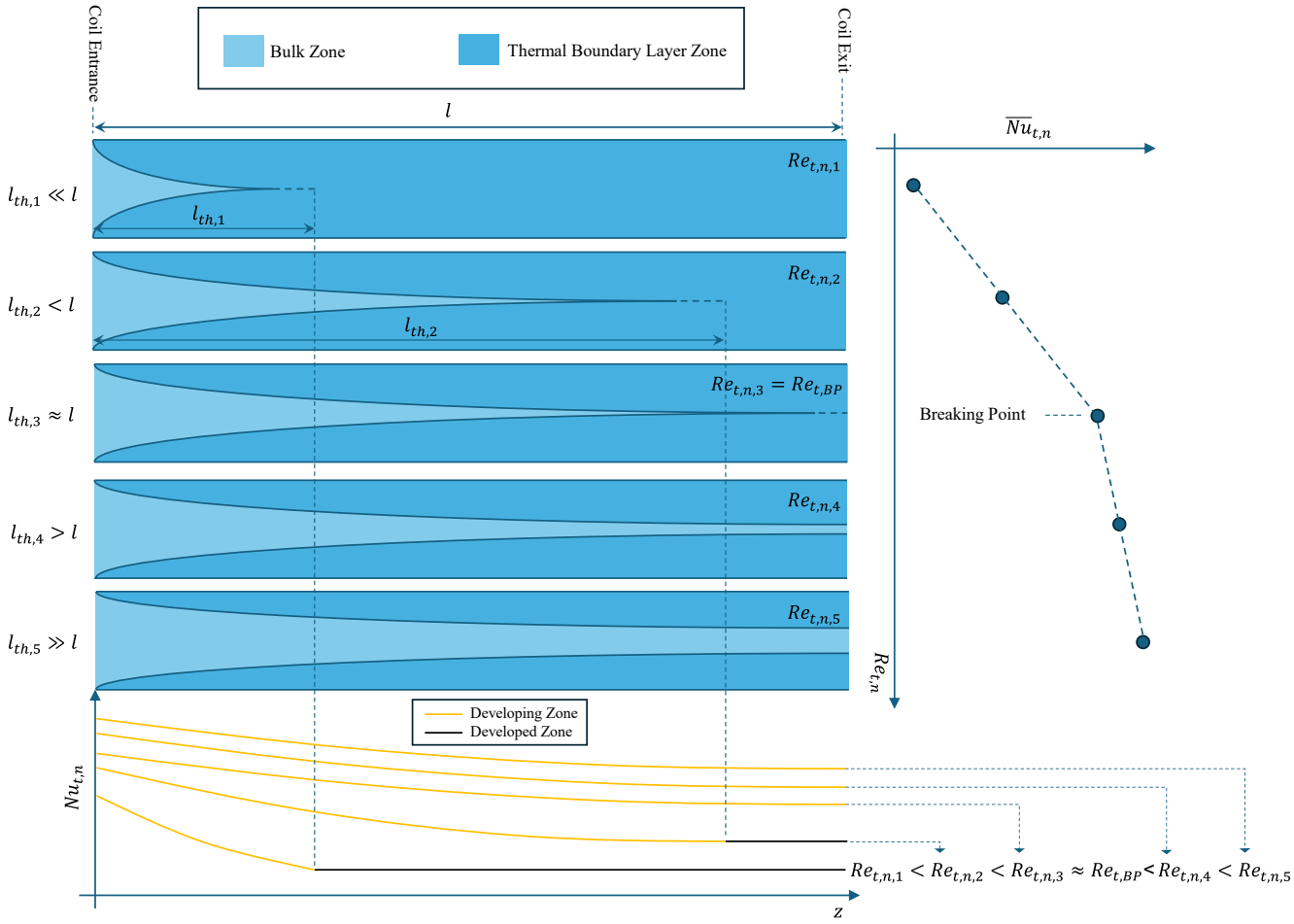

Figure 4-5. Occurrence of the breaking point due to the change in thermal flow field from a combined (developing and developed) field to a developing one. Subscripts 1–5 refer to different values of $Re_{t,n}$.

Figure 4-6 displays the variation of $\overline{Nu}_{t,n}$ vs. De_n for different coils before BP. As different coils provide different values of $\overline{Nu}_{t,n}$, it is clear that the impact of Cu and $Re_{t,n}$ must be correlated individually. Considering that the flow field before BP is a combination of developing and developed flow fields, it is expected that $\overline{Nu}_{t,n}$ exhibits dependence on the coil length.

Figure 4-7 normalizes $\overline{Nu}_{t,n}$ by $Le^{0.94}$ and causes data obtained from the different coil lengths to overlap. In addition, no significant dependence on Cu was observed in the majority of Zone I. This result agrees with a recent numerical study that shows Cu does not

considerably affect the average Nusselt number of a helical coil. [100] Considering that the trend of $\overline{Nu}_{t,n}$ is initially S-shape at the lower values of $Re_{t,n}$ and then becomes smooth concave down, the product of the error function and a power-law expression was selected to cover the full range of $Re_{t,n}$:

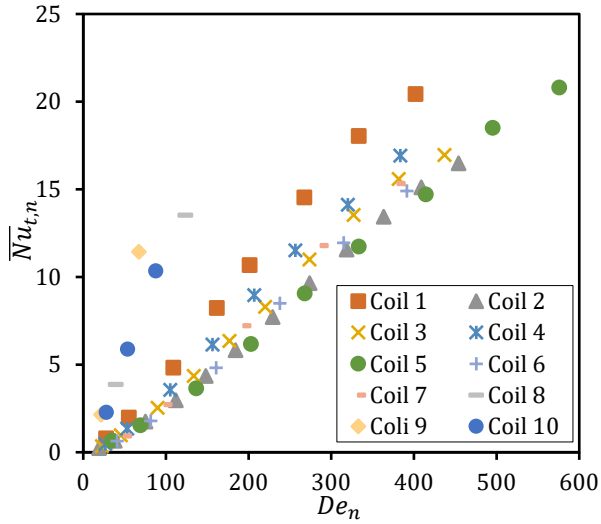

Figure 4-6. Comparison of $\overline{Nu}_{t,n}$–De_n profiles for different coils before BP.

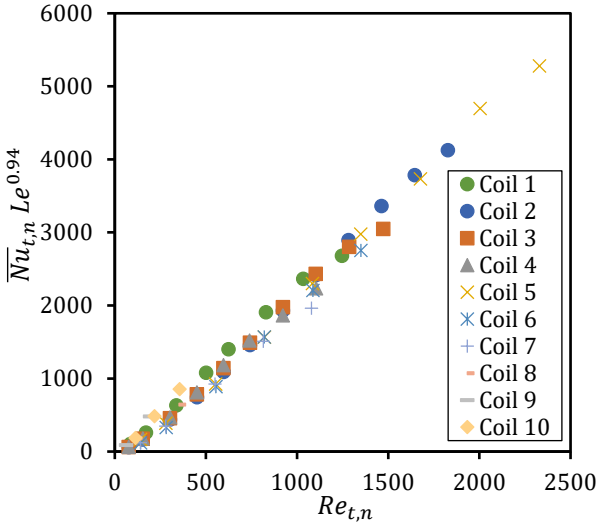

Figure 4-7. Normalization of $\overline{Nu}_{t,n}$ profiles before BP by Le.

$$\overline{Nu}_{t,n} = \alpha + \beta\, Re_{t,n}^{\gamma}\, Pr_t^{1/3} erf(\delta Re_{t,n}) \qquad (4\text{-}20)$$

where α represents the value of $\overline{Nu}_{t,n}$ when $Re_{t,n}$ approaches zero. Since the slope of the S-shape region in Equation (4-20) increases with increasing the constant δ, this will be correlated with the coil length. On the other hand, the dependence of $\overline{Nu}_{t,n}$ on Cu around and after BP appears in β as discussed in the following.

The dependence of $\overline{Nu}_{t,n}$ on Le diminishes when $Re_{t,n} > Re_{t,BP}$ as shown in **Figure 4-8** for Coils 4 and 9. Although the shorter Coil 9 exhibits greater values of $\overline{Nu}_{t,n}$ before BP (similar to Coils 5 vs. 10), it generates comparable values to the longer coil afterwards. This observation can be explained based on the flow regime before the coil entrance. All the entrances of the coils were connected to the water supply by a piece of straight pipe with the same inner diameter as the coils. When $Re_{t,n}$ < 2300, the flow in both the upstream straight pipe and following coil is laminar. When 2300 < $Re_{t,n}$< Re_{cr}, the flow in the upsteam straight

pipe is transitional showing turbulent features while the flow in the downstream coil seeks to laminarize. For the coils employed in this study, most of Zone II has then turbulent flow features in the upsteam straight pipe that are carried forth into the coil. Since the entry length in the turbulent flow is shorter, [109] $\overline{Nu}_{t,n}$ exhibits independence of Le after BP. These explanations agree with the trend of $\overline{Nu}_{t,n}$ around Re_{cr} where no change in the slope is observed. Relative to straight pipes, smaller difference between laminar and turbulent heat transfer rates as a consequence of secondary flows in curved pipes was also reported in the literature. [119]

Figure 4-9 compares $\overline{Nu}_{t,n}$ vs $Re_{t,n}$ plots obtained from Coils 2 and 4, which have different values of Cu. Although curvature increases Re_{cr}, [102,107] it can enhance turbulence by intensifying secondary flows and increase the heat transfer coefficient. As a result, β in Equation (4-20) is considered as a function of Cu.

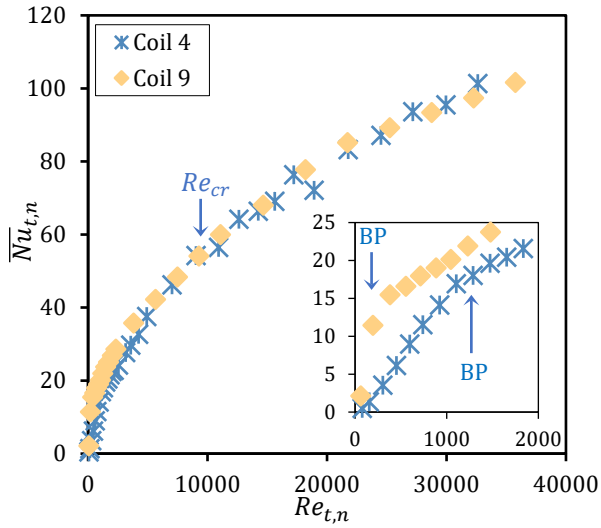

Figure 4-8. Comparison between $\overline{Nu}_{t,n} - Re_{t,n}$ profiles in the laminar and turbulent flow for Coils 4 and 9 which are different in l (the values of l for Coils 4 and 9 are 1.113 and 0.376 m, respectively).

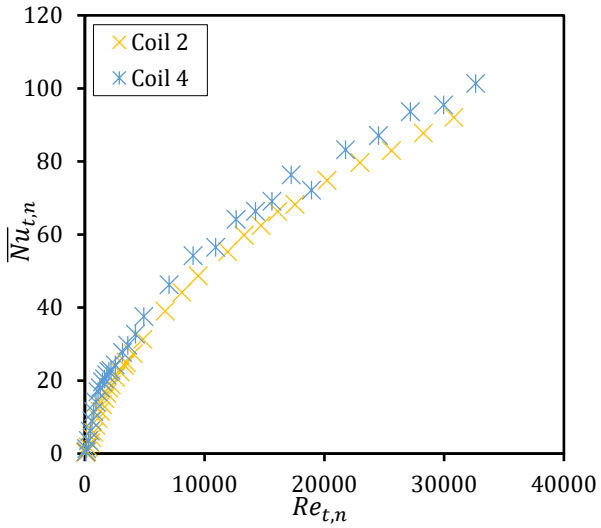

Figure 4-9. Effect of curvature on $\overline{Nu}_{t,n}$ (the values of Cu for Coils 2 and 4 are 0.062 and 0.121 respectively).

Equation (4-20) fits the data obtained from 10 coils with an R^2 = 0.995 which shows the consistency of the data and the accuracy of the model, as shown in **Figure 4-10**. The equation is a continuous function over the full range of $Re_{t,n}$, without errors inherent in piece-wise equations for domain boundaries. The constant 0.01 represents the value of $\overline{Nu}_{t,n}$ when $Re_{t,n}$

approaches zero which is equal to the value of the local Nusselt number ($Nu_{t,n}$) for the developed region at very low values of $Re_{t,n}$. Despite being reproducible, it being below a value of 1 requires further investigation.

$$\overline{Nu}_{t,n} = 0.01 + (0.81\,Cu + 0.38)Re_{t,n}^{0.46}Pr_t^{\frac{1}{3}}erf\left(\frac{0.17}{Le - 37.61}Re_{t,n}\right)$$
$$76 < Re_{t,n} < 36700 \qquad (4\text{-}21)$$
$$0.06 < Cu < 0.13$$
$$53 < Le < 362$$

The error function in Equation (4-21) represents the S-shape trend in the $\overline{Nu}_{t,n}$ plots. After the BP, this function approaches its asymptote such that the length of the developed region approaches zero. Physically, the developed region in a pipe is completely removed at a finite value of $Re_{t,n}$, while the error function predicts an infinity. To estimate l_{th}, $Re_{t,n}$ for different values of Le were determined by equating the error function term to 0.99 (the asymptotic value of the error function is unity). The results are shown in **Figure 4-11** and are correlated as follows:

$$\frac{l_{th}}{d_{t,i}} \approx 0.031\,Re_{t,BP}Pr_t + 27.06 \quad , \quad 53 < Le < 361 \qquad (4\text{-}22)$$

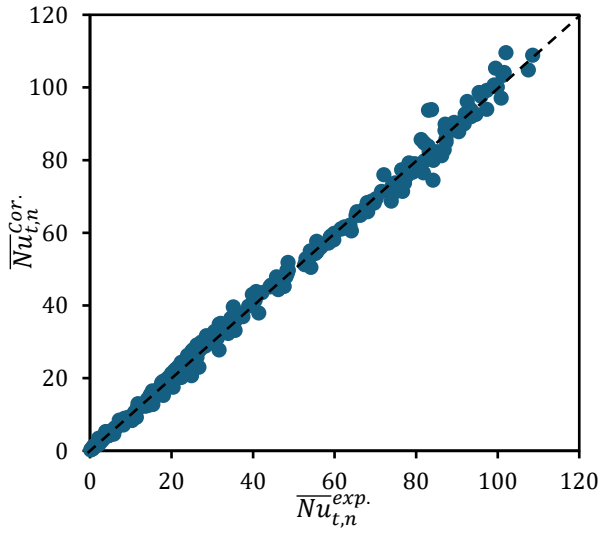

Figure 4-10. Correlated vs. experimental values of $\overline{Nu}_{t,n}$ for all the coils.

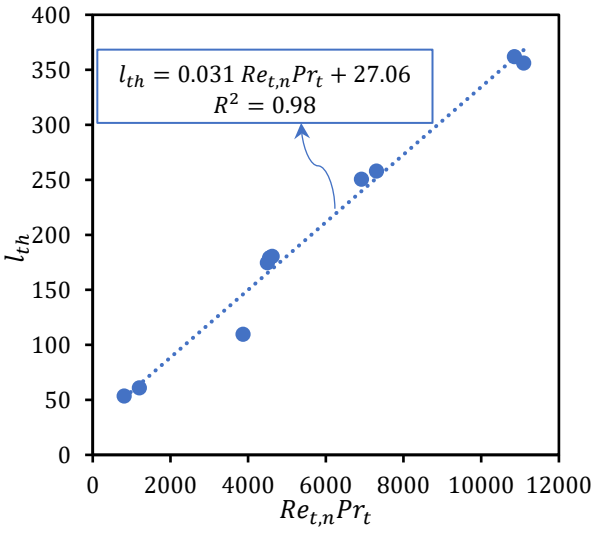

Figure 4-11. Estimated thermal entry length l_{th} using Equation (4-22).

This equation shows that l_{th} in helical coils is independent of Cu and shorter than for straight pipes. [60] The positive ordinate at the origin value results from the form of Equation (4-22) and suggest that l_{th} may become independent of flow conditions; this also warrants further investigation.

4.4.2. Oscillatory Flow

Figure 4-12-a shows the variation of $Nu_{t,o}$ vs. the oscillation amplitude (x) at $Re_{t,n}$ = 730 and different values of frequency (f). As this figure shows, $\overline{Nu}_{t,o}$ overall increases with increasing x, similar to what is observed when increasing the frequency (**Figure 4-12-b**). Nevertheless, it seems that, at high oscillation intensities (high values of x or f), the slope of increase in $\overline{Nu}_{t,o}$ decreases as can be seen for the plot at f = 6 Hz in **Figure 4-12-a**. Since the effects of x and f on $\overline{Nu}_{t,o}$ are similar, it is conventional in the literature that these quantities are lumped into a dimensionless group termed the oscillatory Reynolds number ($Re_{t,o}$) as a measure of oscillation intensity, [25,44,69,71,73–75,77,81] in which the velocity term in the net flow Reynolds number has been replaced with the maximum oscillatory velocity ($u_{o,max} = 2\pi f x$):

$$Re_{t,o} = \frac{2\pi f x \rho d_{t,i}}{\mu} \tag{4-23}$$

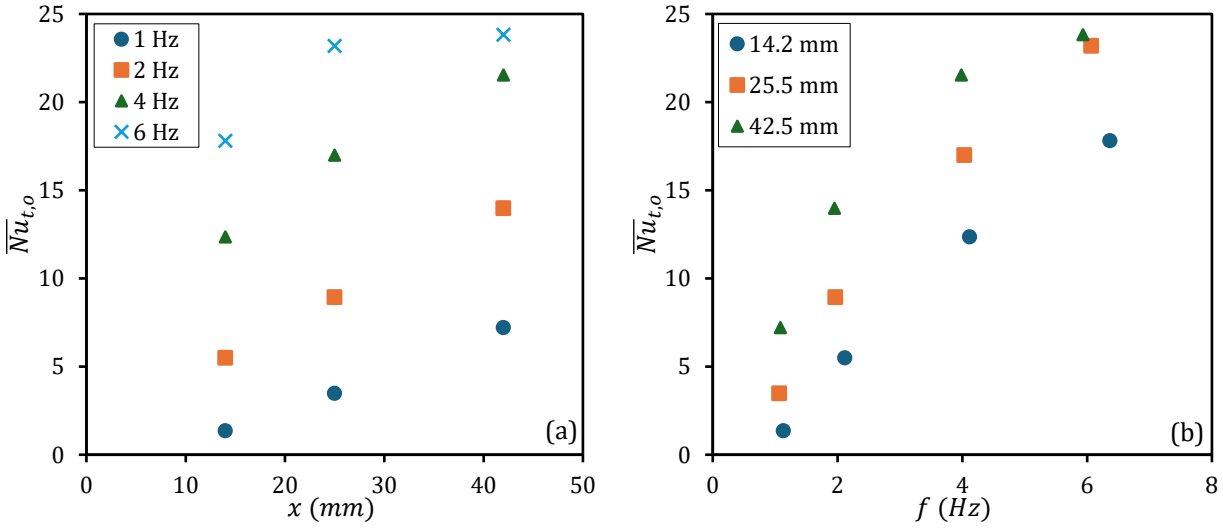

Figure 4-12. Variation of $\overline{Nu}_{t,o}$ vs. x and f at $Re_{t,n}$ = 730 for Coil 8.

Figure 4-13 displays the evolution of $\overline{Nu}_{t,o}$ as a function of $Re_{t,o}$ for two different sets of data points; f is variable and x is constant as well as vice versa. As both data sets are superimposed, this confirms the accuracy of $Re_{t,o}$ as a measure of oscillation intensity.

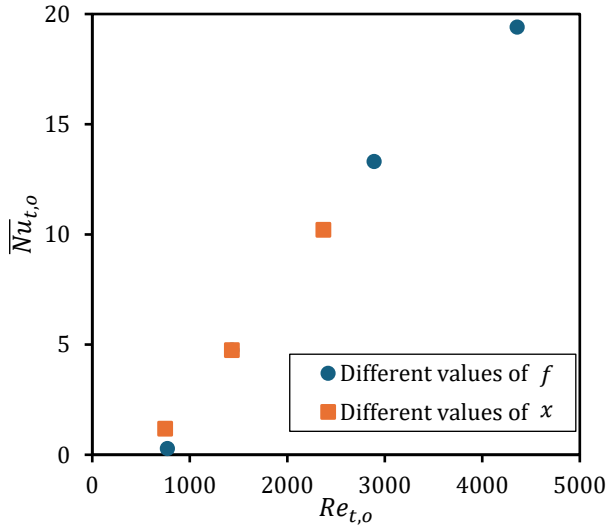

Figure 4-13. An example of the overlapping of $\overline{Nu}_{t,o}$ data points resulting from lumping x and f are into $Re_{t,o}$ for Coil 8 at $Re_{t,n}$ = 730.

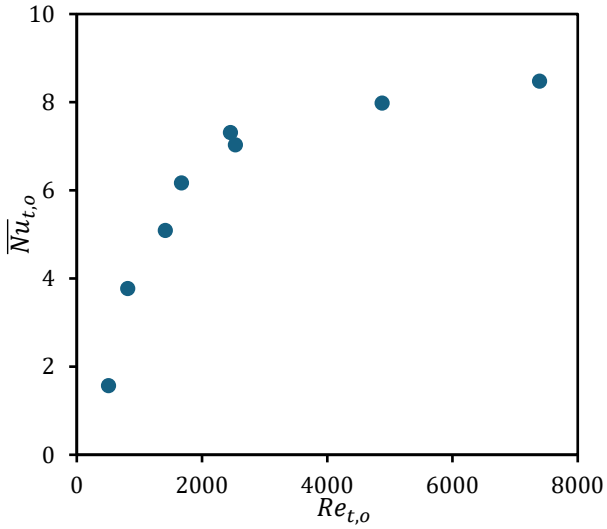

Figure 4-14. Variation of $\overline{Nu}_{t,o}$ vs. $Re_{t,o}$ for Coil 10 at $Re_{t,n}$ = 530.

Figure 4-14 shows the variation of $\overline{Nu}_{t,o}$ vs. $Re_{t,o}$ for Coil 10 at $Re_{t,n}$ = 530. As can also be deduced from **Figure 4-12-a**, at high oscillation intensities, $\overline{Nu}_{t,o}$ tends to approach a plateau, meaning that increasing the oscillation intensity can enhance the heat transfer coefficient up to a certain level (an asymptotic value) but further increases in oscillation intensity cannot effectively increase $\overline{Nu}_{t,o}$.

Although the increase in $Re_{t,o}$ can effectively increase $\overline{Nu}_{t,o}$, the amount of increase in $\overline{Nu}_{t,o}$ as well as the percentage enhancement ($\overline{Nu}_{t,o}/\overline{Nu}_{t,n} \times 100$) shows dependence on $Re_{t,n}$. **Figure 4-15** shows the effect of $Re_{t,n}$ on $\overline{Nu}_{t,o}$–$Re_{t,o}$ profiles for Coil 8. At very low values of $Re_{t,n}$, the oscillation cannot increase the $\overline{Nu}_{t,total}$ regardless of the oscillation intensity; therefore, $\overline{Nu}_{t,o} \approx 0$ according to Equation (4-18). It shows that there is a value of $Re_{t,n}$ below which the effect of oscillation on the heat transfer is marginal. By increasing $Re_{t,n}$, low values of $Re_{t,o}$ (low oscillation intensities) do not impact $\overline{Nu}_{t,total}$, meaning that $Re_{t,o}$ must be higher

than a threshold to affect $\overline{Nu}_{t,total}$so that $\overline{Nu}_{t,o}$ becomes sensible. As can be observed in **Figure 4-15**, $Re_{t,n}$ shifts the plots to the right while their behavior and slope are similar.

Figure 4-16 displays the evolution of percentage enhancement vs. $Re_{t,n}$ at different values of $Re_{t,o}$ for Coil 8. Even though the higher values of $Re_{t,o}$ lead to a higher percentage enhancement, by increasing $Re_{t,n}$, the percentage enhancement first begins to increase within a small range of $Re_{t,n}$ and then it decreases so that a maximum point is observed in the plots. From the maximum point onward, an increase in $Re_{t,n}$ leads to a decrease in $\overline{Nu}_{t,o}$ at a constant value of $Re_{t,o}$. Considering the relationship between $Re_{t,o}$ and $Re_{t,n}$ shown in **Figure 4-15** and **Figure 4-16**, $Re_{t,o}$ can be normalized by $Re_{t,n}$ in order to correlate $\overline{Nu}_{t,o}$ with the operating conditions. Dividing $Re_{t,o}$ by $Re_{t,n}^{1.8}$ led to very good data overlapping for the ascending parts of the plots as represented in **Figure 4-17**. However, there are still large differences between the plateaus at different values of $Re_{t,n}$. In the ascending parts of the plots, oscillation can considerably enhance the heat transfer coefficient by temporally decreasing the thickness of the near-wall viscous layer or intensifying turbulence / secondary flows. However, when the oscillation becomes stronger, the asymptotic value of $\overline{Nu}_{t,o}$ is overall governed by the net flow.

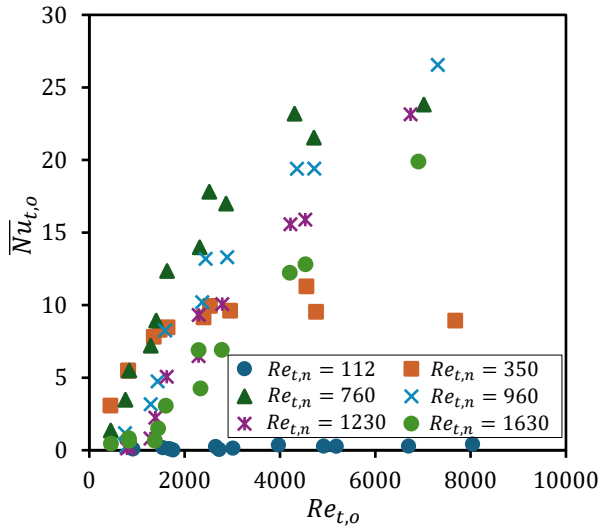

Figure 4-15. Comparison of $\overline{Nu}_{t,o}$–$Re_{t,o}$ profiles for Coil 8 at different values of $Re_{t,n}$.

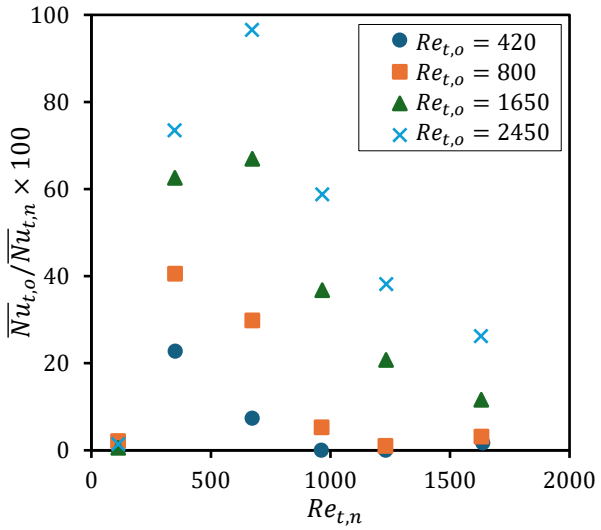

Figure 4-16. Effect of $Re_{t,n}$ on the percentage enhancement for Coil 8 at different values of $Re_{t,o}$.

In summary of the observation from **Figure 4-15**, **Figure 4-16**, and **Figure 4-17**, the enhancement of the convective heat transfer coefficient in a coil by oscillation is limited in four ways:

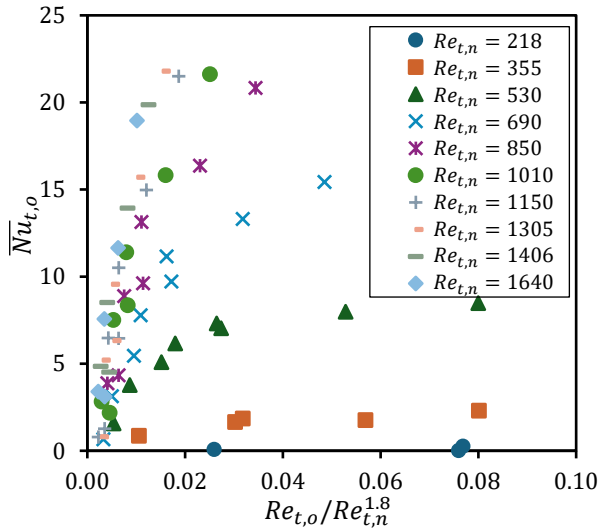

Figure 4-17. Persistent difference between the asymptotic values of $\overline{Nu}_{t,o}$ obtained from Coil 10 at different values of $Re_{t,n}$ after normalizing $Re_{t,o}$ with $Re_{t,n}^{1.8}$.

1- At low values of $Re_{t,n}$, the effect of oscillation on the heat transfer coefficient is marginal; e.g., at $Re_{t,n}$ = 112 in **Figure 4-15**.
2- By increasing $Re_{t,n}$, the threshold for the oscillation effectiveness increases, as shown in **Figure 4-15**.
3- When oscillation becomes strong compared to the net flow, further oscillation does not change $\overline{Nu}_{t,o}$ considerably, and it approaches an asymptotic value.
4- The asymptotic value is also dependent on the amount of $Re_{t,n}$, so that the larger the $Re_{t,n}$, the greater the asymptotic value.

The differences between the asymptotic values in **Figure 4-17** suggest that $\overline{Nu}_{t,o}$ needs extra normalization with $Re_{t,n}$ to minimize these differences. **Figure 4-18** shows the variation of $\overline{Nu}_{t,o}$ vs. $Re_{t,n}$ at $Re_{t,o} \approx 7400$ where all plots in **Figure 4-17** are plateaus. According to this figure, there is a relatively linear relationship between the asymptotic values and $Re_{t,n}$, meaning that $\overline{Nu}_{t,o}$ can be normalized by a linear expression in terms of $Re_{t,n}$ such as $n_1 Re_{t,n} + n_2$ in which n_1 and n_2 are constants and are determined by optimization. Including the Prandtl number in the analysis and normalizing $\overline{Nu}_{t,o}$ by $Re_{t,n}$, resulted in the trend

shown in **Figure 4-19** which was correlated by an exponential function having an asymptotic value with R^2 = 0.97:

$$\frac{\overline{Nu}_{t,o}}{n_1 Re_{t,n} + n_2} = 1.50\, exp\left(-\frac{1}{55.84\,\Psi}\right)$$
$$n_1 = 0.0327 \quad , \quad n_2 = -93.66\,Cu + 15.70 \quad , \quad \Psi = Pr_t^{1/3}\frac{Re_{t,o}}{Re_{t,n}^{1.82}} \tag{4-24}$$

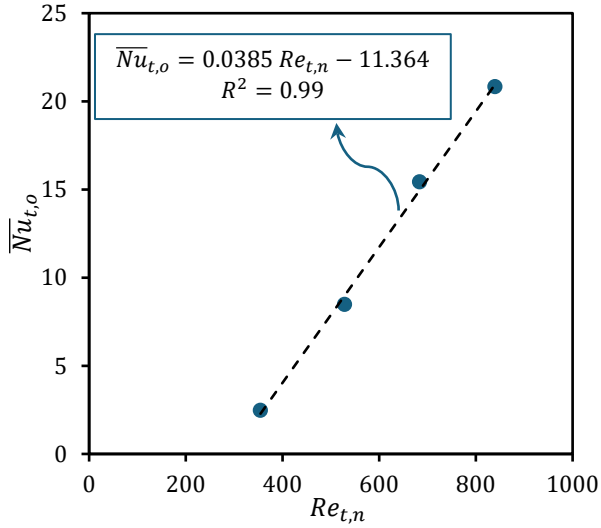

Figure 4-18. Linear relationship between asymptotic values of $\overline{Nu}_{t,o}$ and $Re_{t,n}$ at $Re_{t,o} \approx$ 7400.

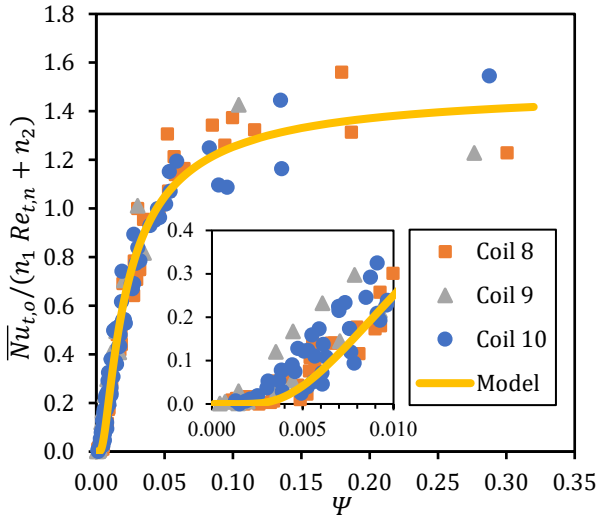

Figure 4-19. Comparison of normalized oscillatory data points and the correlation (Equation (4-24)).

Based on the trend shown in **Figure 4-19**, when 0.005 < Ψ < 0.075, applying oscillation is expected to considerably impact the heat transfer coefficient. For Ψ > 0.075, the effect of oscillation gradually decreases and approaches an asymptotic value. The value $\Psi \approx 0.003$ is the threshold of the oscillation effectiveness, below which applying oscillation does not enhance the heat transfer. Equation (4-24) can be used to determine the oscillatory term of Equation (4-18), and the other term is calculated by Equation (4-21). There are two important points related to Equation (4-24). The presence of n_2 is necessary as the plot in **Figure 4-18** does not pass through the origin of coordinates. The x-intercept of the line in **Figure 4-18** (or overall, the value of $-n_2/n_1$) is an estimation of the $Re_{t,n}$ value below which the oscillation does not considerably impact the heat transfer coefficient. The other point is that the oscillatory data did not show dependence on the tube length; this is likely because

the dependence on the length was included in the $\overline{Nu}_{t,n}$ and heat transfer enhancement by oscillation occurs over a short length (twice the oscillation amplitude).

4.5. Conclusion

The present study tried to prepare a comprehensive quantitative basis for heat transfer calculations in non-oscillatory and oscillatory helical coils, capable of being employed in the design of oscillatory flow coil reactors. Non-oscillatory heat transfer measurements were performed, and the data were processed using the LMTD method and an accurate method of estimating the jacket-side heat transfer resistance. The average Nusselt number vs. Reynolds number profiles showed an S-shape trend at low Reynolds numbers, followed by a smooth trend, so that a repeatable breaking point was observed in all the profiles around the end of the S-shape region. Based on the concept of flow development in pipes, the S-shape region was recognized as the range of the Reynolds number over which the thermally developed region in a helical coil is totally removed and the breaking point was considered as a sign that the thermal entry length approaches the tube length. The experimental data showed that the dependence of the average Nusselt number on coil dimensions before and after the breaking point is different. Before the breaking point, the average Nusselt number is inversely proportional to the coil dimensionless length and approximately independent of the relative curvature. After the breaking point, the average Nusselt number was directly proportional to relative curvature, but it was approximately independent of the coil's dimensionless length, especially at high Reynolds numbers. A continuous function including a power-law expression and the error function was suggested to correlate the S-shape and smooth region of the average Nusselt number profiles for a full range of the Reynolds number. The constants of this function were also correlated with the coil geometry. A correlation for the thermal entry length in helical coils was suggested by equating the error function term to 0.99.

Applying sinusoidal oscillation to selected coils while flowing a net flow through them led overall to an increase in the heat transfer coefficient. The effects of oscillation amplitude and frequency were similar, so that when both increased, the heat transfer coefficient also increased. However, an asymptotic value at high oscillation intensities was observed for every net Reynolds number, meaning that increasing oscillation can enhance the heat transfer coefficient up to a certain level, and further increase in oscillation does not impact

it. Some other limitations related to the net flow Reynolds number were also observed. First, increasing the net flow Reynolds number increases the threshold for the oscillation effectiveness. Second, the effect of oscillation on heat transfer at low Reynolds numbers was marginal. Third, the asymptotic value at high oscillation intensities was governed by the net Reynolds number. These limitations led to further data normalization and a more accurate correlation for the average oscillatory Nusselt number.

Nomenclature

Latin Letters

a	-	model parameter
A	m^2	heat transfer area
$A_{t,i}$	m^2	tube inner surface area
b	-	model parameter
c	-	model parameter
$C_{p,m}$	$kJ \cdot kg^{-1} \cdot K^{-1}$	tube-side fluid heat capacity at film temperature
Cu	-	relative curvature
d	-	model parameter
$\overline{D}_c$	m	coil mean diameter
$\overline{D}_{c,corr}$	m	coil corrected mean diameter
$D_{c,i}$	m	coil inner diameter
$D_{c,o}$	m	coil outer diameter
De_n	-	net flow Dean number
$D_{j,i}$	m	jacket's inner diameter
$d_{t,i}$	m	tube inner diameter
$d_{t,o}$	m	tube outer diameter
e	-	model parameter
f	Hz	oscillation frequency
h_j	$W \cdot m^{-2} \cdot K^{-1}$	jacket-side average convective heat transfer coefficient
h_t	$W \cdot m^{-2} \cdot K^{-1}$	tube-side average convective heat transfer coefficient
k_{Al}	$W \cdot m^{-1} \cdot K^{-1}$	aluminum thermal conductivity
$k_{f,j}$	$W \cdot m^{-1} \cdot K^{-1}$	jacket-side fluid thermal conductivity
$k_{f,t}$	$W \cdot m^{-1} \cdot K^{-1}$	tube-side fluid thermal conductivity
l	m	tube length
l_{th}	m	thermal entry length
m	$m^{1-b} \cdot s^{-1}$	model parameter
$\dot{m}$	$kg \cdot s^{-1}$	mass flow rate
N_t	-	coil number of turns
$\overline{Nu}_j$	-	jacket-side average Nusselt number
$Nu_{t,n}$	-	tube-side local net flow Nusselt number
$\overline{Nu}_{t,n}$	-	tube-side average net flow Nusselt number
$\overline{Nu}_{t,o}$	-	tube-side average oscillatory Nusselt number
$\overline{Nu}_{t,total}$	-	tube-side average total Nusselt number
n_1	-	model parameter
n_2	-	model parameter
Pr_j	-	jacket-side Prandtl number
Pr_t	-	tube-side Prandtl number
P_t	m	tube pitch
$\dot{Q}$	W	rate of heat transfer
R_{Conv}	$m^2 \cdot K \cdot W^{-1}$	convective heat transfer resistance
Re_j	-	jacket-side Reynolds number
$Re_{t,BP}$	-	net flow Reynolds number at breaking point
$Re_{t,n}$	-	tube-side net flow Reynolds number

$Re_{t,o}$	-	tube-side oscillatory Reynolds number
R^2	-	correlation coefficient
$T_{f,j}$	°C	jacket-side film temperature
$T_{f,t}$	°C	tube-side film temperature
$T_{j,i}$	°C	jacket temperature at top of coil
$T_{j,o}$	°C	jacket temperature at bottom of coil
$\bar{T}_{s,i}$	°C	tube inner surface average temperature
$\bar{T}_{s,o}$	°C	tube outer surface average temperature
$T_{t,o}$	°C	tube inlet temperature
$T_{t,i}$	°C	tube outlet temperature
U	$W \cdot m^{-2} \cdot K^{-1}$	overall heat transfer coefficient
$u_{o,max}$	$m \cdot s^{-1}$	maximum oscillation velocity
x	m	oscillation amplitude
z	m	axial coordinate of tube

Greek Letters

α	-	model parameter
β	-	model parameter
γ	-	model parameter
δ	-	model parameter
μ_j	Pa·s	jacket-side fluid viscosity
ρ_j	$kg \cdot m^{-3}$	jacket-side fluid density
Ψ	-	dimensionless group

Abbreviations

BP	breaking point
CPVC	chlorinated polyvinylchloride
DC	direct current
GPM	gallon per minute
LMTD	logarithmic mean temperature difference
NPT	national pipe thread
rpm	revolutions per minute

Solid Forming

5.1. Introduction

Traditional pharmaceutical and fine chemical production processes possess a high degree of flexibility because batch or semi-batch stirred tank reactors are primarily utilized, which aren't often allocated to any specific reaction or product; instead, they are flexible to produce different chemicals via various reactions at a wide range of operating conditions. [1–3] This flexibility is associated with some problems, such as lower heat transfer performance, reduced mixing quality, and fouling. [4–7] Reducing the problems associated with traditional pharmaceutical processes is included in the concept of "Process Intensification," which refers to methods and modifications implemented in a process to enhance its efficiency and economy, such as reducing equipment volume, handling chemical reactions at more severe conditions, decreasing energy consumption, and reducing waste materials. [8–10]

Migration from batch to continuous flow reactors is a common method of intensifying solid-forming processes, especially when the production volume is low and a continuous flow reactor is needed to control the product quality. [19] From the process intensification point of view, a continuous flow microreactor has a high surface-to-volume ratio that can improve heat transfer and diminish transport lengths. [11,12]

One of the continuous flow reactors used for both research and industrial purposes is the helical coil reactor. Simple structure, low cost, and availability are advantages of this reactor. Compared to other types of continuous flow microreactors, a helical coil improves the quality of mixing because the tube curvature, as a simple method of passive mixing, improves the radial mixing in the reaction medium by dissipating the flow kinetic energy and generating secondary flows without a need for inserts and/or contraction of the flow path. [21] However, passive mixing in microreactors may not be sufficient at low flow rates. Therefore, a method of active mixing such as vibration, [120–122] pulsation, [123] and oscillation [44,101] using an external source of energy may be employed to compensate for the lack of proper mixing, enhance transport coefficients, and render the quality of mixing independent of the fluid velocity (and space time for a given reactor volume). [21]

Applying oscillation to a continuous helical coil reactor can improve macromixing by flattening the axial velocity profile and narrowing the residence time distribution. [101]

Oscillation can also increase the plug flow performance in continuous baffled reactors by generating longitudinal vortices in interbaffle zones. [23,46] Micromixing characteristics are also influenced by oscillation when it generates secondary flows in the reaction medium. [25] Since the micromixing quality affects the selectivity of reactions in a reaction medium, [55] it can be an important factor in controlling the crystallization performance of solid-forming reactions. [62] Solid properties such as particle size distribution (PSD) can be more precisely controlled in microreactors as there is greater control over macromixing and micromixing conditions, heat and mass transfer, and particle nucleation/growth. [20,63]

Plain mm-scale helical coils may have lower risk of solids plugging than reactors with internals, but their small diameter along with low fluid velocities can still lead to fouling and ultimately blocking caused by particle aggregation. Some strategies that lower the chance of plugging in microreactors are the use of dispersant agents, ultrasound, buffer fluid flow to avoid direct contact with the wall, and periodic purges. [63–65] In addition, producing particles with a narrow PSD is favored because the number of large particle aggregates decreases, leading to a lower risk of plugging. [39]

In this study, sinusoidal oscillation is applied to a helical coil reactor producing solid particles to experimentally investigate the effects of the operating conditions (net flow rate, oscillation frequency and amplitude) on the particle size distribution. The results obtained from the oscillatory experiments are compared to the non-oscillatory conditions to evaluate the efficiency of oscillation for control of the particle size distribution. The solid-forming reaction is the fast precipitation reaction between sodium carbonate and magnesium sulfate, which was selected based on a toolbox approach developed by Plouffe et al. [7] Finally, since oscillation provides additional periodic shear at the tube wall, its effect on the amount of fouling relative to the absence of oscillation is qualitatively studied.

5.2. Experimental

5.2.1. Materials

The fast precipitation reaction between sodium carbonate (Na_2CO_3) and magnesium sulfate ($MgSO_4$) in the aqueous medium was selected to produce solid magnesium carbonate ($MgCO_3$) at 25 °C:

$$Na_2CO_3\ (aq) + MgSO_4(aq) \rightarrow MgCO_3(s) + Na_2SO_4(aq) \quad (5\text{-}1)$$

Solutions of Na_2CO_3 and $MgSO_4$ (ACP Chemicals, 98% purity) were prepared using demineralized water at different concentrations (0.025 to 0.5 M) and first reacted in batch to determine a concentration (and associated kinetics, PSD) that would then be favorable for continuous flow in the coil. Since the solid particles agglomerate relatively fast, the outlet stream of the coil reactor is directly sent to a flow-through quartz cuvette inserted in a zetasizer to measure the particle size distribution in-line. As the concentration of solid particles must be very low for particle size analysis, reagent concentrations of 0.05 M were found to allow the zetasizer to smoothly operate without stream dilution. Considering the k_{sp} of $MgCO_3$ at 25 °C (0.0139 g per 100 g of water), [124] around 95% of the $MgCO_3$ is precipitated in the form of solid particles in the aqueous medium at an initial concentration of 0.05 M.

5.2.2. Experimental Setup

Solid forming reactions were performed using an experimental setup whose flow diagram is shown in **Figure 5-1**. This setup consists of a vessel as the reactor jacket made of CPVC (a piece of 6" NPT double flanged pipe with a schedule of 80 and a height of 1.1 m), a heating/refrigerated bath circulator (Huber Ministat 230), a magnetic drive pump (Laing SM-1212-STW-26) having a stainless steel impeller and casing connected to a mixing nozzle (Orifice diameter = 3/16 ", circulation rate = 36.8 gpm at 50 psi) in the jacket to increase the jacket-side heat transfer, two syringe pumps (SyrDos, Hitec Zang) capable of continuously injecting fluids for flow rates up to 150 ml·min^{-1}, an oscillator (explained in the following), and two valve assemblies made of stainless steel at the entrance and exit of the installed coil. The oscillator comprised a glass syringe with a proper capacity (1/2.5/10 ml) connected to a reciprocating rod actuated by a high-torque variable-speed DC gear motor (E-S motor, maximum rotational speed = 666 rpm, maximum voltage = 24 V, maximum power = 120 W). The inlet valve assembly was to adjust the operating modes (non-oscillatory / oscillatory), deaerate the oscillator, and wash the reactor at the end of each experiment. The outlet valve assembly was used to lead part of the product to the particle size measurement loop, and measure the coil pressure drop by a differential pressure transmitter (Omega PX409-

250DWUV, 0–17.5 barg) connected to a data acquisition system (National Instrument, NI-9203 installed on NI-cDAQ-9171 chassis).

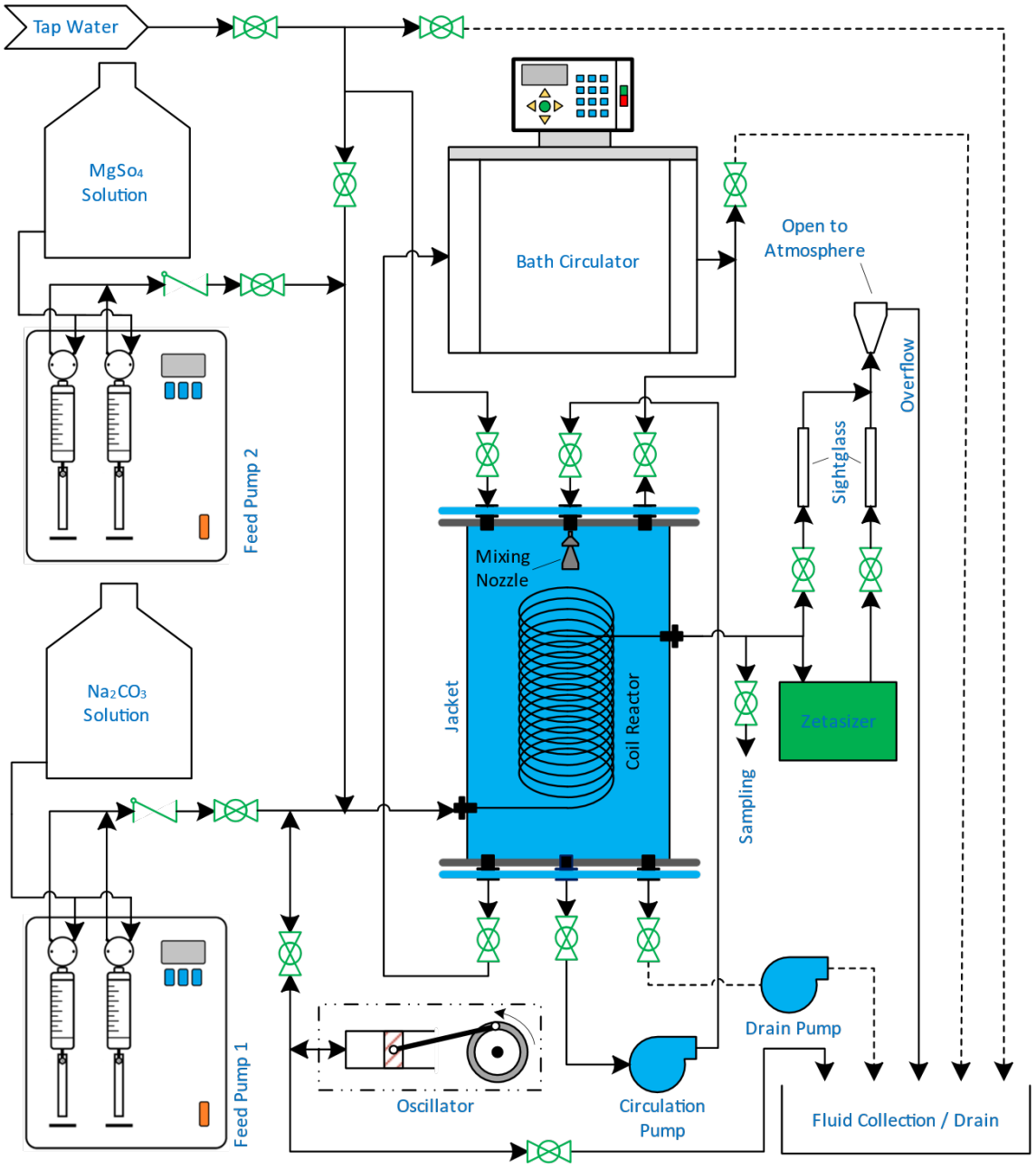

Figure 5-1. Process flow diagram of the experimental setup.

The particle size measurement loop received part of the product from the reactor exit and sent it to a flow-through quartz cell inserted in a zetasizer (Malvern Nano ZS, ZEN 3600) capable of measuring the particle size distribution of flow streams. The flow through cell

(**Figure 5-2**) was a type of screw-lid quartz cell whose lid had been replaced by a home-made two-way cap to customize it for a flow-through application. The two sight glasses allowed for visual inspection of the flow and adjustment of the flow rate through the quartz cell.

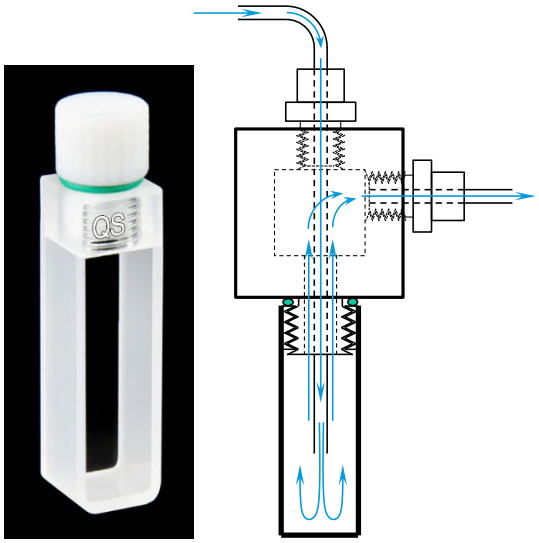

Figure 5-2. Flow-through quartz cell used to measure the particle size online.

Four temperature sensors (PT-1000, Omega PR-10L-4-1000-1/8-4) connected to a data acquisition system (Moxa ioLogik E-2260) were used to measure coil entrance and exit temperatures and the jacket top and bottom temperatures to make sure reactions were performed at a constant temperature. A cylindrical overflow container (ID = 5 cm) was installed at the outlet stream to minimize pressure fluctuations at oscillatory conditions.

A piece of PTFE tube with a length of 8 m, tube inner and outer diameters of 6.35 and 9.5 mm, wound tightly around a piece of PVC pipe with an outer diameter of 42 mm at a tube pitch of 1.25 tube OD, was used as a helical coil reactor with 48 turns to perform solid forming reactions under both non-oscillatory and oscillatory conditions. To eliminate any perturbation at the entrance and exit of the coil and reduce the pressure drop, its inlet and outlet in the jacket were tangent to the circumference of the coils.

After inserting the coil into the jacket, the jacket was filled with water. Then the jacket temperature was adjusted at 25±0.1°C by the circulator. Once the jacket temperature reached a steady state, the circulation pump was started, and then the setup was ready to perform experiments.

5.2.3. Procedure

To run a non-oscillatory experiment, the flow rate of each syringe pump was set at an identical value between 10 and 60 mL·min^{-1} (the net flow rate was between 20 and 120 mL·min^{-1}), then they were started. When twice the space time at the set flow rate passed, the particle size was analyzed in situ at the outlet of the reactor. Following a non-oscillatory experiment, a set of oscillatory experiments at different values of frequency (1–6 Hz) and amplitude (4–11.9 mm) was performed. After setting the frequency and amplitude to certain values, the position of the valve between the oscillator and the coil inlet was changed to open, and the oscillator was started. After approximately twice the residence time, the particle size started being measured until a steady-state value for last three measurements was reached (average value ± 10 %). Then, the last three measurements were recorded.

For the operability study, two non-oscillatory and oscillatory experiments were done at an elevated (10X) concentration of 0.5 M to evaluate the effect of oscillation on the extent of fouling by continuously monitoring the coil pressure drop.

5.2.4. Data analysis

According to the principle of dynamic light scattering, the scattering intensity is proportional to the sixth power of the particle size. Therefore, to identify agglomeration in the reaction medium, intensity distributions are compared. On the other hand, Z_{ave} (intensity weighted harmonic mean particle size) is used as the mean particle size instead of the intensity mean particle size because this quantity is mathematically stable and insensitive to noise. [125] Since PSDs in this study are generally multimodal, their variance (σ^2), instead of the polydispersity index, will be compared.

5.3. Results and Discussion

5.3.1. Non-oscillatory experiments

Figure 5-3 shows the evolution of Z_{ave} vs. the total flow rate in the absence of oscillation. The population Z_{ave} monotonically decreases to a relatively constant value with increasing flow rate. After nucleation, particles grow by absorbing solids formed in the reaction medium and can agglomerate/merge with other particles via mechanisms such as attraction between

adjacent particles and collision between particles with enough momentum. A longer residence time favors particle growth via absorption of solids.

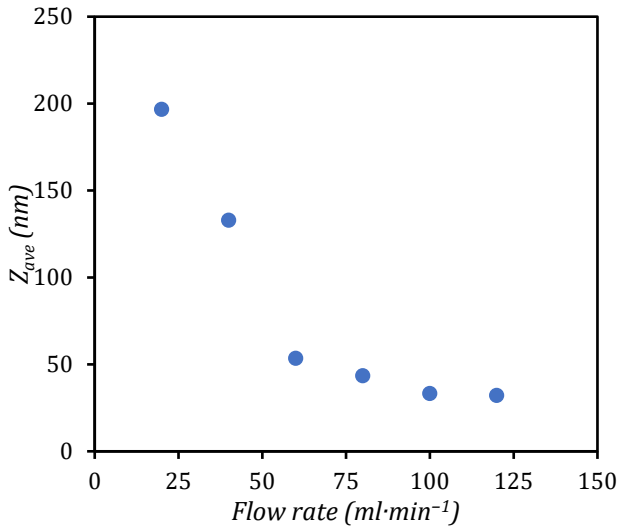

Figure 5-3. Mean particle size vs. the net flow rate for the non-oscillatory experiments.

According to the model provided by Smoluchowski, [126] the number of collisions in a medium containing solid particles is expressed as:

$$N_{c,ij} = f(\dot{\gamma})\, N_{p,i} N_{p,j} \left[d_{p,i} + d_{p,j}\right]^3 \tag{5-2}$$

where $N_{c,ij}$ is the number of collisions between particles of size classes i ($d_{p,i}$) and j ($d_{p,j}$), and $N_{p,i}$, $N_{p,j}$ are their number of particles. $f(\dot{\gamma})$ is the proportionality constant that depends on the shear rate ($\dot{\gamma}$). Since particle collision can lead to agglomeration, breakage, or no change, it is expected that different particle sizes will be obtained for different flow rates. The evolution of the particle size with flow rate shown in **Figure 5-3** is thus a combined effect of the changes in the residence time and number/intensity of collisions, where the asymptotic value implies that an equilibrium between the various factors is reached.

Figure 5-4 shows three PSDs obtained from the experiments shown in **Figure 5-3**. All the distributions have two distinct peaks whose modes are very different. The first peak represents the great majority of the number of particles and shows that these do not considerably grow after nucleation, although they grow more uniformly. The second peak then represents the particles mainly formed by agglomeration. There are two observations

when increasing the flow rate. First, the modes of the peaks shift to lower values leading to a decrease in the population mean particle size. Second, the peak of the smaller particles diminishes whereas the peak of the larger particles diminishes and broadens, which supports the fact that a higher flow rate leads to a shorter residence and growth time as well as an increase in the number and intensity of collisions by increasing the local shear rate.

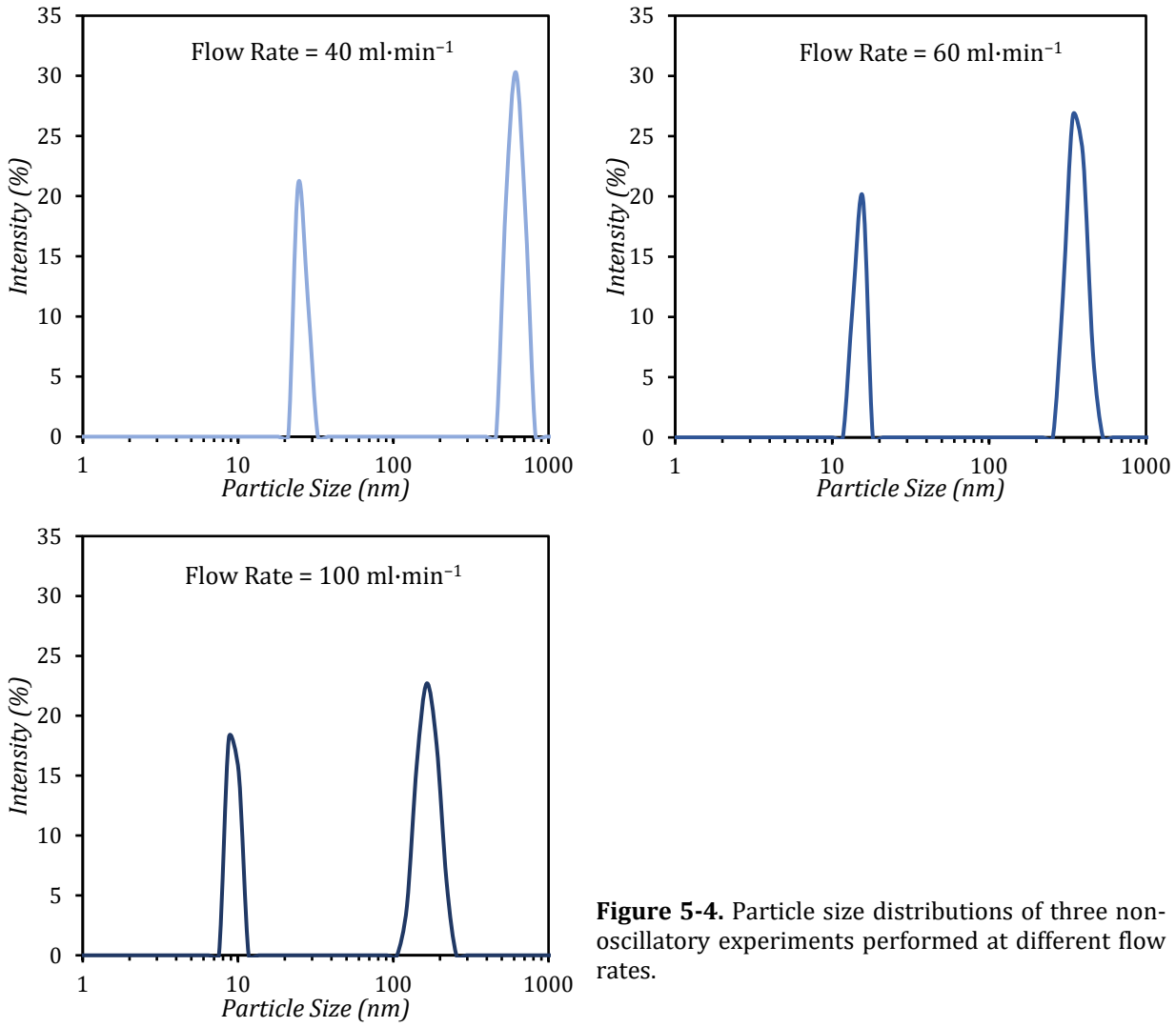

Figure 5-4. Particle size distributions of three non-oscillatory experiments performed at different flow rates.

Figure 5-5 shows that σ^2 decreases by increasing the flow rate. Regardless of what factor is dominant in particle growth, an increase in the flow rate (which is proportional to an increase in the plug flow performance) leads to a narrower PSD because the ratio of axial to radial mixing decreases at higher axial velocity.

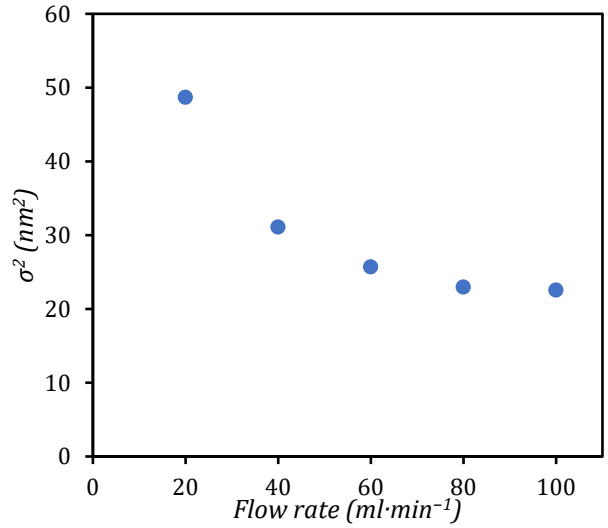

Figure 5-5. Evolution of the PSD broadness vs. flow rate for the non-oscillatory experiments.

5.3.2. Oscillatory Experiments

Figure 5-6 presents the change in Z_{ave} by increasing the oscillation frequency for the experiments at an amplitude of 7.2 mm and a net flow rate of 40 ml·min^{-1}. By increasing the frequency, the mean particle size initially increases and then decreases such that a maximum appears. When sinusoidal oscillation is applied to a flow, the shear rate, which is the derivative of the axial velocity radial profile with respect to the radial distance, has a cosinusoidal profile and depends similarly on the oscillation frequency and amplitude.

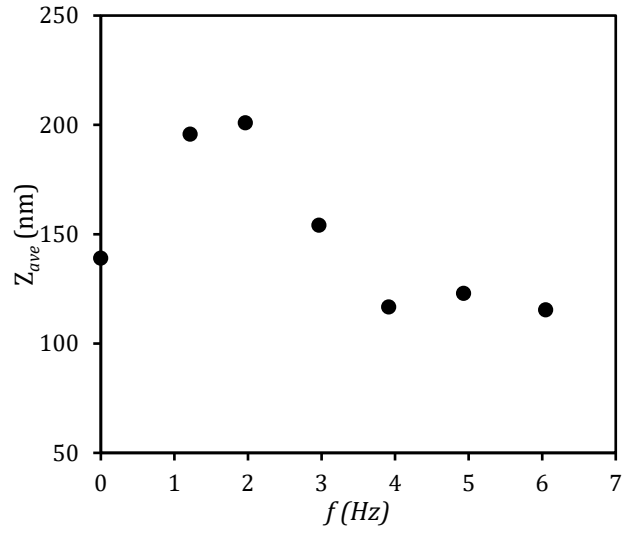

Figure 5-6. Evolution of the mean particle size vs. the oscillation frequency at an amplitude of 7.2 mm and a flow rate of 40 ml·min^{-1}.

According to the Smoluchowski model, by increasing the frequency, the shear rate as well as the number of collisions increases, leading initially to an increase in the mean particle size. Further increase in the frequency increases the momentum of the particles and causes them

to break or not to merge when colliding. At high frequencies, the mean particle size becomes approximately constant, meaning that the factors increasing and decreasing the mean particle size are balanced.

PSDs can provide a better picture of what happens to the particles when increasing the frequency. **Figure 5-7** compares the PSDs obtained from three experiments shown in **Figure 5-6** at f = 0, 2 and 4 Hz which correspond to the non-oscillatory experiment, the oscillatory experiments at and after the peak in **Figure 5-6**, respectively. In the non-oscillatory

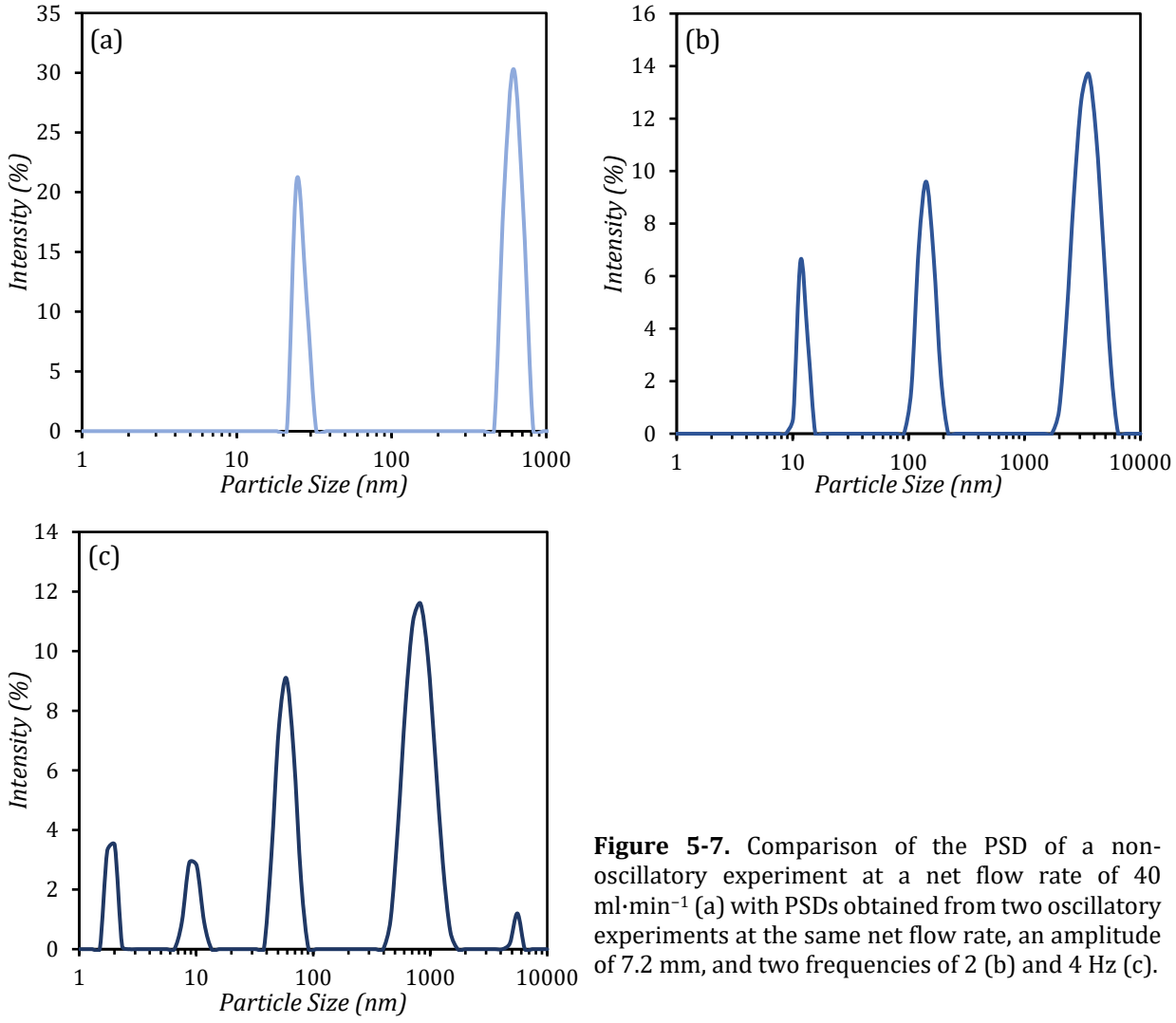

Figure 5-7. Comparison of the PSD of a non-oscillatory experiment at a net flow rate of 40 ml·min^{-1} (a) with PSDs obtained from two oscillatory experiments at the same net flow rate, an amplitude of 7.2 mm, and two frequencies of 2 (b) and 4 Hz (c).

experiment (**Figure 5-7-a**), the PSD possesses 2 peaks, which represent the smaller relatively uniformly grown particles and larger agglomerated ones. By applying oscillation, another peak appears in the middle of the initial peaks (**Figure 5-7-b**) which represents

moderately grown particles and/or intermediate agglomerated particles, and overall increases the mean particle size. **Figure 5-7-c** confirms that at high frequencies (f = 4 Hz and greater) oscillation causes particle breakage or prevents particles from growing sufficiently. An increase in the number of peaks implies that particle breakage occurs at high frequencies, while the appearance of a peak with a small mode is a sign of particles that have not considerably grown.

Figure 5-8 shows the mean particle size profiles vs. the oscillation frequency at an amplitude of 7.2 mm and different net flow rates. The effect of the net flow rate on the mean particle size in the presence of oscillation is similar to the non-oscillatory experiment, where an increase in the flow rate decreases the mean particle size. However, by increasing the frequency, the effect of the net flow rate decreases as the mean particle sizes become more similar. On the other hand, by increasing the net flow rate, the maximum particle size occurs at a lower frequency (shifts to the left), and the amount of particle growth due to oscillation decreases. Accordingly, by increasing one of the net flow rate and oscillation frequency in the investigated ranges, the effect of the other one on Z_{ave} diminishes.

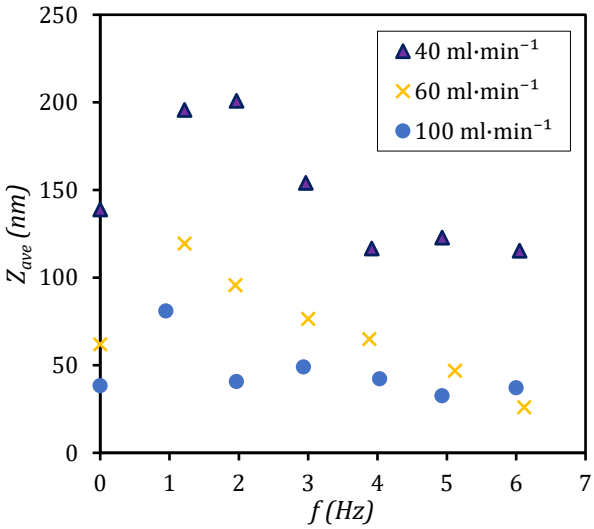

Figure 5-8. Comparison of the mean particle size vs. frequency at an amplitude of 7.2 mm and different net flow rates.

Figure 5-9 shows how changes in the oscillation amplitude affect the mean particle size at different net flow rates. At the lower net flow rate, an increase in the amplitude leads to a higher mean particle size. At the mid net flow rate, the effect of increasing the amplitude is marginal, suggesting that there is a flow rate at which the mean particle size is nearly

independent of the amplitude. At the higher flow rate, the mean particle size decreases with increasing the amplitude.

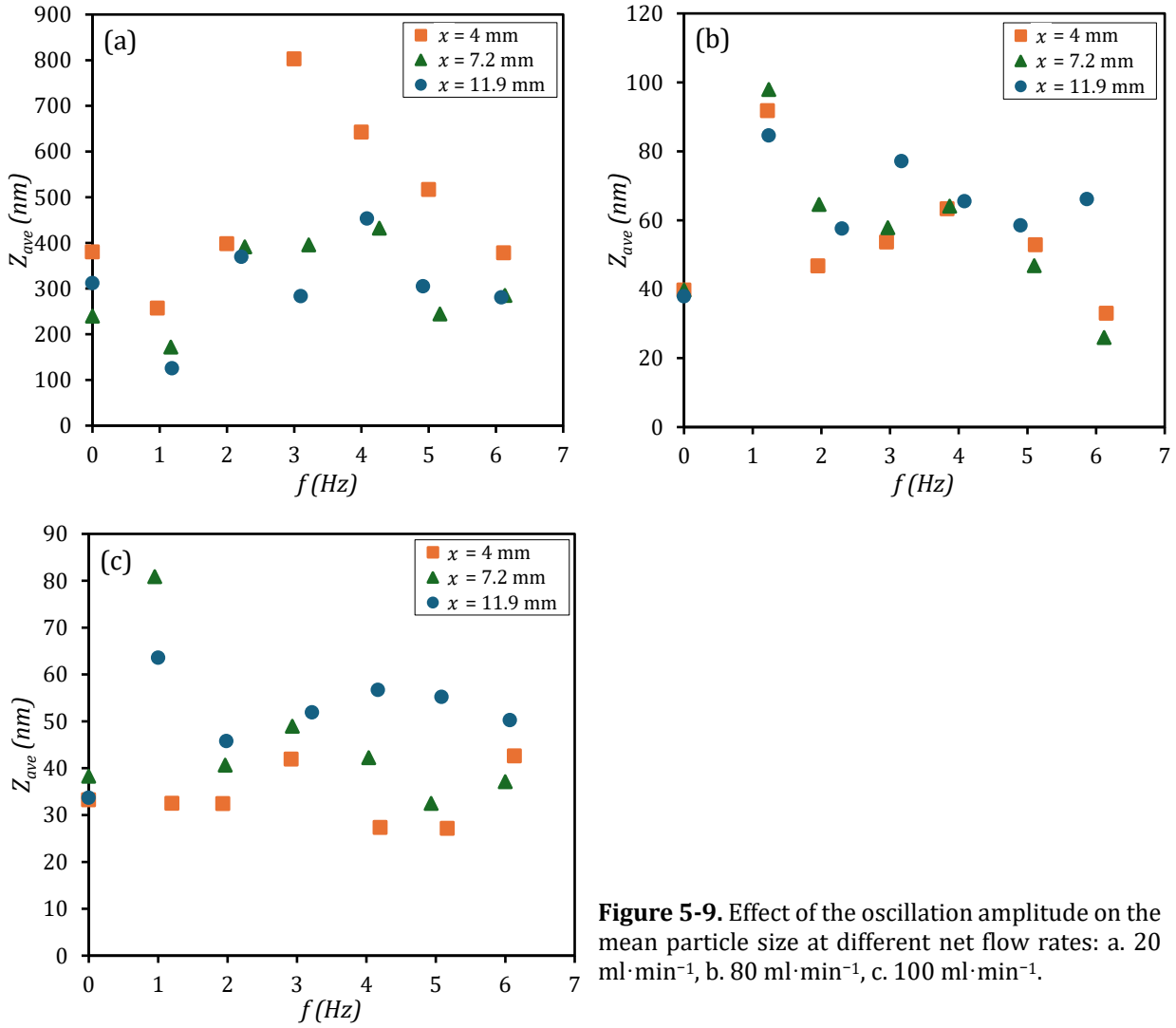

Figure 5-9. Effect of the oscillation amplitude on the mean particle size at different net flow rates: a. 20 ml·min^{-1}, b. 80 ml·min^{-1}, c. 100 ml·min^{-1}.

When the oscillation amplitude is increased, the shear rate as well as the number of collisions increases when the oscillator pushes the fluid forward because the net and oscillatory flows have the same direction. By increasing the amplitude at the lower flow rate, the collisions lead to an increase in the mean particle size. But this effect diminishes when increasing the net flow rate and finally becomes inverse because the high momentum of the particles leads to particle breakage or prevents them from growing. Nonetheless, increasing the oscillation amplitude does not change the particle size as strongly as the oscillation frequency and net flow rate.

5.3.2.1. PSD Broadness

Figure 5-10 shows the variance of the PSDs as a measure of their broadness versus the mean particle size for all the experiments performed. Regardless of the small effect of increasing the oscillation amplitude, the broadness profiles at different amplitudes overlap and become minimum in a similar range of the particle size. The broadness of the PSDs appears to be a strong function of the mean particle size, while according to the Smoluchowski model, the number of particles which is a function of the operating conditions, is a determining factor in the number of collisions and consequently, the PSD broadness. Similar σ^2 vs. Z_{ave} have been obtained at different operating conditions. Since in fast precipitation reactions, the solid content (or the total volume of particles) in the reaction medium is constant and the number of particles is inversely proportional to the mean particle size. As a result, the broadness of PSDs can be expressed by the mean particle size, which is affected by the operating conditions, especially the net flow rate and frequency, as shown before.

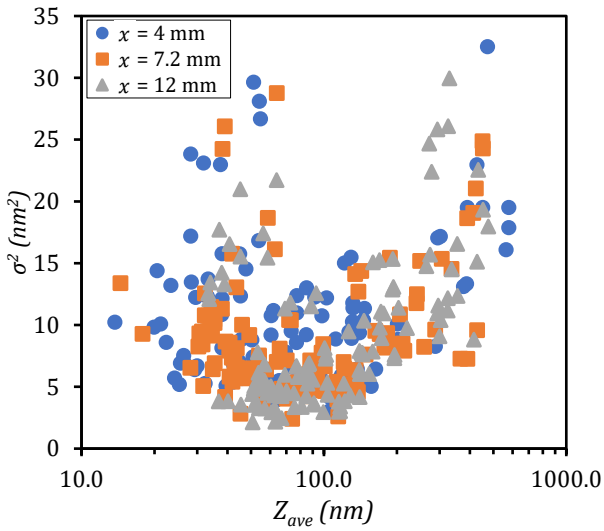

Figure 5-10. Variation of the PSD broadness vs. the mean particle size for all the experiments performed.

5.3.2.2. Data Correlation

A basis for correlating the particle-related measurements obtained from oscillatory flow coil reactors is provided here for future studies aiming to overlap the data and better understand the relation and interactions between the measured particle sizes and the operating conditions.

The frequency and amplitude showed different effectiveness in affecting the resulting mean particle size; therefore, they will be considered individually in the following dimensionless groups:

$$Wo = \frac{d_{t,i}}{2}\sqrt{\frac{2\pi f\rho}{\mu}} \tag{5-3}$$

$$St = \frac{d_{t,i}}{4\pi x} \tag{5-4}$$

Where Wo is the Womersley number, $d_{t,i}$ is the tube inner diameter, f is the oscillation frequency, ρ is the fluid density, and μ is the fluid viscosity. In the Strouhal number (St), x represents the oscillation amplitude. The net flow rate is also included in the net flow Reynolds number:

$$Re_n = \frac{\rho\, u\, d_{t,i}}{\mu} \tag{5-5}$$

Where u is the net flow velocity. **Figure 5-11** shows satisfactory data overlapping when Wo is normalized by Re_n. As the amplitude is not as effective as the frequency, the exponent of St is quite low. When the normalized oscillation intensity $\Psi = Wo\, St^{0.2}/Re_n$ is less than 0.1, the mean particle size does not change considerably relative to the non-oscillatory experiments (Ψ = 0). However, by increasing Ψ, oscillation appears to be more effective so that a maximum is observed in the number of particles, representing maximum particle growth.

By comparing **Figure 5-10** with **Figure 5-11**, it is revealed that for the purpose of producing larger particles (e.g., Z_{ave} = 500 nm) by oscillation, both the mean particle size and PSD broadness cannot be controlled simultaneously because the minimum in **Figure 5-10** cannot coincide with the maximum in **Figure 5-11**. Nonetheless, it is possible to choose ranges for the operating conditions so that both the mean and variance of the particle size distribution are in satisfactory range.

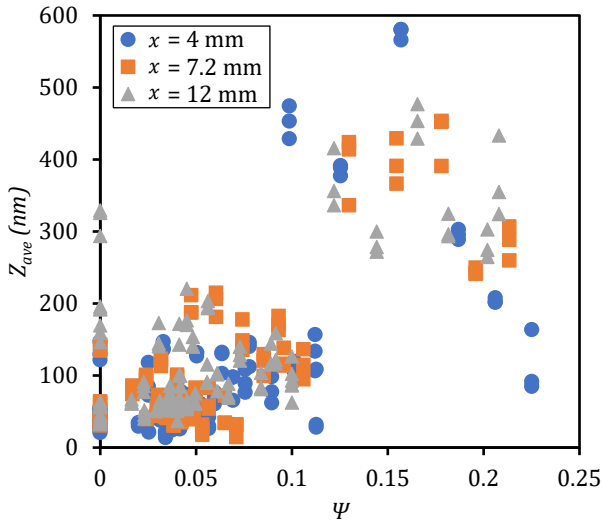

Figure 5-11. Evolution of the mean particle size with increasing the normalized oscillation intensity for all the experiments performed.

5.3.3. Operability Test

Figure 5-12 represents the time evolution of the coil pressure drop for a non-oscillatory and oscillatory experiment performed at a more elevated concentration of 0.5 M for each reagent. The oscillation amplitude and frequency for the latter were 7.2 mm and 3 Hz, respectively. After 80 minutes of operation in the non-oscillatory experiment, the pressure drop begins to rise, and several peaks are observed in the continuation of the experiment, meaning that partial blocking is temporarily removed by the flow. Nonetheless, the height of the peaks increases up to a defined value at which the controller software stops the feed pumps to prevent them from being damaged as the reactor is almost plugged.

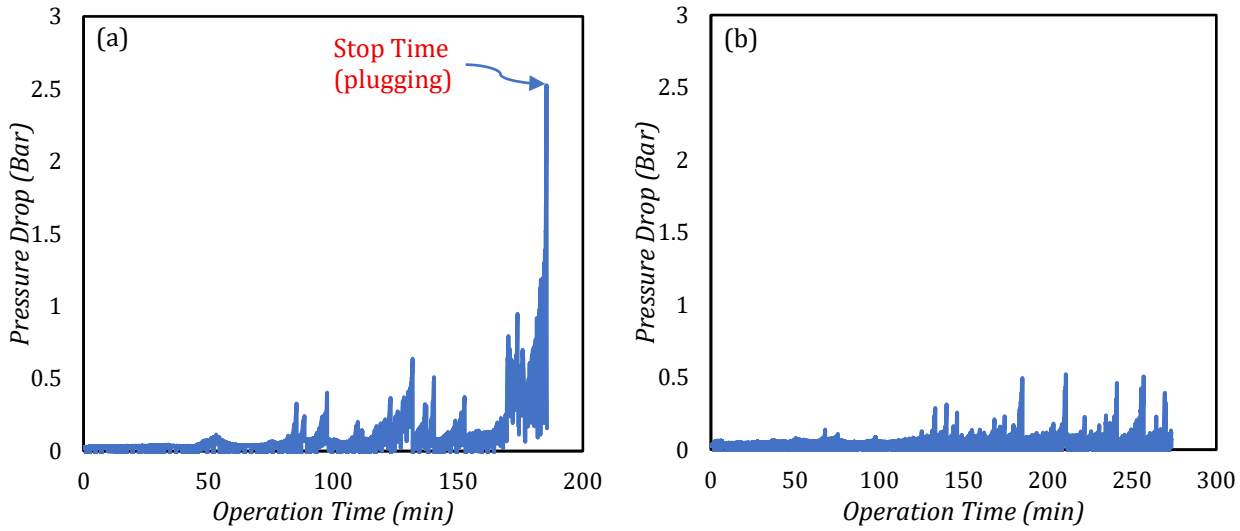

Figure 5-12. Time evolution of the coil pressure drop during two experiments at an elevated concentration of 0.5 m for each reagent. (a) a non-oscillatory experiment at a net flow rate of 40 ml·min^{-1} (b) an oscillatory experiment at the same net flow rate, a frequency of 3Hz and amplitude of 7.2 mm.

Figure 5-12 displays how applying oscillation controls the coil pressure drop during the non-oscillatory experiment and helps long-term operations. Although in the presence of oscillation peaks are repeated, oscillation can maintain the pressure drop at a minimum level for a longer time, thereby decreasing the number of stops in a long-term operation.

5.4. Conclusion

In this study, oscillation was applied to a helical coil reactor producing solid particles of magnesium carbonate from the fast precipitation reaction between sodium carbonate and magnesium sulfate to control the particle size distribution mean and variance compared to non-oscillatory experiments. The mean particle size in non-oscillatory experiments was inversely proportional to the net flow rate, while the PSD became narrower when increasing the net flow rate. In oscillatory experiments, the net flow rate had the same impact as for non-oscillatory conditions, and the frequency appeared stronger than the amplitude in affecting the particle size. The mean particle size displayed a maximum in a range of frequency, suggesting the maximum particle growth. However, this maximum diminished by increasing the net flow rate. In addition, a range of the net flow rate was identified in which an increase in the oscillation amplitude did not considerably affect the mean particle size. Before this range of net flow rate, an increase in the amplitude caused particle growth, but vice versa after it. The mean particle size in the reaction medium was also correlated with the operating conditions lumped into dimensionless groups (net flow Reynolds number, Womersley number, and Strouhal number) and displayed a maximum in a range of the operating conditions. Finally, operability tests showed that applying oscillation can maintain the reactor pressure drop at a minimum level and decrease the number of stops caused by blocking.

Nomenclature

Latin Letters

$d_{p,i}$	nm	particle diameter of size class i
$d_{t,i}$	m	tube inner diameter
f	Hz	oscillation frequency
$N_{c,ij}$	-	number of collisions between particles of size classes i and j
$N_{p,i}$	m^{-3}	number of particles of size classes i
Re_n	-	net flow Reynolds number
St	-	Strouhal number
u	$m \cdot s^{-1}$	net flow velocity
Wo	-	Womersley number
x	m	oscillation amplitude
Z_{ave}	nm	intensity weighted harmonic mean particle size

Greek Letters

$\dot{\gamma}$	s^{-1}	shear rate
μ	Pa·s	fluid viscosity
ρ	$kg \cdot m^{-3}$	fluid density
σ^2	nm^2	PSD variance
Ψ	-	normalized oscillation intensity

Abbreviations

ID	inner diameter
NPT	national pipe thread
OD	outer diameter
PSD	Particle size distribution

Conclusions and Future Research

6.1. How Effective Is Oscillation?

The overall objective of this thesis was to better intensify baffleless coil reactors by applying sinusoidal oscillation as an active mixing method combined with the tube curvature as a passive mixing technique, aiming to improve the quality of mixing and fluid-to-wall heat transfer so that a coil reactor can handle solid-forming reactions. The literature review provided in Chapter 1 justified the importance of this topic, explained the detailed objective of this research, and prepared a basis for calculations and analysis in the next chapters.

In Chapter 2, macromixing behavior of a coil reactor under non-oscillatory and oscillatory conditions was analyzed by experimentally studying the residence time distribution. The results show that applying oscillation to a coil overall improves the plug flow performance (decreases the RTD variance) compared to non-oscillatory flow. Nonetheless, there are ranges of operating conditions for the oscillatory flow in which the plug flow performance is maximum. By originally defining the oscillation amplitude as the characteristic length in the oscillatory Dean number and using a statistical model, a comprehensive correlation including full coil geometry and the operating conditions was suggested to predict the residence time distribution for a coil reactor under oscillatory conditions.

In Chapter 3, the phase angle between the pressure drop and velocity profiles and the viscous power dissipation for an oscillatory flow coil reactor were determined using CFD and a simplified method derived from the mechanical energy balance. The comparison between these two methods showed that the simplified model can provide a good estimate for the viscous power dissipation and phase shift in oscillatory flow coil reactors without a need for an unsteady friction factor or CFD simulation. In addition, the RTD variance normalized by the power dissipation vs. the total Reynolds number attained a monotonic trend, allowing for the estimation of the viscous power dissipation by estimating the RTD variance from the correlation provided in Chapter 2.

Chapter 4 addressed the detailed experimental analysis of heat transfer in coil reactors with wide ranges of operating conditions and coil geometry under non-oscillatory and oscillatory conditions. Results obtained from non-oscillatory flow experiments displayed a clear thermal entry effect, which cannot be ignored in heat transfer calculations. This study led to a

comprehensive correlation for the average Nusselt number in coils as a function of operating conditions and coil geometry lumped into dimensionless groups. This correlation was developed for the full range of the Reynolds number and can well estimate the thermal entry length in coils. Applying oscillation resulted in interesting achievements in oscillatory flow heat transfer. To enhance the heat transfer coefficient, the oscillation intensity normalized by the net flow Reynolds number must be adjusted between two limits. For oscillation intensities less than the lower limit, no enhancement in the heat transfer coefficient was observed, and for ones greater than the upper limit, the amount of enhancement tends to approach an asymptotic value. The results from this part also resulted in a correlation to predict the heat transfer coefficient under oscillatory conditions.

In Chapter 5, a sample fast precipitation reaction was selected and handled in a coil reactor to evaluate its performance of coil reactors in continuous solid production. The evolution of the particle size distribution at the reactor exit was monitored online by changing the non-oscillatory and oscillatory operating conditions. A dimensional analysis showed that the mean particle size is maximized in a range of the oscillation intensity normalized by the net flow Reynolds number, suggesting the maximum particle growth. On the other hand, the PSD variance was a strong function of the mean particle size and displayed a minimum regardless of the operating conditions. Applying oscillation can also facilitate long-term operations by decreasing the risk of blocking.

According to the achievements in this research, applying oscillation can provide ranges of operating conditions in which the plug flow performance, convective heat transfer coefficient, particle growth, and PSD broadness are optimized. Selecting proper operating conditions in those ranges can lead to better intensification of a coil reactor in terms of decreasing the reactor size, optimizing energy consumption, and improving the product quality. The important point is that these ranges are mostly independent, and for quantities related to solid forming reactions, they are case-specific, meaning that it is not feasible to choose operating conditions and coil dimensions at which all the aforementioned quantities are optimum. Therefore, to design a reactor for a specific solid-forming reaction, a trade-off must be established between different design parameters such that more important quantities are in acceptable ranges.

6.2. Recommendations for Future Studies

In Chapter 2, a correlation was proposed to predict RTD of coil reactors under oscillatory conditions. This correlation was developed based on two sets of data points obtained from coils with similar tube inner diameters. It is recommended to test a wider range of the tube inner diameter to verify the parameters of this empirical model. Additionally, this correlation mathematically gives a limiting value for the RTD variance when the oscillation intensity is equal to zero. However, this limiting value is independent of the net flow Reynolds number. For future studies, an upgrade in this correlation is recommended so that a coil RTD is predicted for non-oscillatory conditions.

Although the use of the steady-flow friction factor provided a good estimate of viscous power dissipation in Chapter 3, developing a model to estimate the unsteady flow friction factor as a function of oscillatory flow operating conditions using experiments and CFD modeling is recommended.

In Chapter 4, the thermal entry length of coil reactors appeared to be important in heat transfer analysis, and its trend predicted that this quantity tends to be independent of flow conditions when the Reynolds number approaches zero. In addition, the value of the average Nusselt number in the coil was less than the theoretical value at low Reynolds numbers. A numerical and experimental study is recommended to verify the thermal entry length data points, recognize its trend at very low Reynolds numbers, and study conduction and advection's contributions to heat transfer at low Reynolds numbers. For the oscillatory flow heat transfer, further investigation is required to reveal why the extent of heat transfer enhancement in oscillatory flow, which is essentially non-steady, is dependent on the net flow Reynolds number. The upper and lower limits of the oscillation intensity can also be verified using CFD modeling.

The solid-forming reaction selected in Chapter 5 was a fast precipitation reaction with a relatively low reaction enthalpy. Therefore, the solid content along the reactor was constant so that the majority of the reactor length was employed to grow solid particles, and there was not a need for substantial heat removal. Future studies can also focus on slower reactions/solid forming processes in which the solid content increases along the reactor

length and also on reactions with a high reaction enthalpy, in order to investigate the heat transfer and solid formation together. The experiments performed in Chapter 5 were performed at a very low concentration of the reagent to directly pass the exit flow through an online particle size analyzer. Experiments with concentrated reagents are recommended for future studies to study the interaction between particles in the particle growth process. For this purpose, a sampling/dilution system at the outlet is required to condition samples before analysis.

Appendices

Appendix A: Procedure for determining F-curve and its associated E-curve (RTD)

Appendix B: Algorithm for constructing an RTD using operating conditions and reactor dimensions

Appendix A: Procedure for determining F-curve and its associated E-curve (RTD)

Two aqueous fluids were selected to apply negative/positive step changes in the electrical conductivity of the feed to the reactor: deionized water with a conductivity near zero, and 0.05% w/w NaCl solution with a conductivity around 950 µS/cm at 25°C. A negative/positive step change is applied in the electrical conductivity of the feed to the reactor and the time evolution of the conductivity of the outlet stream is logged continuously. The response to the fluid step change yields the cumulative residence time distribution (F-curve), while the associated E-curve (RTD) is obtained by the differentiation of the F-curve as is shown in **Figure A1**. [47] Times $t_{min}$and t_{max} are when the conductivity starts to change and reaches steady state within measurement error (0.05 %), respectively. The minimum measured conductivity (K_{min}) is equal to the conductivity of the deionized water and is subtracted from all conductivity data for normalization, whereas K_{max} is the maximum measured conductivity.

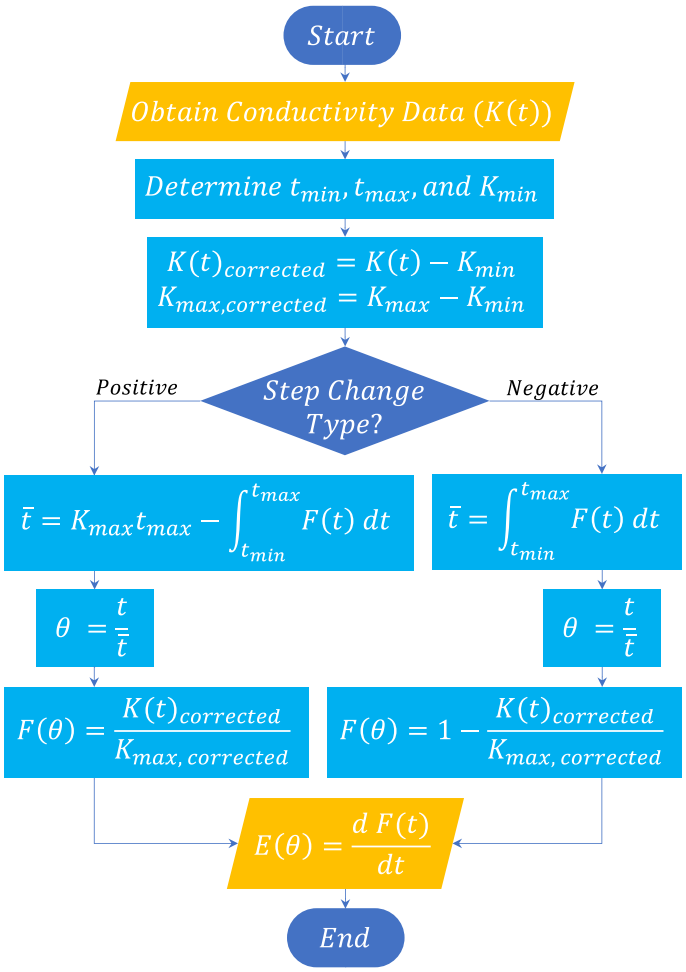

Figure A1. Procedure to determine F-curve and its associated E-curve (RTD). [47]

Appendix B: Algorithm for constructing an RTD using operating conditions and reactor dimensions

Based on the correlations provided in the article, the overall algorithm to build an RTD using the coil dimensions and operating conditions is provided in **Figure A2**.

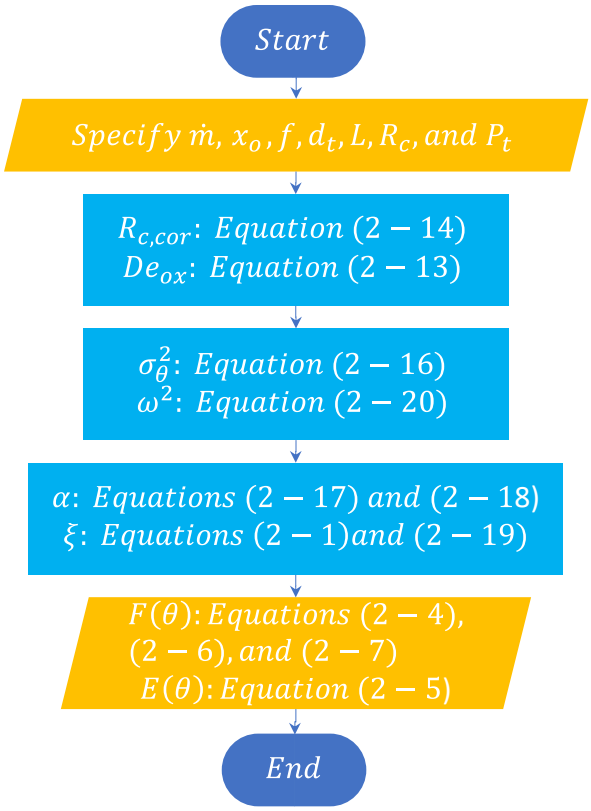

Figure A2. Steps to build an RTD for oscillatory flow coiled reactors using the operating conditions and reactor dimensions.

Appendix Symbols and Abbreviations

Latin Letters

d_t	mm	inner tube diameter
De_{ox}	-	oscillatory Dean number based on oscillation amplitude
E	-	exit time distribution function (RTD)
f	Hz	oscillation frequency
F	-	cumulative residence time distribution
K	$s^{-1}\cdot(mol\cdot L)^{(1-m)}$	reaction rate constant
K_{min}	$S\cdot cm^{-1}$	minimum conductivity
K_{max}	$S\cdot cm^{-1}$	maximum conductivity
L	m	tube length
$\dot{m}$	$g\cdot min^{-1}$	net mass flow rate
P_t	mm	coil tube pitch
R_c	mm	coil radius of curvature
t	s	Time
$\bar{t}$	s	mean residence time
t_{min}	s	start time of conductivity change
t_{max}	s	end time of conductivity change
x_o	mm	oscillation amplitude

Greek Letters

α	-	shape factor in skewed normal distribution model
θ	-	dimensionless time
ξ	-	location parameter in skewed normal distribution model
ω	-	kurtosis in skewed normal distribution model

Abbreviations

RTD	residence time distribution

References

[1] A. Pashkova, L. Greiner, Towards Small-Scale Continuous Chemical Production: Technology Gaps and Challenges, Chemie Ingenieur Technik 83 (2011) 1337–1342.

[2] J.A. Moulijn, M. Makkee, A.E. Van Diepen, Chemical Process Technology, 2013.

[3] D.M. Roberge, L. Ducry, N. Bieler, P. Cretton, B. Zimmermann, Microreactor Technology: A Revolution for the Fine Chemical and Pharmaceutical Industries?, Chem. Eng. Technol. 28 (2005) 318–323.

[4] T. Illg, P. Löb, V. Hessel, Flow chemistry using milli-and microstructured reactors - From conventional to novel process windows, Bioorg. Med. Chem. 18 (2010) 3707–3719.

[5] S.A. May, Flow chemistry, continuous processing, and continuous manufacturing: A pharmaceutical perspective, Journal of Flow Chemistry 7 (2017) 137–145.

[6] N. Kockmann, M. Gottsponer, B. Zimmermann, D.M. Roberge, Enabling continuous-flow chemistry in microstructured devices for pharmaceutical and fine-chemical production, Chemistry - A European Journal 14 (2008) 7470–7477.

[7] P. Plouffe, A. Macchi, D.M. Roberge, From batch to continuous chemical synthesis-a toolbox approach, Org. Process Res. Dev. 18 (2014) 1286–1294.

[8] D. Reay, C. Ramshaw, A. Harvey, Process Intensification: Engineering for Efficiency, Sustainability and Flexibility, 2nd Ed., Elsevier, Kidlington, 2013.

[9] C. Ramshaw, The Incentive for Process Intensification, in: BHR Group Conf. Ser., 1995: pp. 1–4.

[10] A.I. Stankiewicz, J.A. Moulijn, Process intensification: Transforming Chemical Engineering, Chem. Eng. Prog. (2000) 22–34.

[11] M. Baldea, T.F. Edgar, B.L. Stanley, A.A. Kiss, Modular manufacturing processes: Status, challenges, and opportunities, AIChE Journal 63 (2017) 4262–4272.

[12] S. Roy, Consider Modular Plant Design, Chem. Eng. Prog. (2017) 28–31.

[13] H. Lasi, P. Fettke, H.G. Kemper, T. Feld, M. Hoffmann, Industry 4.0, Business & Information Systems Engineering 6 (2014) 239–242.

[14] J. Britton, T.F. Jamison, The assembly and use of continuous flow systems for chemical synthesis, Nat. Protoc. 12 (2017) 2423–2446.

[15] M. Baumann, T.S. Moody, M. Smyth, S. Wharry, A Perspective on Continuous Flow Chemistry in the Pharmaceutical Industry, Org. Process Res. Dev. 24 (2020) 1802–1813.

[16] A.R. Bogdan, A.W. Dombrowski, Emerging Trends in Flow Chemistry and Applications to the Pharmaceutical Industry, J. Med. Chem. 62 (2019) 6422–6468.

[17] V.R.L.J. Bloemendal, M.A.C.H. Janssen, J.C.M. Van Hest, F.P.J.T. Rutjes, Continuous one-flow multi-step synthesis of active pharmaceutical ingredients, React. Chem. Eng. 5 (2020) 1186–1197.

[18] B. Doyle, Development of Micro to Milli-Scale Multiphase Reactors with and Without Solids for Integration Into Mini-Monoplants, University of Ottawa, 2020.

[19] B.J. Doyle, P. Elsner, B. Gutmann, O. Hannaerts, C. Aellig, A. Macchi, D.M. Roberge, Mini-Monoplant Technology for Pharmaceutical Manufacturing, Org. Process Res. Dev. 24 (2020) 2169–2182.

[20] B.J. Doyle, B. Gutmann, M. Bittel, T. Hubler, A. Macchi, D.M. Roberge, Handling of Solids and Flow Characterization in a Baffleless Oscillatory Flow Coil Reactor, Ind. Eng. Chem. Res. 59 (2020) 4007–4019.

[21] V. Hessel, H. Löwe, F. Schönfeld, Micromixers - A review on passive and active mixing principles, Chem. Eng. Sci. 60 (2005) 2479–2501.

[22] E. Mielke, P. Plouffe, S.S. Mongeon, C. Aellig, S. Filliger, A. Macchi, D.M. Roberge, Micro-reactor mixing unit interspacing for fast liquid-liquid reactions leading to a generalized scale-up methodology, Chemical Engineering Journal 352 (2018) 682–694.

[23] P. Stonestreet, P.M.J. Van Der Veeken, The Effects of Oscillatory Flow and Bulk Flow Components on Residence Time Distribution in Baffled Tube Reactors, Chemical Engineering Research and Design 77 (1999) 671–684.

[24] M.J. Hounslow, X. Ni, Population balance modelling of droplet coalescence and break-up in an oscillatory baffled reactor, Chem. Eng. Sci. 59 (2004) 819–828.

[25] J.R. McDonough, M.F. Oates, R. Law, A.P. Harvey, Micromixing in oscillatory baffled flows, Chemical Engineering Journal 361 (2019) 508–518.

[26] Y.A. Çengel, J.M. Cimbala, Fluid Mechanics Fundamentals and Applications, 4th ed., McGraw-Hill Education, New York, 2018.

[27] A. Kalpakli, Experimental study of turbulent flows through pipe bends, Royal Institute of Technology KTH Mechanics, 2012.

[28] P.M. Ligrani, A study of Dean vortex development and structure in a curved rectangular channel with aspect ratio of 40 at dean numbers up to 430, 1994.

[29] A.A. Aider, S. Skali, J.P. Brancher, Laminar-turbulent transition in Taylor-Dean flow, J. Phys. Conf. Ser. 14 (2005) 118–127.

[30] P.L. Spedding, E. Benard, G.M. McNally, Fluid flow through 90 degree bends, Developments in Chemical Engineering and Mineral Processing 12 (2004) 107–128.

[31] M. Rowe, Measurements and computations of flow in pipe bends, J. Fluid Mech. 43 (1970) 771–783.

[32] L.S. Yao, S.A. Berger, Entry flow in a curved pipe, J. Fluid Mech. 67 (1975) 177–196.

[33] S.Z. Ali, S. Dey, Entry flow in curved pipes: Turbulent boundary layer approach, Journal of Hydraulic Research 54 (2016) 90–101.

[34] R.M.C. So, M. Anwer, Swirling turbulent flow through a curved pipe: Part 2: Recovery from swirl and bend curvature, Experiments in Fluids: Experimental Methods and Their Applications to Fluid Flow 14 (1993) 169–177.

[35] M.J. Tunstall, J.K. Harvey, On the effect of a sharp bend in a fully developed turbulent pipe-flow, J. Fluid Mech. 34 (1968) 595–608.

[36] C. Brücker, A time-recording DPIV-study of the swirl-switching effect in a 90° bend flow, in: Proc. 8th International Symposium on Flow Visualization, Sorrento, 1998: pp. 171.1-171.6.

[37] F. Rütten, W. Schröder, M. Meinke, Large-eddy simulation of low frequency oscillations of the Dean vortices in turbulent pipe bend flows, Physics of Fluids 17 (2005) 035107.

[38] J. Pruvost, J. Legrand, P. Legentilhomme, Numerical investigation of bend and torus flows, part I : Effect of swirl motion on flow structure in U-bend, Chem. Eng. Sci. 59 (2004) 3345–3357.

[39] A. Hopley, Liquid Residence Time Distribution in Micro-reactors with Complex Geometries, University of Ottawa, 2018.

[40] L. Sharma, K.D.P. Nigam, S. Roy, Single phase mixing in coiled tubes and coiled flow inverters in different flow regimes, Chem. Eng. Sci. 160 (2017) 227–235.

[41] M. Mridha, K.D.P. Nigam, Coiled flow inverter as an inline mixer, Chem. Eng. Sci. 63 (2008) 1724–1732.

[42] S. Soni, L. Sharma, P. Meena, S. Roy, K.D.P. Nigam, Compact coiled flow inverter for process intensification, Chem. Eng. Sci. 193 (2019) 312–324.

[43] A.K. Saxena, K.D.P. Nigam, Coiled configuration for flow inversion and its effect on residence time distribution, AIChE Journal 30 (1984) 363–368.

[44] J.R. McDonough, S. Murta, R. Law, A.P. Harvey, Oscillatory fluid motion unlocks plug flow operation in helical tube reactors at lower Reynolds numbers (Re ≤ 10), Chemical Engineering Journal 358 (2019) 643–657.

[45] S.S. Mongeon, D.M. Roberge, M. Bittel, P. Elsner, A. Macchi, Liquid-Liquid Mass Transfer in an Oscillatory-Flow Mesoscale Coil Reactor without Baffles, Org. Process Res. Dev. 20 (2016) 733–741.

[46] T. McGlone, N.E.B. Briggs, C.A. Clark, C.J. Brown, J. Sefcik, A.J. Florence, Oscillatory Flow Reactors (OFRs) for Continuous Manufacturing and Crystallization, Org. Process Res. Dev. 19 (2015) 1186–1202.

[47] O. Levenspiel, Chemical Reaction Engineering, 3rd Ed., Wiley, New York, 1999.

[48] K. Sudo, M. Sumida, Y. Yamane, Secondary motion of fully developed oscillatory flow in a curved pipe, J. Fluid Mech. 237 (1992) 189–208.

[49] P. Trambouze, J.P. Euzen, Chemical Reactors: From Design to Operation, Editions Technip, Paris, 2004.

[50] S. Li, J. Xu, Y. Wang, G. Luo, Mesomixing scale controlling and its effect on micromixing performance, Chem. Eng. Sci. 62 (2007) 3620–3626.

[51] K.R. Westertrep, W.P.M. Van Swaaij, A.A.C.M. Beenackers, Chemical Reactor Design and Operation, 2nd Ed., Wiley, Chichester, 1984.

[52] J. Baldyga, J.R. Bourne, Turbulent mixing and chemical reactions, Wiley, 1999.

[53] B.K. Johnson, R.K. Prud'homme, Chemical processing and micromixing in confined impinging jets, AIChE Journal 49 (2003) 2264–2282.

[54] A. Ghanem, T. Lemenand, D. Della Valle, H. Peerhossaini, Static mixers: Mechanisms, applications, and characterization methods – A review, Chemical Engineering Research and Design 92 (2014) 205–228.

[55] Z. Mao, C. Yang, Micro-mixing in chemical reactors: A perspective, Chin. J. Chem. Eng. 25 (2017) 381–390.

[56] J.M. Commenge, L. Falk, Villermaux–Dushman protocol for experimental characterization of micromixers, Chemical Engineering and Processing: Process Intensification 50 (2011) 979–990.

[57] M.I. da Silva Nunes, Micromixing in Chemical Reactors: Test Reactions, Universidade do Porto, 2007.

[58] H.S. Fogler, Elements of Chemical Reaction Engineering, 5th Ed., Prentice Hall, Boston, 2016.

[59] P.M. Ligrani, S. Choi, A.R. Schallert, P. Skogerboe, Effects of Dean vortex pairs on surface heat transfer in curved channel flow, Int. J. Heat Mass Transf. 39 (1996) 27–37.

[60] M. Ghobadi, Y.S. Muzychka, A Review of Heat Transfer and Pressure Drop Correlations for Laminar Flow in Curved Circular Ducts, Heat Transfer Engineering 37 (2016) 815–839.

[61] R. Law, S.M.R. Ahmed, N. Tang, A.N. Phan, A.P. Harvey, Development of a more robust correlation for predicting heat transfer performance in oscillatory baffled reactors, Chemical Engineering and Processing: Process Intensification 125 (2018) 133–138.

[62] N.S. Tavare, Mixing in continuous crystallizers, AIChE Journal 32 (1986) 705–732.

[63] H. Nagasawa, K. Mae, Development of a new microreactor based on annular microsegments for fine particle production, Ind. Eng. Chem. Res. 45 (2006) 2179–2186.

[64] F. Castro, S. Kuhn, K. Jensen, A. Ferreira, F. Rocha, A. Vicente, J.A. Teixeira, Continuous-flow precipitation of hydroxyapatite in ultrasonic microsystems, Chemical Engineering Journal 215–216 (2013) 979–987.

[65] S.L. Poe, M.A. Cummings, M.P. Haaf, D.T. McQuade, Solving the Clogging Problem: Precipitate-Forming Reactions in Flow, Angewandte Chemie-International Edition 45 (2006) 1544–1548.

[66] A.I. Stankiewicz, T. Van Gerven, G. Stefanidis, The fundamentals of process intensification, Wiley-VCH, Weinheim, 2019.

[67] A. Macchi, P. Plouffe, G.S. Patience, D.M. Roberge, Experimental methods in chemical engineering: Micro-reactors, Can. J. Chem. Eng. 97 (2019) 2578–2587.

[68] B.J. Doyle, G. Vrbanec, C. Aellig, E. Marcelić, S. Filliger, A. Macchi, D.M. Roberge, Continuous Production of an API Suspension (ZS-9) under Oscillatory Flow at Intensified Temperature and Pressure, Org. Process Res. Dev. 28 (2024) 1929–1937.

[69] M. Avila, D.F. Fletcher, M. Poux, C. Xuereb, J. Aubin, Mixing performance in continuous oscillatory baffled reactors, Chem. Eng. Sci. 219 (2020) 115600.

[70] G. Jimeno, Y.C. Lee, X.W. Ni, The effect of particle size on flow in a continuous oscillatory baffled reactor using CFD, Canadian Journal of Chemical Engineering 100 (2022) S258–S271.

[71] I.I. Onyemelukwe, Z.K. Nagy, C.D. Rielly, Solid-liquid axial dispersion performance of a mesoscale continuous oscillatory flow crystalliser with smooth periodic constrictions using a non-invasive dual backlit imaging technique, Chemical Engineering Journal 382 (2020) 122862.

[72] I.I. Onyemelukwe, B. Benyahia, N.M. Reis, Z.K. Nagy, C.D. Rielly, The heat transfer characteristics of a mesoscale continuous oscillatory flow crystalliser with smooth periodic constrictions, Int. J. Heat Mass Transf. 123 (2018) 1109–1119.

[73] A. Ferreira, P.O. Adesite, J.A. Teixeira, F. Rocha, Effect of solids on O2 mass transfer in an oscillatory flow reactor provided with smooth periodic constrictions, Chem. Eng. Sci. 170 (2017) 400–409.

[74] N. Reis, A.P. Harvey, M.R. Mackley, A.A. Vicente, J.A. Teixeira, Fluid Mechanics and Design Aspects of a Novel Oscillatory Flow Screening Mesoreactor, Chemical Engineering Research and Design 83 (2005) 357–371.

[75] M. Avila, B. Kawas, D.F. Fletcher, M. Poux, C. Xuereb, J. Aubin, Design, performance characterization and applications of continuous oscillatory baffled reactors, Chemical Engineering and Processing - Process Intensification 180 (2022) 108718.

[76] P. Bianchi, J.D. Williams, C.O. Kappe, Oscillatory flow reactors for synthetic chemistry applications, J. Flow Chem. 10 (2020) 475–490.

[77] X. Ni, H. Jian, A.W. Fitch, Computational fluid dynamic modelling of flow patterns in an oscillatory baffled column, Chem. Eng. Sci. 57 (2002) 2849–2862.

[78] C.G. Niño, N. Kapur, M.F. King, G. de Boer, A.J. Blacker, R. Bourne, H. Thompson, Computational fluid dynamic enabled design optimisation of miniaturised continuous oscillatory baffled reactors in chemical processing, Int. J. Comut. Fluid Dyn. 33 (2019) 317–331.

[79] N. Kljajić, B. Todić, D. Slavnić, N. Nikačević, Turbulent flow modeling in continuous oscillatory flow baffled reactor using STAR CCM+, Computer Aided Chemical Engineering 46 (2019) 841–846.

[80] G. Valitov, D. Rossi, C. Price, A. Gavriilidis, L. Mazzei, Axial dispersion in curved channels in the presence of pulsating flow, Chemical Engineering and Processing - Process Intensification 180 (2022) 108629.

[81] J. Claes, B. Metten, B. Brabants, M.E. Leblebici, S. Kuhn, L.C.J. Thomassen, Oscillatory Flow for Slurry Transport in Baffleless Milliflow Reactors, Ind. Eng. Chem. Res. 62 (2023) 12647–12655.

[82] A. Bérard, B. Blais, G.S. Patience, Experimental methods in chemical engineering: Residence time distribution—RTD, Canadian Journal of Chemical Engineering 98 (2020) 848–867.

[83] J.H. Ham, B. Platzer, Semi-empirical equations for residence time distributions in disperse systems - Part 1: Continuous phase, Chem. Eng. Technol. 27 (2004) 1172–1178.

[84] A. Azzalini, A. Capitanio, The Skew-Normal and Related Families, Cambridge University Press, New York, 2014.

[85] D.B. Owen, Tables for computing bivariate normal probabilities, Annals of Mathematical Statistics 27 (1956) 1075–1090.

[86] OpenFOAM CFD Software, (n.d.). https://openfoam.org/ (accessed December 9, 2023).

[87] H. Itō, Friction Factors for Turbulent Flow in Curved Pipes, J. Fluids Eng. 81 (1959) 123–132.

[88] G. Jimeno, Y.C. Lee, X.W. Ni, On the evaluation of power density models for oscillatory baffled reactors using CFD, Chem. Eng. Process. 134 (2018) 153–162.

[89] J.L. Plawsky, Transport Phenomena Fundamentals, 4th Edition, CRC Press, Boca Raton, 2019.

[90] M. Avila, D.F. Fletcher, M. Poux, C. Xuereb, J. Aubin, Predicting power consumption in continuous oscillatory baffled reactors, Chem. Eng. Sci. 212 (2020) 115310.

[91] L.C. Truesdell, R.J. Adler, Numerical treatment of fully developed laminar flow in helically coiled tubes, AIChE Journal 16 (1970) 1010–1015.

[92] K. Sutherland, L. Pakzad, P. Fatehi, CFD population balance modeling and dimensionless group analysis of a multiphase oscillatory baffled column (OBC) using moving overset meshes, Chem. Eng. Sci. 199 (2019) 552–570.

[93] J. Muñoz-Cámara, J.P. Solano, J. Pérez-García, Experimental correlations for oscillatory-flow friction and heat transfer in circular tubes with tri-orifice baffles, International Journal of Thermal Sciences 156 (2020) 106480.

[94] J. Muñoz-Cámara, D. Crespí-Llorens, J.P. Solano, P.G. Vicente, Experimental analysis of flow pattern and heat transfer in circular-orifice baffled tubes, Int. J. Heat Mass Transf. 147 (2020) 118914.

[95] D. González-Juárez, R. Herrero-Martín, J.P. Solano, Enhanced heat transfer and power dissipation in oscillatory-flow tubes with circular-orifice baffles: a numerical study, Appl. Therm. Eng. 141 (2018) 494–502.

[96] M.H.I. Baird, N.V.R. Rao, Power dissipation and flow patterns in reciprocating baffle-plate columns, Canadian Journal of Chemical Engineering 73 (1995) 417–425.

[97] J. Muñoz-Cámara, J.P. Solano, J. Pérez-García, Non-dimensional analysis of experimental pressure drop and energy dissipation measurements in Oscillatory Baffled Reactors, Chem. Eng. Sci. 262 (2022) 118030.

[98] H. Khosravi-Bizhaem, A. Abbassi, A. Zivari Ravan, Heat transfer enhancement and pressure drop by pulsating flow through helically coiled tube: An experimental study, Appl. Therm. Eng. 160 (2019) 114012.

[99] M.T. Abdelghany, S.M. Elshamy, M.A. Sharafeldin, O.E. Abdellatif, Experimental investigation on the effect of pulsating flow on heat transfer and pressure drop in conical tubes, J. Therm. Anal. Calorim. 148 (2023) 6169–6182.

[100] A.A. Abbasian Arani, A. Jahani, Turbulent Pulsating Nanofluids Flow and Heat Transfer inside Constant Heat Flux Boundary Condition Helical-Coil Tube, AUT Journal of Mechanical Engineering 4 (2020) 289–300.

[101] M.M. Fadaee, B.J. Doyle, D.M. Roberge, A. Macchi, J.B. Haelssig, Liquid flow field and residence time distribution in a baffleless oscillatory flow coil reactor, Chemical Engineering Journal 492 (2024) 151758.

[102] I. Di Piazza, M. Ciofalo, Numerical prediction of turbulent flow and heat transfer in helically coiled pipes, International Journal of Thermal Sciences 49 (2010) 653–663.

[103] M. Van Dyke, Extended Stokes series: laminar flow through a loosely coiled pipe, J. Fluid Mech. 86 (1978) 129–145.

[104] F. Florit, R. Rota, K.F. Jensen, Dispersion in coiled tubular reactors: A CFD and experimental analysis on the effect of pitch, Chem. Eng. Sci. 233 (2021) 116393.

[105] B.J. Doyle, F. Morin, J.B. Haelssig, D.M. Roberge, A. Macchi, Gas-Liquid Flow and Interphase Mass Transfer in LL Microreactors, Fluids 5 (2020) 223.

[106] L.D.G. Sigalotti, C.E. Alvarado-Rodríguez, O. Rendón, Fluid Flow in Helically Coiled Pipes, Fluids 8 (2023) 308.

[107] B.K. Hardik, P.K. Baburajan, S. V. Prabhu, Local heat transfer coefficient in helical coils with single phase flow, Int. J. Heat Mass Transf. 89 (2015) 522–538.

[108] W.I.A. Aly, H. Inaba, N. Haruki, A. Horibe, Drag and Heat Transfer Reduction Phenomena of Drag-Reducing Surfactant Solutions in Straight and Helical Pipes, J. Heat Transfer 128 (2006) 800–810.

[109] T.L. Bergman, A.S. Lavine, F.P. Incropera, D.P. DeWitt, Introduction to Heat Transfer, John Wiley & Sons, 2011.

[110] E. Mielke, P. Plouffe, N. Koushik, M. Eyholzer, M. Gottsponer, N. Kockmann, A. Macchi, D.M. Roberge, Local and overall heat transfer of exothermic reactions in microreactor systems, React. Chem. Eng. 2 (2017) 763–775.

[111] G.H. Cummings, A.S. West, Heat Transfer Data for Kettles with Jackets and Coils, Ind. Eng. Chem. 42 (1950) 2303–2313.

[112] P. Kováts, C. Velten, M. Mansour, D. Thévenin, K. Zähringer, Mixing characterization in different helically coiled configurations by laser-induced fluorescence, Exp. Fluids 61 (2020) 1–17.

[113] R.A. Seban, E.F. McLaughlin, Heat transfer in tube coils with laminar and turbulent flow, Int. J. Heat Mass Transf. 6 (1963) 387–395.

[114] N. Acharya, M. Sen, C. Hsueh-Chia, Heat transfer enhancement in coiled tubes by chaotic mixing, Int. J. Heat Mass Transf. 35 (1992) 2475–2489.

[115] M.R. Salimpour, Heat transfer characteristics of a temperature-dependent-property fluid in shell and coiled tube heat exchangers, International Communications in Heat and Mass Transfer 35 (2008) 1190–1195.

[116] M. Moawed, Experimental study of forced convection from helical coiled tubes with different parameters, Energy Convers. Manag. 52 (2011) 1150–1156.

[117] M. Kahani, S. Zeinali Heris, S.M. Mousavi, Comparative study between metal oxide nanopowders on thermal characteristics of nanofluid flow through helical coils, Powder Technol. 246 (2013) 82–92.

[118] S.S. Pawar, V.K. Sunnapwar, Experimental studies on heat transfer to Newtonian and non-Newtonian fluids in helical coils with laminar and turbulent flow, Exp. Therm. Fluid Sci. 44 (2013) 792–804.

[119] F.P. Incropera, Dewitt David P., T.L. Bergman, A.S. Lavine, Fundamentals of Heat and Mass Transfer, 6th ed., John Wiley & Sons, Hoboken, 2007.

[120] X. Niu, Y.K. Lee, Efficient spatial-temporal chaotic mixing in microchannels, Journal of Micromechanics and Microengineering 13 (2003) 454–462.

[121] S. Qian, H.H. Bau, A chaotic electroosmotic stirrer, Anal. Chem. 74 (2002) 3616–3625.

[122] P. Woias, K. Hauser, E. Yacoub-George, An Active Silicon Micromixer for μTAS Applications, Micro Total Analysis Systems (2000) 277–282.

[123] I. Glasgow, N. Aubry, Enhancement of microfluidic mixing using time pulsing, Lab Chip 3 (2003) 114–120.

[124] Green. Don W., M.Z. Southard, eds., Perry's Chemical Engineers' Handbook, 9th ed., McGraw-Hill Education, New York, 2018.

[125] What is Z-average Size Determined by DLS?, (n.d.). https://www.horiba.com/int/scientific/technologies/dynamic-light-scattering-dls-particle-size-distribution-analysis/z-average/ (accessed January 25, 2026).

[126] M.J.J. Mayer, J. Meuldijk, D. Thoenes, Dynamic Modeling of limited Particle Coagulation in Emulsion Polymerization, J. Appl. Polym. Sci. 59 (1996) 83–90.